Theses and Dissertations

2019-07-01

3D Printed Microfluidic Devices for Bioanalysis

Michael J. Beauchamp
Brigham Young University

Follow this and additional works at: https://scholarsarchive.byu.edu/etd

3D Printed Microfluidic Devices for Bioanalysis

Michael J. Beauchamp

A dissertation/thesis submitted to the faculty of
Brigham Young University
in partial fulfillment of the requirements for the degree of

Doctor of Philosophy

Adam T. Woolley, Chair
Jaron C. Hansen
Gregory P. Nordin
Daniel E. Austin

Department of Chemistry and Biochemistry

Brigham Young University

ABSTRACT

3D Printed Microfluidic Devices for Bioanalysis

Michael J. Beauchamp
Department of Chemistry and Biochemistry, BYU
Doctor of Philosophy

This work presents the development of 3D printed microfluidic devices and their application to microchip analysis. Initial work was focused on the development of the printer resin as well as the development of the general rules for resolution that can be achieved with stereolithographic 3D printing. The next stage of this work involved the characterization of the printer with a variety of interior and exterior resolution features. I found that the minimum positive and negative feature sizes were about 20 μm in either case. Additionally, micropillar arrays were printed with pillar diameters as small as 16 μm. To demonstrate one possible application of these small resolution features I created microfluidic bead traps capable of capturing 25 μm polystyrene particles as a step toward capturing cells. A second application which I pioneered was the creation of devices for microchip electrophoresis. I separated 3 preterm birth biomarkers with good resolution (2.1) and efficiency (3600 plates), comparable to what has been achieved in conventionally fabricated devices. Lastly, I have applied some of the unique capabilities of our 3D printer to a variety of other device applications through collaborative projects. I have created microchips with a natural masking monolith polymerization window, spiral electrodes for capacitively coupled contactless conductivity detection, and a removable electrode insert chip. This work demonstrates the ability to 3D print microfluidic structures and their application to a variety of analyses.

ACKNOWLEDGEMENTS

TABLE OF CONTENTS

LIST OF TABLES

LIST OF FIGURES

1. INTRODUCTION[*]

1.1   Microfluidics

Chemical analyses are valuable tools used to help understand the natural world by measuring interactions between molecules. The creation and optimization of these instruments allows new discoveries further expanding what can be learned through chemical experiments. One growing and useful field of study for a wide variety of applications is microfluidics. The field of microfluidics studies the use and manipulation of liquids in devices with features smaller than about 100 micrometers.[1] Though originally demonstrated in the late 1970's,[2] this area has seen rapid growth as researchers have recently found many applications and opportunities for these types of devices. This field featured 1820 papers published in 2016, 2028 in 2017, 2272 in 2018, and already 1092 this year (as of the date of this publication).

Several of the important early applications helped drive the development of the field of microfluidics. One of the first microfluidic devices was demonstrated in 1992 using a glass device to perform electroosmotic pumping and microchip electrophoresis (μCE) of a mixture of calcein and fluorescein.[3] Later, microchip electrophoresis was extended to more complex biomolecules, such as DNA, and new materials, such as elasotmers[4] and thermoplastics.[5] To help the worlds of drug discovery and medicine, microfluidic devices have been valuable in their ability to conserve reagents, perform synthesis, and control flow and temperature.[6,7] The small size of the channels in microfluidics also made this field an attractive method for studying single

---

[*] Sections 1.2.1 and 1.2.2 of this chapter are adapted with permission from Beauchamp, M.J., Nordin, G.P., Woolley A. T. Moving from millifluidic to truly microfluidic sub-100-μm cross-section 3D printed devices. Anal. Bioanal. Chem. 2017. 409: 4311-9.

cells in non-destructive manners.[8] As the field of microfluidic analysis continue to advance, additional technologies and applications become more widespread. For example, the variety of materials continues to grow with additions such as surface modifications,[9] the use of devices for diagnostics in resource limited settings,[10] more rapid biological analyses,[11] and organs-on-chip models.[12]

While too numerous to mention all the various components that can be combined in microfluidic devices, several key processes are incorporated into most, namely, reservoirs to hold reagents, channels to transport fluid, and functional features such as monoliths,[13] reaction chambers,[14] valves, pumps,[15] and interconnects. By connecting several of these microfluidic components together in series, parallel or both, complex microfluidic systems can be created for analyses.[16]

1.1.1   Advantages of Microfluidics

Microfluidics offer several advantages over traditional laboratory techniques such as requiring lower sample volumes, generating less waste, combining multiple processes on one chip, costing relatively little to manufacture, and being portable if ancillary equipment is similarly portable. Low sample consumption is ideal for expensive or rare materials, especially biological samples, which in turn leads to lower waste generation and cleanup costs.[17,18] By combining several processes in the microfluidic device, the user is able to streamline sample handling and potentially automate fluidic manipulation, saving time and effort.[7,19] The cost of materials for fabricating microfluidic devices is generally low because several devices can be made from a single set of master molds from thermoplastic materials such as poly(methyl methacrylate) (PMMA) or cyclic olefin copolymer (COC) or alternatively, PDMS devices can be

cast.[20,21] This also makes microfluidic devices an attractive option in resource limited settings. Lastly, because of their compact size, microfluidic devices are readily portable making them ideal for field or point of care testing.[22]

1.1.2 Microchip Electrophoresis

The first type of microfluidic analysis was µCE, and it has been used steadily since with about a hundred papers published per year over the last 5 years.[3] µCE is based on well characterized instrumental capillary electrophoresis (CE). CE is a separation technique in which analytes are separated based on their size, shape, and charge in an applied electric field while in a buffered solution.[23] CE, and by extension µCE, has advantages as a separation technique in that it is a non-destructive technique, it has typically excellent resolution, and it works well with biological molecules. The electrophoretic mobility of a given analyte is based on the size of the molecule and on the magnitude of its charge where larger analytes move more slowly than smaller ones, and more highly charged analytes move more quickly than lower charged ones. The formula for electrophoretic mobility is given in equation 1.1 where μ_e is the electrophoretic mobility, q is the charge of the analyte, η is the viscosity of the buffer, and r is the hydrodynamic radius of the molecule.[24] The electrophoretic mobility, then is largely dependent on intrinsic properties of the analyte, namely charge and radius. The viscosity of the buffer will be the same for all the analyses in this dissertation.

$$\mu_e = q/6\pi\eta r \tag{1.1}$$

The second force which acts on the analyte under CE or µCE conditions is electroosmotic

flow (EOF). The formula for electroosmotic mobility (μ_o) is given in equation 1.2 below,[24] where

ε is the dielectric constant and ζ is the zeta potential of the capillary or channel surface.

$$\mu_o = \frac{\varepsilon\zeta}{4\pi\eta} \tag{1.2}$$

To find the net speed or velocity, v, at which the analyte then moves through the capillary

we combine equations 1.1 and 1.2 into equation 1.3. The velocity also depends on the applied

electric field, E.

$$v = E(\mu_e + \mu_o) \tag{1.3}$$

The surface of a capillary or channel is typically negatively charged which causes some

of the positive ions of the filling buffer solution to accumulate near the surface. Then, when a

voltage is applied, these positive ions migrate toward the cathode carrying the bulk solution with

them. This EOF affects the flow of analytes in the capillary, and thus the total velocity of an

analyte is a combination of both its electrophoretic mobility and the solution electroosmotic

mobility, as well as the electric field.

1.2   3D Printing

Three-dimensional (3D) printing has quickly gained acclaim as a technology with the

potential to revolutionize manufacturing and scientific research.[25,26] It is a technique whereby a

physical object is created from a digital design file.[27] The object is generally made by a printer one layer at a time on the basis of the printing method and algorithms in the printer software that determine where to form solid material according to the design and certain user specifications.

1.2.1 Types of 3D Printers

3D printing of fluidic features typically uses one of three approaches: polyjet (PJ), stereolithography (SLA), or fused deposition modeling (FDM). PJ printers use a sprayer to deposit droplets of resin, which are cured by UV light; successive layers are then formed and cured on top of each previous layer. To make fluidic structures PJ printing requires the use of a sacrificial support material for imbedded channels or voids, so the next layer can be deposited on top. PJ printing has approximately 25-μm resolution for positioning of the print head and can form devices from two or more component inks; however, a key challenge for PJ printed fluidics is the difficulty in effectively removing the sacrificial support materials from fluidic channels. Examples of PJ printers include the Projet 3000HD and Objet 30.

FDM is a method that uses a thermoplastic that is extruded though a heated nozzle in patterned layers, which after cooling and hardening give a device. FDM generally prints quickly but suffers from lower resolution (approximately 50 μm for print head placement, but typical nozzle extrusion diameters and layer heights are hundreds of micrometers) than either PJ printing or SLA. FDM has the benefit of being able to print different materials because multiple print heads can be incorporated at the same time. Additionally, if stopping and restarting printing at specified times is feasible, multiple materials such as glass coverslips or semipermeable membranes can be introduced during the process. Examples of FDM printers include the Stratasys Dimension Elite and Makerbot Replicator.

SLA uses a vat of liquid resin that is photopolymerized typically with LED light patterned by a projector or a scanned laser that determines the spatial resolution. In SLA, patterned interior voids for fluids contain unpolymerized liquid resin that must be flushed after fabrication. This process is much easier than for either PJ printing or FDM since the unpolymerized resin is a liquid (and low-viscosity resins can be made). In theory, SLA resolution for fluidic structures is limited in current commercial 3D printers by the projector pixel size to approximately 30 μm, but in practice polymerization in subsequent layers typically limits channel cross sections to approximately 500 μm. Examples of SLA printers include the Miicraft and Asiga Pico Plus. A subcategory of SLA is two-photon polymerization (TPP). TPP 3D printing uses a scanned laser instead of an LED and projector as the light source and has very high resolution (approximately 1 μm).[28-30] Unfortunately, multiple fundamental limitations of TPP hinder its application in the making of microfluidic devices. For example, because each voxel must be individually addressed, print times can be as long as 10 h per cubic millimeter. Moreover, TPP 3D printers typically cost hundreds of thousands of dollars, making them cost prohibitive for many research applications. These price/size/time constraints severely limit TPP 3D printing to niche, very high resolution applications, rather than construction of microfluidic analysis devices.

1.2.2   Advantages of 3D Printing

3D printing as a method of creating structures allows rapid iterative changes in design to be made and then fabricated, which is one reason why 3D printing is sometimes referred to as rapid prototyping. This ability to quickly change or edit designs also allows varied structures to be made without the expensive and time-consuming processes involved in forming new masters,

6

templates, or molds in conventional micromachining. Indeed, 3D printed fluidic devices can be made in a modular manner with individual components linked together in various configurations to create working devices from multiple pieces.[31-34] In addition to facilitating rapid prototyping, 3D printing can provide an automated process wherein a complete device is made with essentially no operator input in the manufacturing process, reducing time and training requirements. Following fabrication, potentially simple post-processing steps such as resin clearing or support removal are all that need to be done to make a device ready for use. 3D printing holds considerable potential value for analytical chemists, as varied, custom-designed miniaturized parts can be made rapidly and with low costs. A key advantage of 3D printing is that it has a much lower cost barrier to entry than conventional cleanroom-based techniques for microfabrication that require expensive equipment and extensive training. These features motivated researchers to use 3D printing to create fluidic structures for analytical applications and to desire to make 3D printed microfluidic devices.

Perhaps one of the greatest potential advantages 3D printing could offer microfluidics is the possibility of making complex 3D fluidic networks much more easily than with use of stacked, two-dimensional surface micromachined layers. 3D printing can also allow simplified interfacing of devices with external fluid sources, as threaded ports[35,36] and Luer-lock systems[32,37,38] have been printed as part of fluidic devices. Finally, 3D printing design files can be shared easily, which should facilitate collaboration and enable broad use.

1.3   Pre-Term Birth

Pre-term birth (PTB) is defined as birth of the baby before the 37th week of pregnancy. Affecting approximately 1 in 10 births worldwide, this potentially dangerous complication is the

most common of pregnancy, unfortunately resulting in 1 million infant deaths per year.[39,40] In addition, many of the survivors suffer from adverse conditions from incomplete development such as vision, hearing, neurological, respiratory, and cardiac challenges.[41,42] The estimated cost of PTB is ~$26 billion as of 2007 and continues to rise.[43]

Fortunately, when PTB is suspected therapeutic interventions exist such as progesterone injections to help delay birth,[44] increasing the chance of survival, but difficulties arise because there is no clinically available method to assess PTB risk. Thus a key unmet medical need exists to develop a platform to predict and diagnose PTB allowing for both the treatment of the patient as well as the ability to study the underlying causes to potentially prevent PTB from occurring in the future.

To help in these diagnostic efforts, researchers have identified six maternal serum biomarkers that are implicated in PTB risk.[45-48] Three recently identified peptides, fragments of a larger protein called inter-alpha-trypsin inhibitor heavy chain IV, have been added to this panel of biomarkers, and when taken together, have 87% sensitivity and 81% specificity in predicting PTB at 28 weeks of pregnancy.[49] A list of these biomarkers can be seen in Table 1.1, along with additional information about their molecular weight and PTB risk level.

Table 1.1 Pre-term birth biomarkers

PTB Biomarker	Abbreviation	Molecular Weight (kDa)	PTB Risk Level (nM)
Peptide 1-QLGLPGPPDVPDHAAYHPF	P1	2.0	Unknown
Peptide 2-NVHSAGAAGSRMNFRPGVLSSR QLGLPGPPDVPDHAAYHPF	P2	4.2	Unknown
Peptide 3-NVHSAGAAGSRM(O)NFRPGVLS SRQLGLPGPPDVPDHAAYHPF	P3	4.2	Unknown
Corticotropin releasing factor	CRF	2.7	0.075
Defensins	Def	3-6	178
Tumor necrosis factor-α receptor type 1	TNF	26	0.06
Lactoferrin	LF	80	3
Thrombin-antithrombin III	TAT	95-110	7900
Ferritin	Fer	470	0.040

Current methods used to analyze PTB biomarkers such as HPLC, ELISA, and mass spectrometry are time consuming, expensive and require large, complex instruments rendering them not suitable for point of care applications. For example, the sample preparation methods required to analyze the smaller peptides such as P1 or CRF are much different from the ones used for larger proteins like Fer or TAT. In addition, the HPLC-MS methods used to analyze compounds of such different m/z ratios may not be compatible requiring multiple analyses in multiple configurations.[50] Additionally, the instrumentation required for HPLC-MS is very expensive and not available in most doctors' offices. ELISA is an often used and robust technique however difficulties exist using this technique for multiplexing due to interference from other species.[51] Sandwich immunoassays also could be used, but the smaller peptides can be very difficult to detect due to their small size.[52] Both these techniques suffer from lower detection limits than other methods. This presents an opportunity for simple, affordable, portable microfluidic systems capable of analyzing PTB risk.

1.4   Dissertation Overview

3D printing offers a unique opportunity to develop and manufacture microfluidic devices. The ease of fabrication and rapid feedback provided by this technology are particularly attractive in a field where the optimal device design, layout and features are not known but rather determined experimentally. Then in turn, these devices can be brought to bear on tackling challenging biomedical applications. To this end, this dissertation focuses on 3D printing microfluidic devices and their application in analyses, including PTB biomarker detection.

In chapter 2, I briefly describe the high-resolution 3D printer developed in Dr. Nordin's lab, as well as my efforts to characterize commercial and custom resin formulations. Material absorption properties were determined for a number of different resins using the measured thickness of membranes printed at various exposure times. With this information and the developed 3D printer, a fellow graduate student was able to create microfluidic channels using this custom resin formulation.

In chapter 3, creation of several types of features using the 3D printer described in chapter 2 is evaluated fully. I designed and printed positive and negative features on the exterior and interior of devices. In addition, micropillar arrays and microparticle trapping devices are printed and characterized. The features are measured with scanning electron microscopy (SEM) as well as optical profilometry where appropriate and the produced size is compared to the designed size. In addition, the effect of individual layer exposure time is studied as it plays a major role in the overall feature shape. A novel exposure pattern using multiple images per layer is also demonstrated with its effect on print quality.

In chapter 4, a microfluidic device is created for microchip electrophoresis of PTB biomarkers. Parameters for the separation are optimized such as device layout, reservoir size,

buffer identity and applied voltages. The device is characterized for following Ohm's Law and confirming operation under stable conditions. Initial separations are demonstrated using fluorescently labeled amino acids to demonstrate the function of the first 3D printed microchip electrophoresis device. Then this system is utilized on a panel of three PTB biomarkers (Fer, P1 and CRF, see Table 1.1).

In chapter 5, I present several different unique 3D printed microfluidic structures. First, I created a monolith polymerization window (MPW) that allowed maskless, spatially controlled polymerization of the monoliths for use in immoaffinity extraction of a PTB biomarker, Fer, in concentrated serum. A second functionality enabled by 3D printing was the production of a spiral electrode wrapped around a μCE channel for label-free capacitatively coupled contactless conductivity (C4D) detection. These devices were confirmed to be operational under C4D-like settings by performing a separation of an amino acid test mixture with and without the voltage applied. Finally, a T-shaped μCE device like that in chapter 4 was created, with a removable insert for electrochemical detection near the end of the separation channel. These devices were tested using an amino acid mixture with the insert in place to confirm a liquid-tight seal. All of these devices demonstrate unique functionalities over conventional microfluidic fabrication techniques enabled by 3D printing.

Chapter 6 summarizes the results presented and gives conclusions for this work. Future directions for this work in printer and resin improvements, separations results, and device optimization are also described.

1.5 References

1. Whitesides, G. M. The origins and the future of microfluidics. *Nature.* **2006**, 442, 368-373.

2. Terry, S. C., Jerman, J. H., Angell, J. B. A gas chromatographic air analyzer fabricated on a silicon wafer. *IEEE Trans. Electron Devices.* **1979**, 26, 1880-1886.

3. Harrison, D. J., Manz, A., Fan, Z., Luedi, H., Widmer, H. M. Capillary electrophoresis and sample injection systems integrated on a planar glass chip. *Anal. Chem*. **1992**, 64, 1926-32.

4. Effenhauser, C. S., Bruin, G. J. M., Paulus, A., Ehrat, M. Integrated capillary electrophoresis on flexible silicone microdevices: Analysis of DNA restriction fragments and detection of single DNA molecules on microchips. *Anal. Chem.* **1997**, 69, 3451-3457.

5. McCormick, R. M., Nelson, R. J., Alonso-Amigo, M. G. Microchannel electrophoretic separations of DNA in injection-molded plastic substrates. *Anal. Chem*. **1997**, 69, 2626-2630.

6. Pennenmann, H., Watts, P., Haswell, S. J., Hessel, V., Löwe, H. Benchmarking of microreactor applications. *Org. Process Res. Dev.* **2004**, 8, 422-39.

7. Watts, P., Wiles, C., Haswell, S. J., Pombo-Vilalr, E., Styring, P. The synthesis of peptides using micro reactors. *Chem. Commun*. **2001**, 11, 990-1.

8. Wheeler, A. R., Throndset, W. R., Whelan, R. J., Leach, A. M., Zare, R. N., Liao, Y. H., Farrell, K., Manger, I. D., Daridon, A. Microfluidic device for single-cell analysis. *Anal. Chem*. **2003**, 75, 3581-6.

9. Trantidou, T., Elani, Y., Ces, O. Hydrophilic surface modification of PDMS for droplet microfluidics using a simple, quick, and robust method via PVA deposition. *Microsyst. Nanoeng.* **2017**, 3, 16091.

10.   Kalme, S., Kandaswamy, S., Chandrasekharmath, A., Katiyar, R., Rajamanickam, G. P., Kumar, S., Dendukuri, D. A hydrogel sensor-based microfluidic platform for the quantitative and multiplexed detection of fertility markers for point-of-care immunoassays. *Anal. Meth*. **2019**, 12, 1639-50.

11.   Ribeiro-Samy, S., Oliveira, M. I., Pereira-Veiga, T., Muinelo-Romay, L., Carvalho, S., Gaspar, J., Freitas, P. P., López-López, R., Costa, C., Diéguez, L. Fast and efficient microfluidic cell filter for isolation of circulating tumor cells from unprocessed whole blood of colorectal cancer patients. *Sci. Rep.* **2019**, 9, 8032.

12.   Wong, J. F., Simmons, C. A. Microfluidic assay for the on-chip electrochemical measurement of cell monolayer permeability. *Lab Chip*. **2019**, 19, 1060-70.

13.   Huh, D., Matthews, B. D., Mammoto, A., Montoya-Zavala, M., Hsin, H. Y., Ingber, D. E. Reconstituting organ-level lung functions on a chip. *Science*. **2010**, 328, 1662-8.

14.   Jacobson, S. C., Koutny, L. B., Hergenröder, R., Moore, Jr. A. W., Ramsey, J. M. Microchip capillary electrophoresis with an integrated postcolumn reactor. *Anal. Chem*. **1994**, 66, 3472-6.

15.   Melin, J., Quake, S. R. Microfluidic large-scale integration: the evolution of design rules for biological automation. *Annu. Rev. Biophys. Biomol. Struct.* **2007**, 36, 213-31.

16.   Mora, M. F., Greer, F., Stockton, A. M., Bryant, S., Willis, P. A. Toward total automation of microfluidics for extraterrestrial in situ analysis. *Anal. Chem*. **2011**, 83, 8636-41.

17.   Lagally, E. T., Simpson, P. C., Mathies, R. A. Monolithic integrated microfluidic DNA amplification and capillary electrophoresis analysis system. *Sens. Act. B. Chem*. **2000**, 63, 138-46.

18.   Mitchell, P. Microfluidics-downsizing large-scale biology. *Nat. Biotech*. **2001**, 19, 717-21.

19.   Garcia-Egido, E., Spikmans, V., Wong, S. Y. F., Warrington, B. H. Synthesis and analysis of combinatorial libraries performed in an automated micro reactor system. *Lab Chip*. **2003**, 3, 73-6.

20.   Easley, C. J., Benninger, R. K. P., Shaver, J. H., Head, W. S., Piston, D. W. Rapid and inexpensive fabrication of polymeric microfluidic device via toner transfer masking. *Lab Chip*. **2009**, 9, 1119-27.

21.   Haiducu, M., Rahbar, M., Foulds, I. G., Johnstone, R. W., Sameoto, D., Parameswaran, M. Deep-UV patterning of commercial grade PMMA for low-cost, large-scale microfluidics. *J. Micromech. Microeng*. **2008**, 18, 115029.

22.   Chin, C. D., Linder, V., Sia, S. K. Commercialization of microfluidic point-of-care diagnostic devices. *Lab Chip*. **2012**, 12, 2118-34.

23.   Gordon, M. J., Huang, X., Pentoney, Jr. S. L., Zare, R. N. Capillary electrophoresis. *Science*, **1988**, 242, 224-8.

24.   Landers, J. P. (1996). *Handbook of Capillary Electrophoresis*. Second Ed. New York City, New York: CRC Press.

25.   Yazdi, A. A., Popma, A., Wong, W. Nguyen, T., Pan, Y., Xu, J. 3D printing: an emerging tool for novel microfluidics and lab-on-a-chip applications. *Microfluid. Nanofluid.* **2016**, 20, 50.

26.   Chen, C., Mehl, B. T., Munshi, A. S., Townsend, A. D., Spence, D. M., Martin, R. S. 3D-prnited microfluidic devices: fabrication, advantages and limitations-a mini review. *Anal. Methods*. **2016**, 8, 6005-12.

27.   Waheed, S., Cabot, J. M., Macdonald, N. P., Lewis, T., Guijt, R. M., Paull, B., Breadmore, M. C. 3D printed microfluidic device: enablers and barrier. *Lab Chip*. **2016**, 16, 1993-2013.

28.   Engelhardy, S., Hoch, E., Borchers, K., Meyer, W., Krüger, H., Tovar, G., Gillner, A. Fabrication of 2D protein microstructures and 3D polymer–protein hybrid microstructures by two-photon polymerization. *Biofabrication*. **2011**, 3, 025003.

29.   Raimondi, M. T., Eaton, S. M., Laganà, M., Aprile, V., Nava, M. M., Cerullo, G, Osellame, R. Three-dimensional structural niches engineered via two-photon laser polymerization promote stem cell homing. *Acta Biomater*. **2013**, 9, 4579–84.

30.   Claeyssens, F., Hasan, E. A., Gaidukeviciute, A., Achilleos, D. S., Ranella, A., Reinhardt, C., Ovsianikov, A., Shizhou, X., Fotakis, C., Vamvakaki, M., Chichkov, B. N., Farsari, M. Three-dimensional biodegradable structures fabricated by two-photon polymerization. *Langmuir*. **2009**, 25, 3219–23.

31.   Bhargava, K. C., Thompson, B., Malmstadt, N. Discrete elements for 3D microfluidics. *Proc Natl Acad Sci USA*. **2014**, 111, 15013–8.

32.   Chen, C., Mehl, B. T., Munshi, A. S., Townsend, A. D., Spence, D .M., Martin, R. S. 3D-printed microfluidic devices: fabrication, advantages and limitations-a mini review. *Anal Methods*. **2016**, 8, 6005–12.

33.   Amin, R., Knowlton, S., Hart, A., Yenilmez, B., Ghaderinezhad, F., Katebifar, S., Messina, M., Khademhosseini, A., Tasoglu, S. 3D-printed microfluidic devices. *Biofabrication*. **2016**, 8, 022001.

34.   Lee, K. G., Park, K. J., Seok, S., Shin, S., Kim, D. H., Park, J. Y., Heo, Y. S., Lee, S. J., Lee, T. J. 3D printed modules for integrated microfluidic devices. *RSC Adv*. **2014**, 4, 32876–80.

35.   Bishop, G. W., Satterwhite-Warden, J. E., Bist, I., Chen, E., Rusling, J. F. Electrochemiluminescence at bare and DNA-coated graphite electrodes in 3D-printed fluidic devices. *ACS Sens*. **2016**, 1, 197–202.

36.   Anderson, K. B., Lockwood, S. Y., Martin, R. S., Spence, D. M. A 3D printed fluidic device that enables integrated features. *Anal Chem*. **2013**, 85, 5622–6.

37.   Lee, W., Kwon, D., Chung, B., Jung, G. Y., Au, A., Folch, A., Jeon, S. Ultrarapid detection of pathogenic bacteria using a 3D immunomagnetic flow assay. *Anal Chem*. **2014**, 86, 6683–8.

38.   Au, K. A., Lee, W., Folch, A. Mail-order microfluidics: evaluation of stereolithography for the production of microfluidic devices. *Lab Chip*. **2014**, 14, 1294–301.

39.   World Health Organization, Born too soon: the global action report on preterm birth, WHO, Geneva 2012.

40.   Centers for Disease Control and Prevention. Preterm birth. In: Maternal and Infant Health. CDC. 2018. https://www.cdc.gov/reproductivehealth/maternalinfanthealth/pretermbirth.htm. Accessed 17 Apr 2019.

41.   Behrman, R. E., Butler, A. S. Preterm birth: causes, consequences, and prevention. Washington DC: National Academies Press; 2007.

42.   Blencowe, H., Cousens, S., Oestergaard, M. Z., Chou, D., Moller, A. B., Narwal, R., Adler, A., Garcia, C. V., Rohde, S., Say, L., Lawn, J. E. National, regional, and worldwide estimates of preterm birth rates in the year 2010 with time trends since 1990 for selected countries: a systematic analysis and implications. *Lancet*. **2012**, 379, 2162-72.

43.   Institute of Medicine of the National Academies. Preterm Birth: Causes, Consequences, and Prevention, IOM, Washington, DC 2006.

44.   Roberts, D., Brown, J., Medley, N., Dalziel, S. R. Antenatal corticosteroid therapy for reduction of neonatal respiratory morbidity and mortality from preterm delivery. *Cochrane Data. Sys. Rev*. **2017**, CD004454.

45.   Al-Gubory, K. H., Fowler, P. A., Garrel, C. The roles of cellular reactive oxygen species, oxidative stress and antioxidants in pregnancy outcomes. *Int. J. Biochem. Cell Biol*. **2010**, 42, 1634–50.

46.   Buhimschi, I. A., Christner, R., Buhimschi, C. S. Proteomic biomarker analysis of amniotic fluid for identification of intra-amniotic inflammation. *BJOG.* **2005**, 112, 173–81.

47.   Fortunato, S. J., Menon, R. Distinct molecular events suggest different pathways for preterm labor and premature rupture of membranes. *Am. J. Obstet. Gynecol*. **2001**, 184, 1399-406.

48.   Petraglia, F., Imperatore, A., Challis, J. R. G. Neuroendocrine mechanisms in pregnancy and parturition. *Endocrine Rev*. **2010**, 31, 783–816.

49.   Esplin, M. S., Merrell, K., Goldenberg, R., Lai, Y., Iams, J. D., Mercer, B., Spong, C. Y., Miodovnik, M., Simhan, H. N., van Dorsten, R., Dombrowski, M., Proteomic identification of serum peptides predicting subsequent spontaneous preterm birth. *Am. J. Obstet. Gynecol*. **2011**, 204, 391.e1–8.

50.   Nováková, L., Vlcková, H. A review of current trends and advances in modern bio-analytical methods: chromatography and sample preparation. *Anal. Chem. Acta*. **2009**, 656, 8-35.

51.   Tighe P. J., Ryder, R. R., Todd, I. Fairclough, L. C. ELISA in the multiplex era: Potentials and pitfalls. *Proteom. Clin. App*. **2015**, 9, 406-22.

52.   Lim, S. L., Ichinose, H., Shinoda, T., Ueda, H. Noncompetitive detection of low molecular weight peptides by open sandwich immunoassay. *Anal. Chem*. **2007**, 79, 6193-200.

2. 3D PRINTER OPERATION AND RESIN DEVELOPMENT[*]

2.1   Introduction

Recent years have seen a steady increase in the number of publications using 3D printing to produce millifluidic devices.[1] One of the most promising types of 3D printers for making features small enough to be considered truly microfluidic is stereolithography (SLA). This technique uses a projector or laser to photopolymerize a liquid prepolymer resin into solid material. The prints are created one layer at a time to produce the 3D printed device.[1-4] To make successful microfluidic features, it is necessary to produce a small region of unpolymerized material which can later be cleared to reveal the desired features. Several different types of features can be created such as passive components like channels, mixers, reaction chambers and droplet generators[5-7] and active components such as valves and pumps.[8,9]

A number of different 3D printers and resins exist to attempt to make microfluidic features; however, these printers and materials are generally incapable of producing features small enough for most microfluidic applications.[10,11] As a result, the smallest published 3D printed microfluidic channels prior to Nordin and Woolley's collaborations are 250 μm × 250 μm,[6] 400 μm × 400 μm,[7] and 500 μm × 500 μm.[5] In all cases except for this work, commercial resins were used. Importantly, these features are in the milli-fluidic, rather than microfluidic size range, such that a critical need exists to develop methods to significantly reduce 3D printed

---

microchannel sizes. In previous work with an unoptimized custom resin, my own group has fabricated 250 mm x 350 mm flow channels.[8]

In September 2015 Nordin's group evaluated the minimum flow channel size that can be fabricated at four commercial 3D printing service bureaus. They submitted a design shown in Figure 2.1A, which has windows varying from 700×700 μm to 50×200 μm and table shaped membranes which are 50 μm thick. Only one service specifies a minimum flow channel size (500 μm $\times 500$ μm). They found that they and another service were successful in printing channels as small as 350 mm $\times$ 350 mm with the test design. In addition, only one of the services was able to successfully produce the 50 μm thick membrane. This demonstrated the inability for currently available services to adequately provide microfluidic devices for many applications, especially where small channels are required.
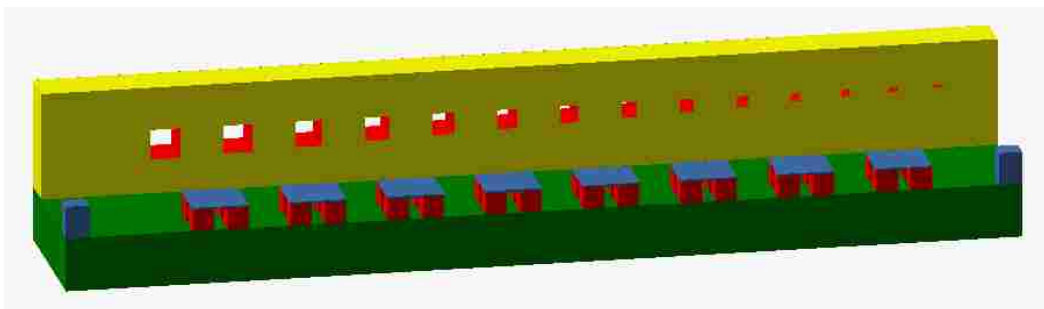
Figure 2.1 Design submitted to online 3D printing services. The device features channels 700×700 μm to 50×200 μm and table shaped membranes 50 μm thick.

In addition to working with optimized resin materials for making devices, the ability to 3D print microfluidics also depends on the printer used. Nordin's group has developed a custom-built 3D printer for producing microfluidics based on a high-resolution projector and vertical stage.

In this chapter, I focus on custom formulation of resins in addition to their use in a custom-built 3D printer that enable much smaller flow channels. Specifically, I used a mathematical model developed by Nordin[12] for the total optical dose delivered as a function of depth through a 3D printed device, including void regions, to guide the formulation of custom resins. I measured the absorptivity of various resins and used the most promising candidates to see how small of microfluidic channels they could print using the commercially available Asiga Pico Plus 27 3D printer. These results led to the development of general rules for minimum achievable flow channel size given a resin's optical properties, and allowed a fellow graduate student, Hua Gong, to demonstrate reliable fabrication of flow channels as small as 60 µm × 108 µm. Importantly, this analysis indicates how to achieve even smaller dimension channels. To this end I helped identify possible resin components and test their use to make microfluidic channels using various selection criteria such as solubility, absorptivity, and rigidity of the finished print. In addition, I measured the spectral properties of currently available commercial 3D printing resins for comparison to the model and examined the flow channel sizes they were able to print.

2.2   Experimental Section

2.2.1   Material Sources

Poly(ethylene glycol) diacrylate (PEGDA), triethoxysilyl propyl methacrylate, di(trimethylolpropane) tetraacrylate (DTPTA), trimethylolpropane ethoxylate triacrylate (TPET), 2-[[(butylamino)carbonyl]oxy]ethyl acrylate (BACA), and 2,5-bis(5-*tert*-butyl-benzoxazol-2-yl) thiophene (TBT), Martius Yellow, morin hydrate, quinoline yellow, 3,3′,4′,5,6-pentahydroxyflavone (Quercetin), and Sudan I were purchased from Sigma-Aldrich (St. Louis, MO). 4,4′-bis(2-sulfonatostyryl) biphenyl (Benetex OB-M1), nitrofurazone, and 2-nitrophenyl

phenyl sulfide (NPS) were purchased from TCI America (Portland, OR). 2,3,6,7-tetrahydro-9-methyl-1*H*,5*H*-quinolizino-(9,1-gh) coumarin (Coumarin 102), triamterene, and 9,10-diethoxyanthracene were purchased from Alfa Aesar (Haverhill, MA). 5,12-naphthacenequinone (NATQ) and phenazine were purchased from Santa Cruz Biotechnology (Dallas, TX). Salicylaldehyde and 2-propanol (IPA) was purchased from Thermo Fisher Scientific (Waltham, MA). Avobenzone and octocrylene were purchased from Making Cosmetics (Snoqualmie, WA). Phenylbis (2,4,6-trimethylbenzoyl) phosphine oxide (Irgacure 819) was provided by BASF (Midland, MI). Benzenepropanoic acid (BLS 99-2) was purchased from Mayzo (Suwanee, GA). UV386A was purchased from QCR Solutions (St. Lucie, FL). Ethyl(2,4,6-trimethylbenzoyl) phenylphosphinate (TPO) was purchased from Combi-Blocks (San Diego, CA). FSL Clear 3D printing resin was purchased from Full Spectrum Laser (Las Vegas, NV). PlasClear 3D printing resin was purchased from Proto Products (Ashland City, TN).

2.2.2   3D Printing

All custom-formulated 3D printing resins were prepared (w/w) using the following protocol except PR48: PEGDA was used as the base monomer and 1% Irgacure 819 was used as the photoinitiator. For each specific resin, the indicated amount of UV absorber was added and the mixture was sonicated until all components were dissolved. Prepared resins were stored in amber glass bottles wrapped in aluminum foil to protect them from light. The PR48 resin was prepared by mixing (w/w) 40% each of DTPTA and TPET with 20% BACA. 0.16% TBT and 0.4% TPO were added as the UV absorber and photoinitiator, respectively. The rest of the resin preparation procedure was the same.

Two different 3D printers were used for this work. First, the commercially available Asiga Pico Plus 27 was used for work with the Sudan I, Plasclear, FSL Clear and PR48 resins. This printer has 27 μm resolution in the X-Y plane and Z resolution of 1 μm, and the light source operates at 412 nm with a total projector area of 21.2 mm × 33.8 mm. The second printer is a custom-built 3D printer based on a Visitech light engine. This projector has a 385 nm light source with a pixel size of 7.6 μm in the image plane with a total image size of 19.4 mm × 12.1 mm. A heavily modified Solus 3D printing mechanism (Junction3D, Santa Clarita, CA) serves as the vertical stage with a Z resolution of <1 μm.[13]

After prints were completed in either printer, they were removed from the build platform and washed with IPA. Fluidic features such as channels were flushed with additional IPA and vacuum. Prints were post-cured under a broad UV light source (54 Watt Professional UV Nail Dryer, Royal Nails, Rixheim, France).

All prints were printed on a silanized glass slide. Glass microscope slides 1 mm thick were scored into 1″ squares on one face with a laser cutter (Universal Laser Systems, Scottsdale, AZ). The setting for the laser cutter were 50% power, 10% speed and 165 pulses per inch. The glass slides were then washed with acetone and IPA and dried. The glass slides were then submerged in a freshly prepared 10% (v/v) solution of triethoxysilyl propyl methacrylate in toluene for at least 2 hours. After treatment, the glass slides were washed with IPA, dried and broken along the score marks to the desired size. They were stored under toluene until use.

3D printing designs were created in the open source CAD software OpenSCAD (openscad.org). Several different designs were used in this work and will be shown as they are discussed in Section 2.3.

Spectral properties of resins and 3D printer light sources were measured through a 100 μm optical fiber connected to a QE65000 spectrometer from Ocean Optics (Dunedin, FL) using a XCITE-12Q broadband source for the resins (Lumen Dynamics, Ontario, Canada). Resin spectrum measurements were made by placing a small amount of resin between a glass slide and coverslip separated by two 65 μm spacers. The molar absorptivity of each absorber was calculated from the concentration in the resin using resin without the absorber as a blank.

Imaging for completed prints was done using two techniques. Photographs of printed parts were taken using an Optixcam Summit K2 CCD camera (Roanoke, VA) which was mounted to an Olympus BX60 microscope (Center Valley, PA) through either the 5× or 10× objectives. Prints were prepared for SEM imaging by removing the print from the glass slide using a razor blade and then cutting the print so the desired channel could be imaged. The prints were fixed to a stage with conductive tape and sputter coated with 80:20 Au/Pd. SEM images were taken using an ESEM XL 30 FEI (Thermo Fisher, Fairlawn, NJ) in high vacuum mode and a 10 kV beam voltage. The resulting channel size was measured with ImageJ (NIH, Bethesda, MD).

2.3   Results and Discussion

The first step in the assessment of commercial materials to 3D print microfluidic features that I was involved with was to use a commercially available 3D printer but develop custom 3D printing resins for use with it. For this work, the Asiga Pico Plus 27 was used because it had the highest resolution of SLA 3D printers commercially available. The monomer chosen to make up the base of the resin is PEGDA which has been previously demonstrated to work well as a microfluidic material due to low nonspecific adsorption of biomolecules, optical clarity, water

stability and low background fluorescence.[14] For the photoinitiator and UV absorber, I examined the UV source used in this 3D printer because it is necessary to have appropriate spectral overlap between the projected light and the absorption of the resin. The measured spectrum for this printer can be seen in Figure 2.2 showing the peak emission at 411.8 nm.
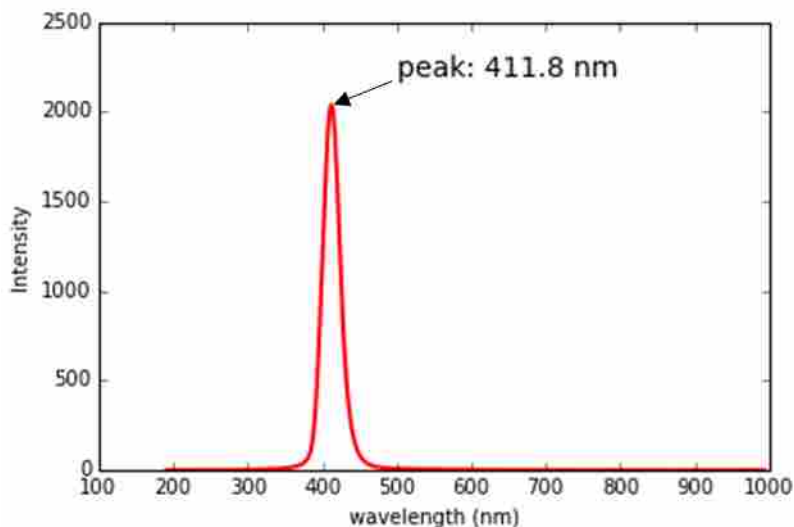

Figure 2.2 Measured spectrum of Asiga 3D printer light source. The peak emission is indicated at 411.8 nm.

With the source spectrum known, I could begin searching for potential UV absorbers to use in a resin formulated specifically for this printer. After an extensive literature and internet search several possible candidates were identified. To efficiently examine this initial library of compounds a fellow graduate student, Hua Gong, and I divided them up and I primarily focused on the following compounds: Martius Yellow, quercetin, salicylaldehyde, UV386A, avobenzone, and octocrylene. These potential UV absorbers were evaluated based on several selection criteria such as solubility in PEGDA, absorbance of the source light, and stability of the produced print.

The first analysis was the solubility test, because if the potential absorber candidates were insoluble in the resin, little else could be tested and they would be eliminated from consideration.

Of the compounds tested salicylaldehyde, avobenzone, and octocrylene were found to be highly

soluble (>5%), Martius Yellow was soluble to 3%, quercetin was soluble to 0.8% and UV386A

was found to be insoluble. The solubility results eliminated the UV386A from use, and the

remaining compounds' spectral properties were tested.

The absorption spectra for the remaining compounds were measured using a small

amount of resin without the photoinitiator. The background subtracted spectra can be seen in

Figure 2.3. From the spectra seen two main trends can be observed. First, the molar absorptivity

at 412 nm (the peak emission of the printer) for most of the absorbers is low. This means that

salicylaldehyde, octocrylene and avobenzone are not well suited to work in the resin with this

light source. Second, different absorbers have different absorptivities meaning that different

concentrations will be required to obtain the same degree of optical control in the resin. For this

reason, both the solubility and absorptivity of the UV absorber need to be considered for resin
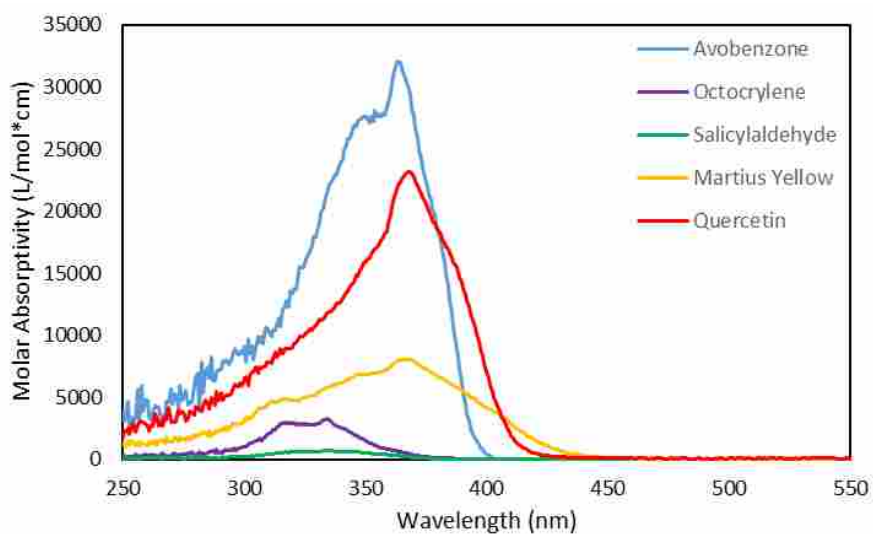
formulation.

Figure 2.3 Molar absorptivity of UV absorber candidates.

To aid in this analysis, Prof. Nordin has developed a mathematical model to describe the penetration of light during an SLA 3D printing process.[12] This model accounts for the penetration of light into a printing resin beyond the layer currently being printed, i.e. into a void area where a channel is being formed. The model is based on Beer's Law and defines the dose of light necessary to cause full polymerization of resin at a depth into the material. Some of the key parameters identified were T_c which was the critical time to reach a given dose of irradiation and h_a which is the penetration depth. T_c gives the minimum light exposure time needed to polymerize the resin for a given thickness and h_a will give information about the absorptivity of the resin. Both of these factors are dependent on the concentration of absorber in the resin and were determined experimentally for several resin formulations. The same design that was submitted to the online printing services was also used for these purpose (Fig. 2.1). Here the table features were designed to be one 50 µm thick layer. The produced layer thickness could then be measured at various exposure times. An example of one of these printed membranes can be seen in Figure 2.4A using a 0.2% Martius Yellow resin. By measuring the membrane thickness at several exposure times, I was able to determine h_a and T_c for several resin formulations. An example of the type of plot created is shown in Figure 2.4B for a resin composed of 0.2% Martius Yellow in PEGDA. For this resin, the h_a and T_c were determined to be 150 µm and 0.41 s, respectively. Resins with lower h_a values mean the resin absorbs light more strongly and there is less penetration of the light beyond the layer currently being printed. This results in better control of the light and ultimately smaller microfluidic features.
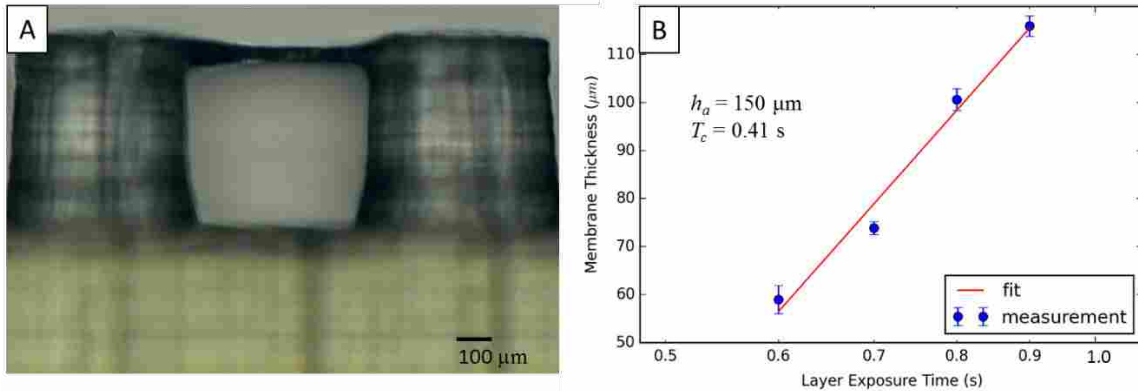
Figure 2.4 Photograph and plot used to measure h_a and T_c for resin compositions. A) Device photograph through 5× objective of table design to measure the thickness of a printed layer. B) Plot of measured membrane thicknesses at various exposure times for 0.2% Martius Yellow resin. The measured h_a and T_c for this resin are listed in the figure and 150 μm and 0.41 s, respectively.

The next step for the resin, after quantifying its absorptivity, was to see how small of channels could be printed. This was accomplished using the same design as was used for the h_a measurements because it also contained short (1.08 mm) channel features of varying heights and widths. The resulting windows could be examined to determine if the channel was open. Figure 2.5 shows an example channel made in 2.0% Martius Yellow resin which measures approximately 250 μm tall and 190 μm wide. Working with alternative UV absorbers and additional resin formulations, my colleague Hua Gong, was able to produce channels as small as 60×108 μm^2 (H × W) using a 0.6% Sudan I resin demonstrating the advantages of considering SLA resins from an optical perspective to create microfluidic features. Based on the experimental results of channels printed from resin formulations, Prof. Nordin developed general guidelines regarding the size of channels that could be produced from a resin with its corresponding absorptivity (h_a). In general, resins were able to produce channel heights about 3.5-5.5 × h_a depending on its magnitude with higher h_a values typically leading to relatively taller channels. The channel width was largely independent of h_a with most channels being about 4 projector pixels wide.[13]
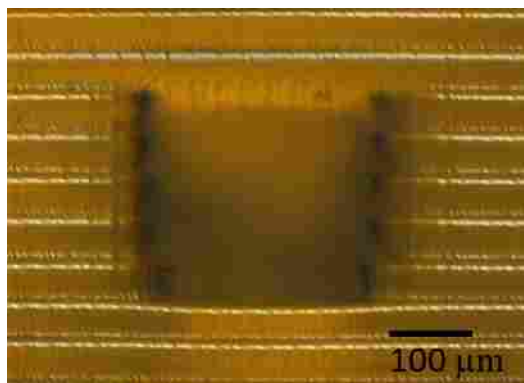
28

Figure 2.5 Example microfluidic channel produced using an Asiga Pico Plus 3D printer. The channels dimensions measure 250 µm tall, 1.08 mm long, and 190 µm wide. This channel was printed using 2.0% Martius Yellow resin.

Using the developed model, I also evaluated two commercially available resins, PlasClear and FSL Clear, and a published 3D printing recipe from AutoDesk for a resin called PR48. These three resins were tested using the same h_a determining procedure described previously. The measured h_a values for the resins are 120 µm for PlasClear, 320 µm for FSL Clear, and 80 µm for PR48. Figure 2.6 shows the resulting channels from these materials. In Fig 2.6 A and B the produced channels were very large and not all of the channel could be imaged by the microscope CCD camera using the widest-angle objective so the channel bottom was placed in the field of view with the top of the channel extending beyond the frame. For even these channel sizes a large amount of material can be seen partially blocking the channel (dark colored material in the top half of the channel view). The resulting minimum channel sizes that could be printed were 1000×540 µm^2 for PlasClear, 1100×810 µm^2 for FSL Clear, and 400×190 µm^2 for PR48. It is worth noting those the viscosities for all these commercial materials were significantly higher than that of any of the PEGDA based resins, which made it difficult to fully flush even short (1.08 mm) channels. This likely contributed to the large channel sizes produced, especially the widths of the channels.
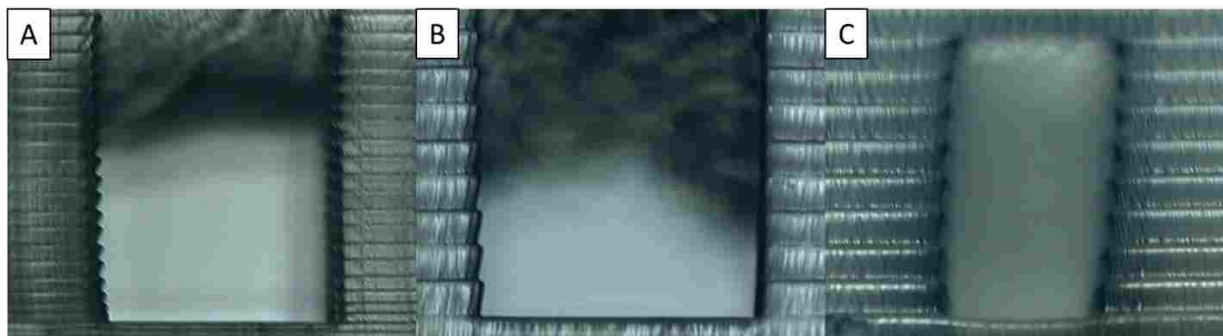
29

Figure 2.6 3D printed channels using commercial resin formulations. A) PlasClear channel measuring 1000×540 μm^2. B) FLS Clear channel measuring 1100×810 μm^2. Because of the large size of these two channels, not all of the channel could be imaged with the microscope CCD with the widest view. C) PR48 channel measuring 400×190 μm^2.

At this point, my efforts were focused mostly on working towards µCE separations of amino acids and PTB biomarkers (see chapter 4); however, additional work continued to be done to develop even better 3D printers and resins for microfluidic devices. This work was conducted in the Nordin lab by Hua Gong and is key to the subsequent chapters as it formed the basis of both printer and materials used for those devices as well as the rationale for the full characterization of this printer in chapter 3. In the continued work, a custom built SLA 3D printer was created with 7.6 µm pixel resolution in the X-Y plane and <1 µm resolution with the Z stage. Using the same optical approach to determine the optimal resin composition, the projector was measured to operate at 383 nm and Hua Gong, Bryce Bickham and I identified a number of potential UV absorber candidates for solubility, absorptivity, mechanical strength, and fluorescence testing. This list included avobenzone, Benetex OB+, Benetex OB-M1, BLS 99-2, Coumarin 102, Martius Yellow, morin hydrate, nitrofurazone, NPS, NTAQ, octocrylene, phenazine, POPOP, quinoline yellow, quercetin, salicylaldhyde, Sudan I, triamterene, UV386A and UVS-1101. From these, a 3% NPS resin was shown to have the ability to print microfluidic channels as small as 18×20 μm^2.[13] For routine processing and function, however, 2% NPS and 35×50 μm^2 channels are more commonly used.

This chapter demonstrates the importance of undertaking fundamental studies for the development and evaluation of 3D printing resins. Selection criteria for UV absorbers were demonstrated on the basis of solubility and spectral overlap (absorptivity). The importance of measuring the source spectrum and matching the absorptivity of the UV absorber to that of the source was found to be a critical aspect of formulating a resin capable of printing truly microfluidic channels. From this analysis, channels as small as $60 \times 108 \ \mu m^2$ were printed using a custom resin formulation and a commercial 3D printer. The mathematical model was also extended to commercially available resins, PlasClear and FSL Clear, as well as a published recipe, PR48. This work lays the foundation for the ability to 3D print truly microfluidic channels by optimizing custom resin formulations.

2.4 References

1.   Ho, C. M. B., Ng, S. H., Li, K. H. H., Yoon, Y. J. 3D printed microfluidics for biological applications. *Lab Chip*. **2015**, 15, 3627-37.

2.   Lu, Y., Mapili, G., Suhali, G., Chen, S., Roy, K. A digital micro-mirror device-based system for the microfabrication of comlex, spatially patterned tissue engineering scaffolds. *J. Biomed. Mater. Res. Part A*, **2006**, 77, 396-405.

3.   Melchels, F. P. W., Feijen, J., Grijpma, D. W. A review on stereolithography and its applications in biomedical engineering. *Biomaterials*. **2010**, 31, 6121-30.

4.   Gross, B. C., Erkal, J. L., Lockwood, S. Y., Chen, C., Spence, D. M. Evaluation of 3D printing and its potential impact on biotechnology and the chemical sciences. *Anal. Chem.* **2014**, 86, 3240-53.

5.   Bhargava, K. C., Thompson, B., Malmstadt, N. Discrete elements for 3D microfluidics. *Proc. Natl. Acad. Sci. U. S. A.* **2014**, 111, 15013-8.

6.   Shallan, A. I., Smejkal, P., Corban, M., Guijt, R. M., Breadmore, M. C. Cost-effective three-dimensional printing of visibly transparent microchips within minutes. *Anal. Chem.* **2014**, 86, 3124-30.

7.   Au, A. K., Lee, W., Folch, A. Mail-order microfluidics: evaluation of stereolithography for the production of microfluidic devices. *Lab Chip*. **2014**, 14, 1294-301.

8.   Rogers, C. I., Qaderi, K., Woolley, A. T., Nordin, G. P. 3D printed microfluidic devices with integrated valves. *Biomicrofluidics*. **2015**, 9, 016501.

9.   Au, A. K., Bhattacharjee, N., Horowitz, L. F., Chang, T. C., Folch, A. 3D-printed microfluidic automation. *Lab Chip*. **2015**, 15, 1934-41.

10.   Nge, P. N., Rogers, C. I., Woolley, A. T. Advances in microfluidic materials, functions, integration, and applications. *Chem. Rev.* **2013**, 113, 2550-83.

11.   Mark, D., Haeberle, S., Roth, G., Von Stetten, F., Zengerle, R. Microfluidic lab-on-a-chip platforms: requirements, characteristics and applications. *Chem. Soc. Rev.* **2010**, 83, 6418-25.

12.   Gong, H., Beauchamp, M., Perry, S., Woolley, A. T., Nordin, G. P. Optical approach to resin formulation for 3D printed microfluidics. *RSC. Adv*. **2015**, 5, 106621-32.

13.   Gong, H., Bickham, B. P., Woolley, A. T., Nordin, G. P. Custom 3D printer and resin for 18×20 μm microfluidic flow channels. *Lab Chip*. **2017**, 17, 2899-909.

14.   Rogers, C. I., Pagaduan, J. V., Nordin, G. P., Woolley, A. T. Single-monomer formulation of polymerized polyethylene glycol diacrylate as a nonadsorptive material for microfluidics. *Anal. Chem*. **2011**, 83, 6418-25.

3. 3D PRINTED MICROFLUIDIC FEATURES USING DOSE CONTROL IN X, Y, AND Z DIMENSIONS[*]

3.1 Introduction

3D printing is a valuable technique for custom and rapid design change and optimization in fabrication of millifluidic devices.[1] Miniature device applications stand to benefit from the advantages offered from 3D printing, such as the ability to create and test devices with rapid feedback allowing changes to be quickly tested. Device optimization based on empirical results could save time and money compared to traditional device fabrication techniques that involve conventional machining or micromachining.

A number of groups have recently sought to use 3D printing to produce fluidic devices for various applications. Devices for nitrite[2] or anemia[3] detection, measuring endocrine secretion,[4] sorting bacteria,[5] and cell culture[6-7] have all been shown. Although these are promising assays, a key issue from these works is the size of printed features. Most commercially available printers and resins are only able to achieve feature sizes down to 250 μm, with typical features around 500 μm, which are not suitable for many microfluidics applications. Additionally, these commercial printers lack flexibility in terms of resin development, individual layer custom exposure time control, or multiple exposures per layer. For 3D printing of fluidic devices with low surface roughness, stereolithography (SLA) printers are the best suited.[8] The material left in the channels after printing is a liquid and thus is much easier to clear than solid

---

[*] Portions of this chapter are adapted with permission from Beauchamp, M. J., Gong, H., Woolley, A. T., Nordin, G. P. 3D printed microfluidic features using dose control in X. Y, and Z dimensions. *Micromachines*, **2018**, *9*, 326.

33

sacrificial materials formed with either polyjet or fused deposition modeling printers.[9-11] Reviews of 3D printing over the past several years have offered helpful insights regarding types of printers and their applications. Many different outlooks are given for future directions in 3D printing of fluidic devices, such as resin improvements, material removal techniques, throughput, and printer resolution.[1,12-16]

Dr. Nordin's group has previously developed an SLA 3D printer as well as a custom resin formulated specifically for creating truly microfluidic structures with this printer,[17] having made small (18 x 20 μm) microfluidic channels,[18] as well as fluid control systems involving pumps and valves.[19] To make the smallest channels, an edge compensation technique was employed which overexposed the pixels at the channel edge to make it narrower.[18] However, how this edge compensation approach affects features in the channels had not been examined previously.

In this chapter, I investigate precise control over printing exposure areas and dosage conditions to create microscale substructures within microfluidic features. First, I examine positive and negative features on the exterior of prints to see what size features can be printed with various exposure times and with exposure edge compensation. Next, I evaluate positive and negative features in interior void areas to see the impact of exposure times and edge compensation. Finally, I create microfluidic particle traps to demonstrate how the ability to control specific dosing parameters allows improved function.

3.2   Experimental Section

3.2.1   Material Sources

Acetone, 2-propanol (IPA), and 25 μm polystyrene microspheres were purchased from Thermo-Fisher Scientific (Salt Lake City, UT). Triethoxysilyl propylmethacrylate,

hydroxypropyl cellulose (HPC), and polyethylene glycol diacrylate (PEGDA, 258 Da MW) were purchased from Sigma-Aldrich (Milwaukee, WI). Toluene and glass microscope slides (3" x 1" x 1.2 mm) were purchased from Avantor (Center Valley, PA). 2-Nitrodiphenylsulfide (NPS) was purchased from TCI America (Portland, OR). Phenylbis(2,4,6-trimethylbenzoyl)phosphine oxide (Irgacure 819) was provided by BASF (Midland, MI). All chemicals were used as received.

3.2.2 Printing Setup

Glass microscope slides were scored on one side using a laser cutter (Universal Laser Systems, Scottsdale, AZ). The settings for cutting were 50% power, 10% speed and 165 points per inch. The glass slides were then broken along the scored mark, washed with acetone and IPA, and dried with air. A fresh preparation of 10% triethoxysilyl propylmethacrylate in toluene was made. Glass slides were submerged in this silane solution in a shallow covered dish for a minimum of two hours after which they were rinsed with IPA and dried with air. For longer term storage, slides were kept in a container under toluene.

The resin was prepared by mixing 2% NPS with 1% Irgacure 819 in 97% PEGDA. The resin was sonicated until all solid components dissolved and was stored in an amber bottle wrapped in aluminum foil to protect it from light.

The 3D printer used for this work is the same as described in reference 18. This printer operates with a nominally 385 nm light source and 7.6 µm pixel size in the image plane. The build layer height for all prints was 10 µm, the image plane irradiance was 21.2 mW·cm^{-2}, and the exposure time was chosen to be either 500, 750, 1000, or 1500 ms. To ensure thorough attachment of the print to the glass slide the first four layers were overexposed for 20, 10, 5 and 1 seconds, respectively. For prints where the normal layer exposure time exceeded 1 second, only

the first three layers were exposed in this manner. After printing, the remaining liquid resin in the print was flushed out with IPA and the device was cured under an 11 mW 430 nm LED (ThorLabs, Newton, NJ) for 10 minutes before use.

An edge compensation technique similar to the one in reference 18 was used where indicated for both interior and exterior trenches (negative features). This technique exposes the two pixels forming the edge of the trench for double the normal exposure time. The purpose of this technique is to cause a wider trench design to be narrower when printed. For example, a 3D printed trench that is designed to be 4 pixels wide without compensation may have the same width as a 6 pixel wide design formed with compensation as the two pixels at the channel edge will receive additional light exposure.

3.2.3 Printing Designs

Designs for 3D printed parts were made using open source OpenSCAD software (openscad.org). Schematics of the resolution prints can be seen in Figure 3.1. For the exterior ridges (Figure 3.1A) and trenches (Figure 3.1B), the features are 100 µm tall or deep, and the widths are from 1 to 10 pixels (7.6 to 76 µm), with a spacing between individual ridges or trenches of 100 pixels.

For the interior resolution features (Figure 3.1C), the height of the feature area is 100 µm. The internal ridges are all 5 pixels wide, 250 pixels long, and have heights from 1 to 10 layers (10 to 100 µm). For the trench sections, the trenches are all 100 µm deep and vary in width from 1 to 10 pixels. The pillars are designed with diameters ranging from 1 to 10 pixels, and all of the pillars in a given row are identical. In between each internal feature (or set of features with the

pillars) is a support beam to help hold up the microchannel ceiling. These ceiling supports are all 5 pixels wide and go from the floor of the feature areas to the ceiling.

The trapping devices consist of 6 straight channels 30 pixels wide and 8 layers tall with fluidic reservoirs at both ends (Figure 3.1D). The traps consist of two L-shaped pieces facing each other that are 8 pixels long, 4 pixels wide and spaced 2 pixels apart (Figure 3.1E). The traps are spaced 20 pixels apart down the length of the channel. Each print contains 6 different channels for testing a variety of trap layouts. Three different configurations of the traps were tested: one with traps only down the center of the channel, one with traps staggered along the edges, and one with traps staggered in the middle of the channel and along the sides (see Figure 3.1D, insets).
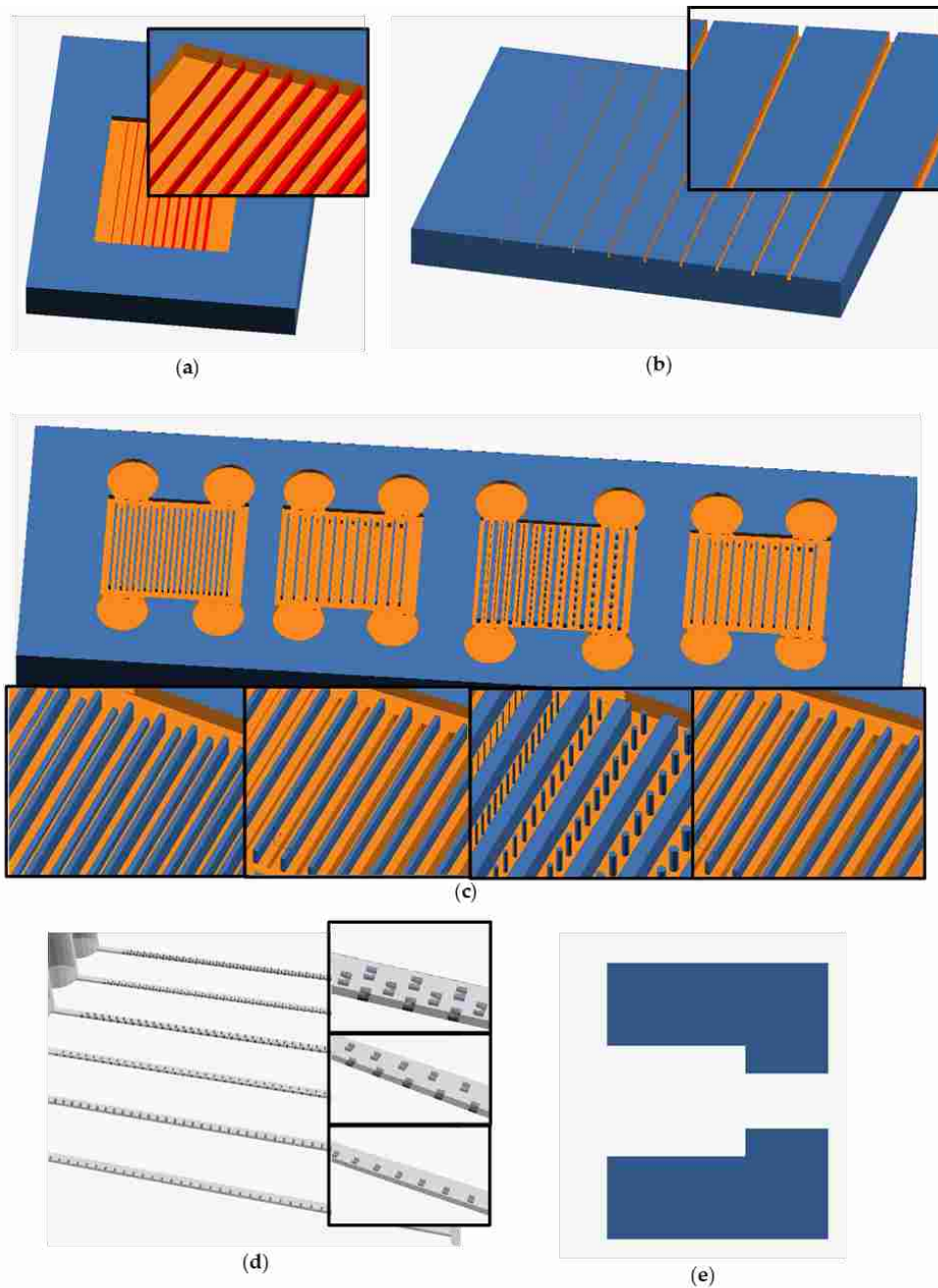
Figure 3.1 OpenSCAD designs of prints for exterior and interior resolution features. (**a**) Ridge device. The ridges are shown in red and there is a support box around the ridges. The ridges are 100 μm tall and have widths of 1-10 pixels (7.6-76 μm) from left to right. The cutout shows a zoom view. (**b**) Trench device with the trenches shown in orange. The trenches are 100 μm deep and have widths of 1-10 pixels (7.6-76 μm) from left to right. The cutout shows a zoom view. (**c**) Interior features device. The top layers of the device have been removed in the schematic to show the features. From left to right the regions are ridges, trenches with exposure compensation, pillars, and trenches without exposure compensation. Each set of features has a series of ceiling support ridges running the length of the feature area. Below each feature void area is a zoom view. (**d**) Bead trap device design showing 6 channels and traps within channels. Insets show a zoom view of the three different trap layouts. (**e**) Schematic of bead trap. The large gap is designed to allow the beads to enter and the smaller gap allows fluid to pass through the trap.

3.2.4 Measurement of Print Features and Bead Trapping Details

Exterior feature heights, depths, and widths were measured using a Zeta 20 optical profilometer (Zeta Instruments, San Jose, CA). The width was measured as the full width at half height or depth. SEM imaging was done using an ESEM XL30 (FEI, ThermoFisher Scientific). Samples were prepared by cutting them open with a razor blade and sputtering with 80:20 Au:Pd to allow the side profile to be observed. Images were processed using ImageJ (NIH) to measure the widths and heights of interior pillars, ridges, and trenches.

For trapping experiments, imaging was done using a Zeiss AXIO Observer A1 inverted microscope (Thornwood, NY) using a 10x objective connected to a Photometrics coolSNAP HQ2 CCD camera (Tucson, AZ). The exposure time for the CCD was 10 ms. The images were recorded and processed using ImageJ.

The bead solution for trapping was made by suspending the beads in deionized water at a concentration of 1 mg/mL with 0.5% HPC to prevent aggregation. 1.5 µL of bead solution was pipetted into the left reservoir as oriented in Figure 1D and drawn through the channel with vacuum over ~7 seconds, which resulted in a flow rate of 13 µL/min. This was repeated three times so a total of 4.5 µL of bead solution was pulled through the channel, after which CCD images were taken.

3.3 Results and Discussion

The full data set of photographs and SEM images for the exterior and interior resolution features, as well as their measured sizes can be found in Appendix A. The following sections present the summarized results.

3.3.1 Exterior Features

3.3.1.1 Ridges

Initial resolution testing focused on the exterior features created by our 3D printer by testing a set of ridges and trenches on the surface of prints. The purpose of these features is to evaluate how positive features formed on the surface of print. For the surface ridges, the design shown in Figure 3.1A was created; the design was printed three times with exposure times of 500, 1000, or 1500 ms for each build layer. I found that the ends of the ridges became warped when they were not anchored, so a support box was placed around the ridges. A photograph though the microscope can be seen in Figure 3.2A showing example ridges that are 3 and 4 pixels wide for 1500 ms exposure. The heights and widths of these features were then measured with an optical profilometer. Figure 3.3A shows the measured ridge width plotted against the designed width, for ridges which reached >90% of the full height. This shows that increasing light dosage from 500 ms (blue line in Figure 3.3A) to 1500 ms (red line in Figure 3.3A) allows smaller ridges to successfully reach full height and be closer to their designed width. Additionally, a ridge that is designed to a certain width will print smaller than expected if the exposure time is insufficient. The minimum width ridge that could be successfully printed was 30 μm which was with an exposure time of 1500 ms. These positive features benefit from increased light exposure, indicating the need to be able to give sufficient exposure to positive features.

3.3.1.2 Trenches

For the exterior negative features, I created the design shown in Figure 3.1B. This design was printed with and without the exposure compensation pattern at 500, 1000, and 1500 ms for a total of six prints. An example microscope image showing a trench 4 pixels wide with 500 ms exposure can be seen in Figure 3.2B. The heights and depths of these trenches were measured with optical profilometry. As seen in Figure 3.3B measured width was plotted against designed width; only the features which achieved >90% of the designed feature depth were included. The first observation is that the compensation pattern caused the trenches to turn out narrower than the uncompensated devices due to the additional exposure at the trench edge. The second effect that can be seen is that increasing the layer exposure time for the uncompensated case results in narrower trenches, as expected. Finally I note that, to achieve a minimum trench width at full depth, there are three different possibilities: 500 ms exposure without compensation, 1000 ms exposure without compensation, or 1000 ms exposure with compensation. All three of these approaches produced a trench 100 μm deep and about 20 μm wide; however the designed widths were all different (4, 5 and 6 pixels, respectively). These results show that having precise control over both exposure and printing parameters allows for careful control of final feature sizes for exterior trenches.

41
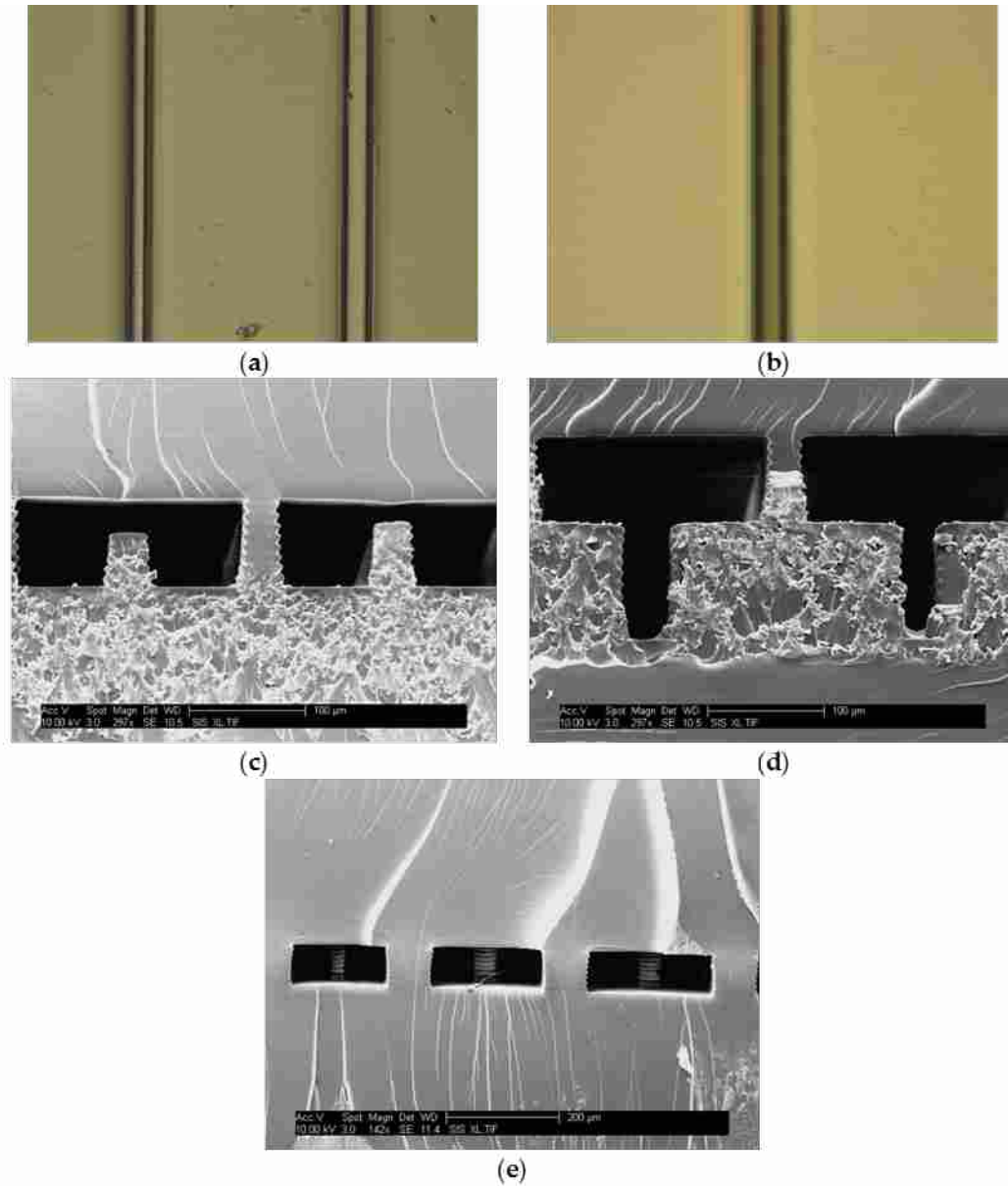
Figure 3.2 Images of 3D printed resolution features. (**a**) Top view photograph of 1500 ms exposure ridges designed 3 and 4 pixels (23 and 30 µm) wide. The ridges measured 25 and 29 µm. (**b**) Top view photograph of a 500 ms exposure (without compensation) trench designed 4 pixels (30 µm) wide, which measures 20 µm. (**c**) SEM images of 1000 ms exposure interior ridges designed 5 and 6 layers tall. The ridges measured 46 and 55 µm tall, respectively; a support pillar is in the middle of the image. (**d**) SEM image of interior trenches at 1000 ms exposure without compensation designed 5 and 6 pixels (38 and 46 µm) wide, which measured 22 and 34 µm wide. (**e**) SEM image of interior pillar structures at 1500 ms exposure designed to be 5-7 pixels (38-53 µm) in diameter.
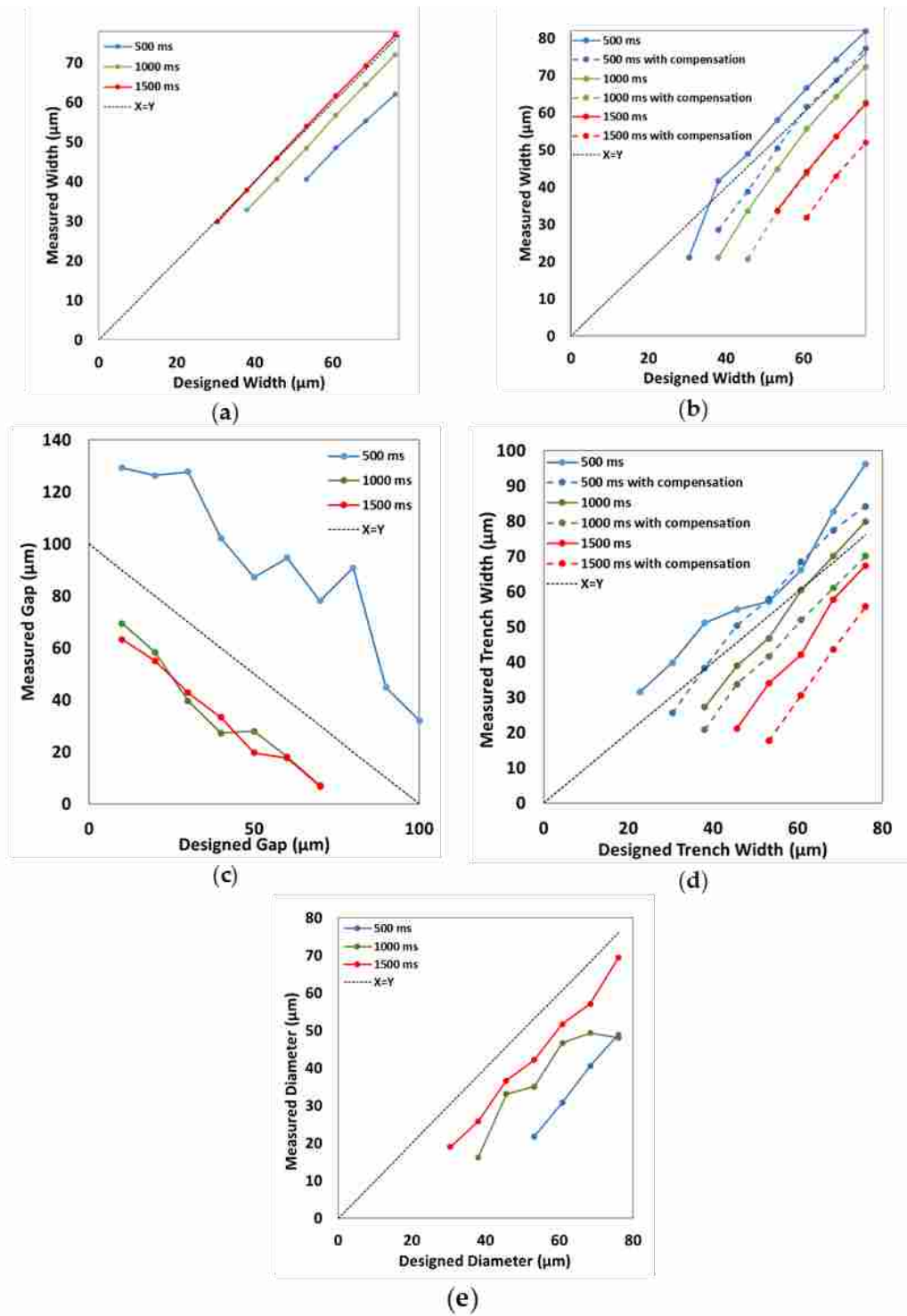
Figure 3.3 Designed feature width versus measured width for different exposure conditions. Only features which reached >90 µm in height (ridges) or depth (trenches) were included. For the pillars, only those that were attached floor to ceiling were included. (a) Exterior ridges. (b) Exterior trenches. (c) Interior ridges. (d) Interior trenches. (e) Interior pillars.

3.3.2   Interior Features

For interior feature resolution, I undertook a similar study of positive and negative features in a confined space according to the design in Figure 3.1C. When prototyping this design, I found that a large void space without a support for the ceiling resulted in irregular top layers and erratic feature measurements. Thus, an alternating pattern of feature and ceiling support pieces exists in each of the interior feature areas. Each print contains two sets of trenches, either with or without exposure compensation, such that both could be tested in a single print.

3.3.2.1 Ridges

I again used ridges as positive features to determine the types of structures that could be placed in an interior void in a 3D printed part. Five pixels width was chosen because it formed reliably for surface ridges. An example SEM image of two ridges at 1000 ms exposure is shown in Figure 3.2C; the interior ridge 5 layers tall is shown on the left, with the ceiling support in the middle, and the ridge 6 layers tall is on the right. For interior ridges I measured the gap between the top of the ridge and the ceiling of the void area, which gave information about interior Z resolution. Gap distance (excluding any ridges that attached to the ceiling) is plotted for these interior ridges as shown in Figure 3.3C. The 500 ms exposure time resulted in a void region that was taller than the designed 100 μm due to insufficient adhesion between layers. The ceiling support pieces have broken off, resulting in voids taller than the designed size (Appendix A, Tables A10, A13, A16, and A18). For 1000 and 1500 ms, the void height is smaller than designed, likely due to exposure of the top layer of the chamber polymerizing significantly more than to 10 μm of resin, thereby making the first ceiling layer substantially thicker than designed,

resulting in reduced overall chamber height and hence reduced gap size. This is consistent with our previous work in which we analyzed the layer exposure profile as a function of z[17]. The height of the void area was about 70-75 μm instead of 100 μm and thus any ridges designed to be >7 layers tall were attached to the ceiling. For the ridges that were not attached, however, there was a linear relationship between the designed and measured gap distance. From this data, gaps between the feature and ceiling area as small as 7 μm can be produced with either 1000 or 1500 ms exposures. As long as the print receives sufficient light exposure (>500 ms for this formulation), the gap height between features and ridges is independent of the exposure time for 1000 and 1500 ms exposures, as seen in Figure 3.3C.

3.3.2.2 Trenches

For the interior trenches, a similar approach to the exterior trenches was used. The widths of printed trenches were measured with SEM imaging, and an example image is shown in Figure 3.2D for 1000 ms exposure (without compensation) of trenches that were designed to be 5 and 6 pixels (38 and 46 μm) wide. In this image the trench 6 pixels wide is on the left, and the trench 5 pixels wide is on the right, with the ceiling support pillar in the middle. The measured width was compared to the designed width in Figure 3.3D, including only those trenches that reached >90% of full depth. The 500 ms trenches (both with and without compensation) turn out wider than the 1500 ms trenches, indicating that lower exposure times work better for forming wider trenches. Similar to the effect observed with the exterior trenches, the use of a compensation pattern leads to trenches smaller than they would have otherwise printed, as the compensated trenches are all narrower than the uncompensated ones. Similar to the exterior trenches, the smallest trenches that successfully formed were about 20 μm wide, though they were printed with different

exposure times: 5 pixels wide for 1000 ms with compensation (21 µm), 6 pixels wide for 1500 ms without compensation (21 µm), and 7 pixels wide for 1500 ms with compensation (18 µm). This again demonstrates the concept that there are several different ways to obtain a minimum feature size if the right exposure conditions are determined, especially when there is full control over the exposure properties.

3.3.2.3 Pillars

A final type of feature is a cylindrical pillar in the interior of a void area. Example SEM images were taken of pillars, and an example can be seen in Figure 3.2E showing 1500 ms exposure pillars that are 5-7 pixels wide (38-53 µm). Figure 3.3E shows a plot comparing the designed pillar diameter and the measured diameter, including only those pillars which were fully formed. From this graph, it can be seen that the pillars all printed narrower than their designed width and followed the trend that longer exposure times led to wider pillars. The smallest pillars that were successfully printed were about 16 µm in diameter, printed with 1000 ms exposure for a 5 pixel designed width. The dependence of pillar diameter on light exposure is another example of how control over dosing parameters is essential to achieve desired feature dimensions during SLA 3D printing.

3.3.3 Trapping Devices

To demonstrate the utility of tight control of both positive and negative interior features I created trapping devices to catch particles as they flow through a channel, as a first step toward trapping of cells. The beads selected were 25 µm in diameter, approximately the same size as the smallest trench that was successfully printed. Because 3D printing designs can be easily edited to

46

optimize configurations and print parameters, I attempted a number of different trap placements

(see Figure 3.1D insets) to determine the best trapping efficiency. Figure 3.4 shows images of

channels after trapping experiments were carried out. I found that traps exclusively in the center

of the channel (Figure 3.4A) did not trap as efficiently as traps along the sides (Figure 3.4B)

which in turn were not as efficient as traps that alternate between the channel sides and center

(Figure 3.4C). This was largely due to the flow of the beads around (instead of through) the

traps. Additionally, I found that traps that were 3 layers (~50% of channel height) tall did not

trap as efficiently as traps that were the full height of the channel; when the traps are shorter

many beads simply pass over the traps.
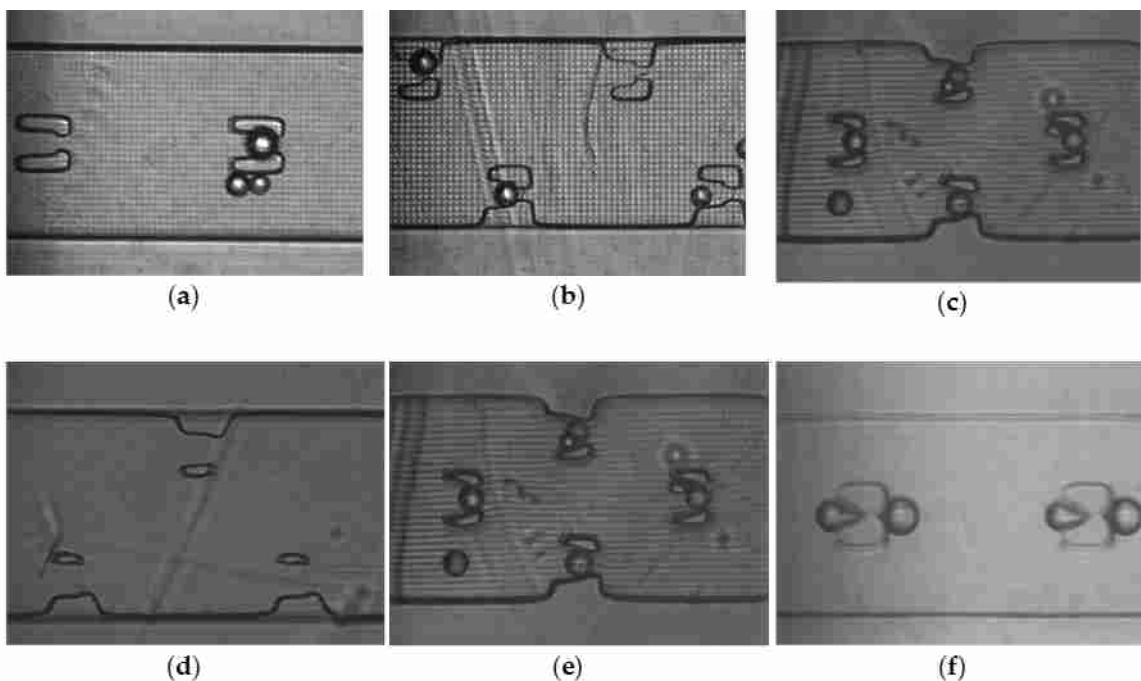
Figure 3.4 CCD images showing the effect of trap placement and different exposure times on trap shape. (**a**) Channel with traps exclusively in the center. (**b**) Channel with traps staggered along the sides. (**c**) Channel with traps staggered along the sides and in the middle of the channel. (**d**) Prints exposed 500 ms showing underformed traps with no bead capture. (**e**) Prints exposed for 750 ms with beads trapped well. (**f**) Prints exposed at 1000 ms showing overexposed traps. Bubbles are stuck at the front and back of the traps hindering bead capture.

Finally, it is critical to have traps that have the correct dimensions. The degree of trap openness could be controlled through the exposure time used for the print. If the exposure time was too short (<600 ms), the traps would be underformed and the beads would pass through the trap without getting caught. Conversely, if the exposure time was too long (>1000 ms) the traps would end up overexposed and there would be no flow through the traps, which resulted in no beads being trapped and often small bubbles that stuck instead. The exposure time of ~750 ms was nearly ideal for forming traps that worked well for beads. Figure 3.4 shows this effect, with underexposed in (d), optimal exposure in (e), and overexposed in (f).

In this chapter I have characterized the 3D printing of sub-100 μm external and internal positive and negative resolution features. I have shown the importance of controlling light dosage, as well as the benefits of multiple different exposure patterns within one layer of a print. Finally, I created a particle trapping device and leveraged the rapid iterative design capabilities of 3D printing to improve trap placement and efficiency.

These developments demonstrate the need for careful control of dosing parameters in making complex 3D printed microfluidic devices. More customization of printer control, resin development, and higher resolution projectors should lead to smaller, more intricate 3D printed microfluidic systems. Improved microfluidics of this type could provide even smaller traps, potentially allowing their use in cell capture or isolation experiments.

3.4   References

1.   Au, A. K., Huynh, W., Horowitz, L. F., Folch, A. 3D-printed microfluidics. *Angew. Chem. Int. Ed*. **2016**, 55, 3862-81.

2.   Shallan, A. I., Smejkal, P., Corban, M., Guijt, R. M., Breadmore M. C. Cost effective 3D printing of visible transparent microchips within minutes. *Anal. Chem*. **2014**, 86, 3124-30.

3.   Plevniak, K., Campbell, M., Myers, T., Hodges, A., He, M. 3D Printed Auto-Mixing chip enables rapid smartphone analysis of anemia. *Biomicrofluidics.* **2016**, 10, 054113-1-11.

4.   Brooks, J. C., Fort, K. I., Holder, D. H., Holtan, M. D., Easley, C. J. Macro to micro interfacing to microfluidic channels using 3d printed templates: application to time resolved secretion sampling of endocrine tissue. *Analyst.* **2016**, 141, 5714-21.

5.   Lee, W., Kwon, D., Choi, W., Jung, G. Y., Au, A. K., Folch, A., Jeon, S. 3D-printed microfluidic device for the detection of pathogenic bacteria using size-based separation in helical channel with trapezoid cross-section. *Scientific Reports.* **2015**, 5, 7717-1-6.

6.   Takenaga, S., Schneider, B., Erbay, E., Biselli, M., Schnitzler, T., Schöning, M. J., Wagner, T. Fabrication of biocompatible lab-on-chip devices for biomedical applications by means of a 3D-printing process. *Phys Status solidi A.* **2015**, 212, 1347-52.

7.   Urrios, A., Parra-Cabrera, C., Bhattacharjee, N., Gonzalez-Suarez, A. M., Rigat-Brugarolas, L. G., Nallapatti, U., Samitier, J., DeForest, C. A., Posas, F., Carcia-Cordero, J. L., Folch, A. 3D printing of transparent bio-microfluidic devices in PEGDA. *Lab Chip.* **2016**, 16, 2287-94.

8.   Macdonald, N. P., Cabot, J. M., Smejkal, P., Guijt, R. M., Paull, B., Breadmore, M. C. Comparing microfluidic performance of three-dimensional (3D) printing platforms. *Anal. Chem*. **2017**, 89, 3858-66.

9.   Sochol, R. D., Sweet, E., Glick, C. C., Venkatesh, S., Avetisyan, A., Ekman, K. G., Raulinaitis, A., Tsai, A., Wienkers, A., Korner, K., Hanson, K., Long, A., Hightower, B. J.,

Slatton, G., Burnett, D. C., Massey, T. L., Iwai, K., Lee, L. P., Pister, K. S. J., Lin, L. 3D printed microfluidic circuitry via multijet based additive manufacturing. *Lab Chip.* **2016**, 16, 668-78.

10.   Lee, K. G., Park, K. J., Seok, S., Shin, S., Kim, D. H., Park, J. Y., Heo, Y. S., Lee, S. J., Lee, T. J. 3D printed modules for integrated microfluidic devices. *RSC Adv*. **2014**, 4, 32876-80.

11.   Lee, J. M., Zhang, M., Yeong, W. Y. Characterization and evaluation of 3D printed microfluidic chip for cell processing. *Microfluid. Nanofluid*. **2016**, 20, 1-15.

12.   He, Y., Wu, Y., Fu, J., Gao, Q., Qiu, J. Developments of 3D printing Microfluidics and Applications in Chemistry and Biology: A Review. *Electroanalysis.* **2016**, 28, 1-22.

13.   Yazdi, A. A., Popma, A., Wong, W., Nguyen, T., Pan, Y., Xu, J. 3D Printing: an emerging tool for novel microfluidics and lab-on-a-chip applications. *Microfluid. Nanofluid*. **2016**, 20, 1-18.

14.   Chen, C., Mehl, B. T., Munshi, A. S., Townsend, A. D., Spence, D. M., Martin, R. S. 3D-printed microfluidic devices: fabrication, advantages and limitations-a mini review. *Anal. Methods*. **2016**, 8, 6005-12.

15.   Waheed, S., Cabot, J. M., Macdonald, N. P., Lewis, T., Guijt, R. M., Paull, B., Breadmore, M. C. 3D printed microfluidic devices: enablers and barriers. *Lab Chip*. **2016**, 16, 1993-2013.

16.   Beauchamp, M. J., Nordin, G. P., Woolley, A. T. Moving from millifluidic to truly microfluidic sub-100 μm cross-section 3D printed devices. *Anal. Bioanal. Chem.* **2017**, 409, 4311-18.

17.   Gong, H., Beauchamp, M. J., Perry, S., Woolley, A. T., Nordin, G. P. Optical approach to resin formulation for 3D printed microfluidics. *RSC Adv*. **2015**, 5, 106621-32.

18.   Gong, H., Bickham, B. P., Woolley, A. T., Nordin, G. P. Custom 3D printer and resin for 18 μm x 20 μm microfluidic flow channels. *Lab Chip*. **2017**, 17, 2899-909.

19.   Gong, H., Woolley, A. T., Nordin, G. P. 3D printed high density, reversible, chip-to-chip microfluidic interconnects. *Lab Chip*. **2018**, 4, 639-47.

4. 3D PRINTED MICROFLUIDIC DEVICES FOR MICROCHIP ELECTROPHORESIS OF PRETERM BIRTH BIOMARKERS[*]

4.1 Introduction

Preterm birth (PTB) is defined as birth before the 37th week of pregnancy and is the leading complication of pregnancy worldwide, affecting about 1 in 10 pregnancies.[1] Sadly, about 1 million infants worldwide die each year from complications from PTB.[2] Additionally, many of the survivors suffer complications from incomplete development including vision, hearing, neurological, respiratory, and cardiac challenges.[3,4] A key strategy in decreasing PTBs and their associated complications would be to develop a widely available diagnostic tool for PTB risk, which could also facilitate studies of the underlying causes of and treatment options for patients at high risk for a PTB. Esplin et al.[5] identified three peptides, which when combined with six previously identified PTB biomarkers,[6-10] predict preterm birth risk from maternal serum at 28 weeks of gestational age with 87% selectivity and 81% specificity. Identifying these biomarkers required a variety of sample preparation techniques prior to LCMS analysis for small peptides vs. proteins,[5] which complicates large scale screening.[11] Other types of analysis such as sandwich or competitive immunoassays like ELISA are well developed but suffer from difficulties with sensitivity and multiplexing due to the interference of multiple analytes being detected simultaneously.[12] An ideal PTB risk diagnosis platform would be inexpensive, robust, and capable of both point of care diagnosis and multiplex detection.

---

[*] Portions of this chapter are reprinted with permission from Beauchamp, M. J., Nielsen, A. V., Gong, H., Nordin, G. P., Woolley, A. T. 3D printed microfluidic devices for microchip electrophoresis of preterm birth biomarkers. *Anal. Chem.* **2019**, 91, 7418-25. Copyright 2019 American Chemical Society.

Microfluidic devices are well suited to address this need because of their small size, low reagent consumption and waste generation, integration of many processes, and ability to be automated.[13-16] To this end, the Woolley lab has been working toward the development of microfluidic systems to determine PTB risk.[17-19] The focus is on microchip electrophoresis (µCE) for separation of these PTB biomarkers because of its ability to readily handle both proteins and peptides in a single analysis. Indeed, Woolley's group recently demonstrated separation of several fluorescently labeled PTB biomarkers in a conventionally constructed planar microfluidic device.[19]

A limitation of planar 2D microfluidic device fabrication is the slow turnaround times for development and optimization of device layouts. For simple, single-layer planar designs like cross T channels, conventional techniques such as embossing, machining, or injection molding work well for device production. However, complex layouts that contain multiple channels in different levels, and valves or pumps, are far more difficult to reliably produce using planar 2D micromachining due to the alignment and bonding processes required for each individual planar layer.[20] Moreover, there exists a substantial cost and time barrier to creating new designs for optimizing a device layout. Finally, the production of such complex, multilayer microfluidic devices by conventional means requires combinations of a cleanroom environment and caustic chemicals, or highly trained personnel.

As a result, alternative and simpler microfabrication techniques such as 3D printing are especially appealing. Several researchers have made 3D printed devices for analytical applications, such as nitrite[21] or anemia[22] detection, endocrine secretion analysis,[23] saponin analysis,[24] catechol detection,[25] and bacterial sorting.[26] Though these works show the possibility of using 3D printed devices to analyze various chemical and biological samples, fabrication was

limited in the minimum size of channels that could be created. Indeed, commercial 3D printing systems are typically capable of printing interior fluidic features of ~250 μm, but for routine use the features are more often >500 μm.[27,28] Such millifluidic structures are poorly suited for important biological and analytical processes such as single-cell analysis, high-performance separations, or creating models of the circulatory system. Alternatively, two photon polymerization techniques can create micro and nanoscale features, with excellent resolution (~150 nm), but they suffer from long print times (>20 hr) to make devices of suitable size for microfluidics.[29]

Two recent publications show both promise and pitfalls of using 3D printing to make fluidic devices for electrically driven separations. Breadmore et al.[30] created large microfluidic (~500 × 800 μm cross section) devices with multiple embedded materials for filtration and isotachophoresis of ampicillin. Although these devices show promise in working with multiple materials and integrating steps in one chip, the detection limit (2 ppm) is too high for many bioanalyses, and the ability to multiplex medically relevant analytes has yet to be demonstrated. Walczak et al.[31] 3D printed ~400 μm diameter microchannels which they filled with gel to electrophoretically analyze a fluorescently labeled DNA ladder. However, the channel fabrication suffered from multihour clearing of support materials. Additionally, as a result of the large channel diameters, even the application of moderate electric fields (200 V/cm) required active cooling of the entire device, and performance was considerably inferior to previously reported microchip DNA separations.

In chapter 2, I discussed the 3D printing of truly microfluidic features using a custom resin formulation and stereolithographic (SLA) 3D printer[32,33] that made channels as small as 18 × 20 μm.[32] The Woolley and Nordin groups have demonstrated the use of these 3D printed

devices for the creation of microfluidic valves, pumps, chip-to-chip interconnects, and PTB biomarker immunoaffinity capture devices.[34,35] Here I present the first demonstration of 3D printed devices with ~50 µm channels that are suitable for microchip electrophoresis separation of several fluorescently labeled PTB biomarkers. Device layout, running buffer, and applied voltages were optimized, and figures of merit were determined for separations. Additionally, limits of detection for the PTB biomarkers were evaluated. This chapter demonstrates the ability to create SLA 3D printed microfluidic devices for high-performance separation of medically relevant biomolecules.

4.2   Experimental Section

4.2.1   Material Sources

Polyethylene glycol diacrylate (PEGDA, 258 Da MW), triethoxysilyl propyl methacrylate, hydroxypropyl cellulose (HPC, average MW 300 kDa), 4-(2-hydroxyethyl)-1-piperazineethanesulfonic acid (HEPES), 2-ethanesulfonic acid (MES), N-cyclohexyl-2-aminoethanesulfonic acid (CHES), phenylbis (2,4,6-trimethylbenzoyl)phosphine oxide (Irgacure 819), and dimethyl sulfoxide (DMSO) were purchased from Sigma-Aldrich (Milwaukee, WI). AlexaFluor 532 NHS ester (AF), acetone, and 2-propanol (IPA) were purchased from Fisher Scientific (Salt Lake City, UT). Glycine (G), ferritin (Fer), sodium phosphate monobasic, hydrochloric acid, and Amicon ultra 0.5 mL centrifuge filters were purchased from Millipore Sigma (Billerica, MA). Boric acid and sodium hydroxide were purchased from Mallinckrodt Specialty Chemicals (St. Louis, MO). Citric acid and sodium bicarbonate monobasic were purchased from Merck (Burlington, MA). Toluene and glass microscope slides (3 × 1 in, 1 mm thick) were purchased from Avantor (Center Valley, PA). Rhodamine B and phenylalanine (F)

were purchased from Spectrum Chemical (New Brunswick, NJ). Peptide 1 (P1) was purchased from Biomatik (Wilmington, DE). Corticotropin releasing factor (CRF) was purchased from GeneScript (Piscataway, NJ). 2-Nitrodiphenylsulfide (NPS) was purchased from TCI America (Portland, OR). Cyclic olefin copolymer (COC) was purchased from Zeon Chemicals (Louisville, KY). Poly(methyl methacrylate) (PMMA) was purchased from Evonik (Parsippany, NJ). Polydimethylsiloxane (PDMS) base and curing agent were purchased from Dow Chemical (Midland, MI). All solutions were prepared in deionized water (18.3 MΩ•cm) filtered by a Barnstead EASYpure UV/UF system (Dubuque, IA).

4.2.2   3D Printing

Glass slides were scored into 1" squares on one face with a laser cutter (Universal Laser Systems, Scottsdale, AZ). The laser cutter settings were 50% power, 10% speed, and 165 pulses per inch. The scored slides were washed with acetone and then IPA and dried in air. They were then submerged in a freshly prepared 10% (v/v) solution of triethoxysilyl propyl methacrylate in toluene for 2h. After treatment, the glass slides were washed again with IPA, dried, and broken along the scored marks. They were stored under toluene until use. The 3D printing resin was made from a solution of 2% NPS and 1% Irgacure 819 (w/w) in PEGDA. The resin was sonicated until all components were dissolved and stored in an amber bottle wrapped in foil to protect it from light.

3D printing designs were created in open source CAD software called OpenSCAD (openscad.org). A schematic of the design used in this work can be seen in Figure 4.1A, showing the sample and buffer reservoirs in purple and channels in green. The overall device dimensions are $12 \times 20 \times 1.8$ mm^3 (L × W × H); 12 mm × 20 mm is the approximate X-Y build area of the

printer. The reservoir radius is 1.4 mm, and channels are designed to be 38 μm wide and 50 μm tall.
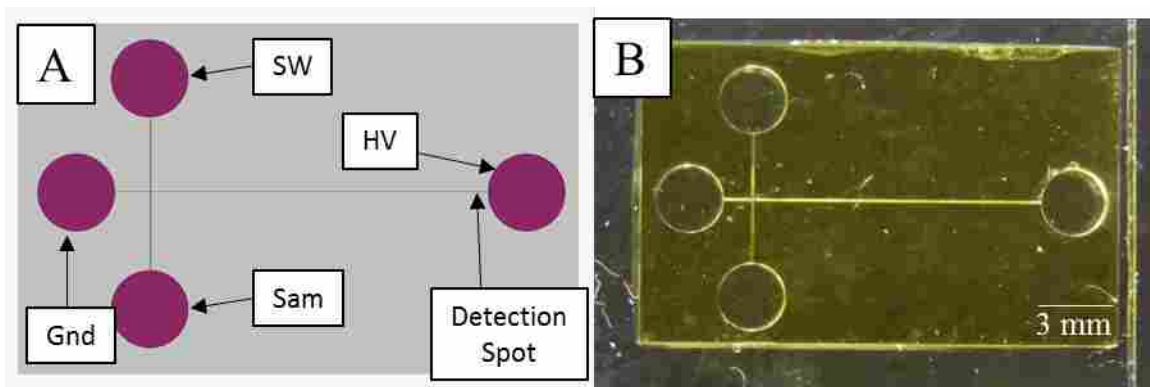
Figure 4.1 T-shaped separation device. (A) OpenSCAD design with channels shown in green and reservoirs in purple. The sample, ground, sample waste and high voltage reservoirs are abbreviated Sam, Gnd, SW, and HV, respectively. The detection point is also indicated. (B) Device photograph.

The SLA 3D printer used in this work is described in ref 32 and chapters 2-3. This 3D printer has a polymerization source that operates at 385 nm, a 7.6 μm pixel size in the image plane and an irradiance of 21 mW•cm^{-2}. The layer thickness for devices is 10 μm, and the normal exposure time for each layer is 600 ms. To ensure attachment of a print to the glass slide, the first four layers are overexposed for 20, 10, 5, and 1 s. After the printing process is complete, the unpolymerized material is flushed out of the print in 30 s using IPA and vacuum. Postprint the device is cured with a 430 nm LED (ThorLabs, Newton NJ) at 11 mW/cm^2 for at least 20 min after liquid resin removal.

An edge underexposure technique is used obtain channels with a more square-like geometry, similar to the technique previously used in our group.[32,36] Edge underexposure uses our ability to project multiple images per layer to over or underexpose pixels at channel edges to optimize feature sizes. Channels are designed to be 5 pixels wide, and the printer underexposes

the two pixels adjacent to each side of the channel. Using this technique, the bulk of the print receives a 600 ms projector exposure in a layer, whereas the two pixels at the channel edge only receive a 400 ms exposure. This reduced exposure helps to limit light scattering into the channels and to optimize the channel shape.

For device transmittance properties, a 2 mm thick piece of resin with 2% NPS was polymerized using our standard device fabrication conditions. The absorption spectrum was measured using an Ocean Optics QE65000 spectrometer (Largo, FL) collected by a 100 μm core optical fiber illuminated by a broadband XCITE-120Q source (Lumen Dynamics, Ontario) between 200 and 1000 nm. The percent transmittance was calculated from three replicate measurements.

To prepare devices for SEM imaging, they were removed from the glass slide and cut using a razor blade. The pieces were fixed to conductive tape and sputter coated with 80:20 Au:Pd. SEM images of channels were taken using an ESEM XL30 FEI (Thermo Fisher, Fairlawn, NJ) using high-vacuum mode with a beam voltage of 10 kV. Channel sizes were measured with ImageJ (NIH, Bethesda, MD) for five different devices. Further characterization of the resolution of the printer and repeatability can be found in chapter 3.

4.2.3   Separations

All samples were dissolved in 10 mM sodium bicarbonate (pH 9.5), and labeling was performed overnight at 37 °C. AF was dissolved in DMSO, with the total DMSO content for labeling kept at or below 10%. The molar labeling ratio for G, F, P1, and CRF was 10:1 sample:dye to minimize the amount of extraneous dye peaks; samples were not filtered due to relatively low analyte molecular weights. Fer was labeled in a 30:1 dye:sample molar ratio.

Excess dye from Fer labeling was removed using a 50 kDa centrifuge filter (4 times, 14,000 rpm, 15 min). The rinsing buffer for Fer filtering was the labeling buffer, 10 mM sodium bicarbonate, pH 9.5. Working solutions of all samples were prepared in 5 mM HEPES (pH 8). Much faster on-chip labeling of proteins and peptides can be accomplished in <30 min in an integrated device.[17] A list of PTB biomarkers analyzed is given in Table 4.1.

Table 4.1 List of PTB biomarkers.[5,17-19]

Biomarker	Abbreviation	Molecular Weight (kDa)	PTB Risk Concentration (nM)
Peptide 1: QLGLPGPPDVPDHAAY HPF	P1	2.0	*
Corticotropin releasing factor	CRF	2.7	0.075
Ferritin	Fer	470	0.040

*PTB risk concentration not known.

For Ohm's law experiments a device was filled with running buffer (50 mM HEPES pH 8 with 1.0% HPC). The Sam, SW, and Gnd reservoirs were kept at 0 V and voltage was applied at the HV reservoir. The current and voltage were measured using a high voltage power supply (Stanford Research Systems, Sunnyvale, CA). The experiment was conducted on three different devices, with three replicates per device.

For μCE, the device was filled with 50 mM HEPES, pH 8, with 1.0% HPC (running buffer). All buffers were prepared with the stated concentration of buffering compound and titrated to the stated pH using 0.1 M NaOH or HCl. Pinched injection[19,37] at +200 V was used;

plug shape was confirmed by fluorescence imaging of the channel intersection. During separation, the pullback voltage was +200 V, and the separation voltage was +400 V.

The LIF detection system had a 532 nm laser (Laserglow Technologies, Toronto, ON) that passed through a dichroic mirror (Semrock, Rochester, NY) and entered an Axio Observer.A1 inverted microscope (Zeiss, Jena, Germany) fitted with a Chroma ET-532 nm laser band and long pass filter set (Rockingham, VT). A 20× objective was used to focus the excitation source within the channel and collect fluorescent photons. Voltages were controlled using two high-voltage power supplies and a custom voltage switching box, which was connected to the separation device using platinum electrodes. Power exiting the laser was 4.0 mW. The fluorescence emission was collected with a Hamamatsu PMT (Bridgewater, NJ) with a Stanford Research Systems SR-560 preamplifier (Sunnyvale, CA). The analog PMT voltage signal was digitized using a NI USB-6212 analog-to-digital converter (National Instruments; Austin, TX) and recorded at 20 Hz using LabVIEW software (National Instruments). The signal was measured 0.5 mm from the end of the separation channel, giving an effective separation distance (injection channel to detection point) of 11.6 mm.

PDMS was prepared by mixing base and curing agent in a 10:1 ratio and degassing for 30 min. The mixture was placed on a glass slide and cured at 110°C for 45 minutes. To measure the autofluorescence of various device materials (PMMA, COC, PDMS, and 3D prints) a small block of material was placed within the focused laser, and the resulting fluorescent signal at the PMT was measured for 1 min at five different points.

For electroosmotic flow (EOF) measurements (each conducted in duplicate), 20 nM rhodamine B was injected in the same manner as the samples. The time to saturate the signal detected at the channel intersection (within 5% of its maximum) was measured. EOF was

calculated from the injection time, applied voltage (+200 V), distance to the detection spot, and total length of the injection channel. Finally, EOF was corrected for diffusion by allowing rhodamine B to diffuse without an applied voltage.

4.3 Results and Discussion

A photograph of a finished 3D printed device can be seen in Figure 4.1B. The print has a slight yellow color due to the presence of both the UV absorber (NPS) and photoinitiator (Irgacure 819). Channels can be seen running between the Sam and SW reservoirs and Gnd and HV reservoirs, which intersect in a T-shaped design.

A comparison between a channel without edge underexposure and one with channel edge underexposure as used in this work can be seen in Figure 4.2. The channel with standard exposure (Figure 4.2A) measures 27.1 ± 1.1 μm wide and 50.6 ± 1.4 μm tall (n = 5). The channel has nearly the same height as designed but is 12 μm narrower. Figure 4.2B shows an SEM image of a device with a reduced edge exposure as used in this work. The channels of this device measure 37.2 ± 0.5 μm wide and 49.3 ± 0.8 μm tall (n = 5). This channel size was selected because these devices had high yields with routine processing. The channel height and width are almost exactly as designed in the CAD file. Importantly, understanding the effects of exposure parameters on channel shape and size, plus the ability to control all aspects of printing including layer thickness (down to 1 μm), enable successful device fabrication.
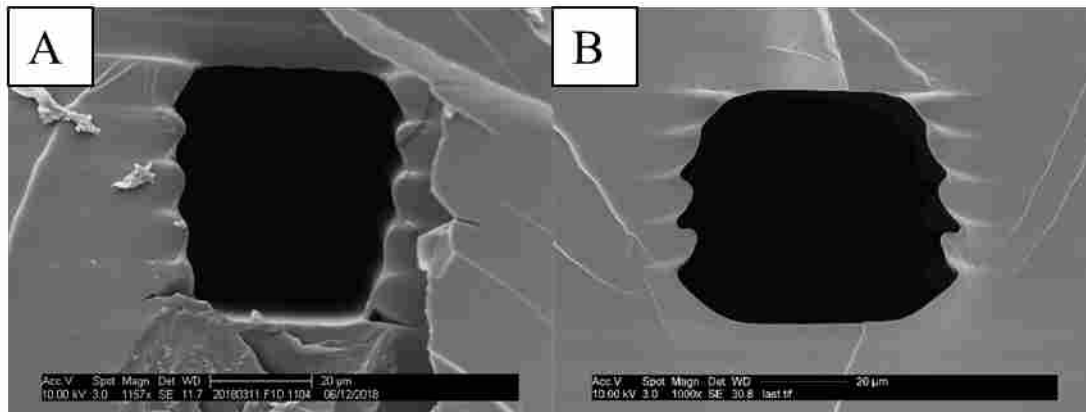
Figure 4.2 SEM images of channel cross sections. (A) Channels with standard (600 ms) exposure measure 27.1 ± 1.1 µm wide and 50.6 ± 1.4 µm tall. (B) Reduced edge exposure (400 ms at channel edge, 600 ms in bulk) channels measure 37.2 ± 0.5 µm wide and 49.3 ± 0.8 µm tall.

Initial experiments focused on determining optimal separation conditions and device layout for peak resolution and efficiency. Several device layout parameters such as reservoir size, relative lengths of separation and injection channels, and reservoir spacing were tested to determine their effects on separation results. From this analysis, I determined that the device configuration that yielded the most reproducible results (Figure 4.1) had reservoirs 2.7 mm in diameter, a separation channel length of 13 mm, and the channel connecting the sample and sample waste reservoirs intersecting the separation channel 2 mm from the ground reservoir. I believe this design worked well for two main reasons. First, the larger reservoirs minimize the effects of gravity-induced flow due to height differences of liquid in the reservoirs. Rapid capillary flow is observed in these devices even with minor liquid height differences, and larger reservoirs limit gravity induced flow, such that fluid motion is only dictated by the voltage configuration. Second, the device layout in Figure 4.1 makes the separation channel length near the maximum length feasible for a straight channel with the 3D print size, allowing the best peak resolution possible. A serpentine geometry could be used to increase channel length, but the tapered turns needed to limit band broadening[38] create complications. The minimum channel

width we can print is ~20 μm wide, which would require untapered sections of channel to be ~100 μm wide, likely degrading separation performance.

Nordin's group previously characterized the absorption of this resin;[32] the transmittance for a 500 μm thick piece of material can be seen in Figure 4.3. This matches the 500 μm thickness of material between the channel and the bottom of a device. At the maximum excitation and emission wavelengths of AF532 (532 and 554 nm) the transmittances are 99.84 and 99.87%, respectively, indicating very little absorbance of the excitation and emission in these devices.
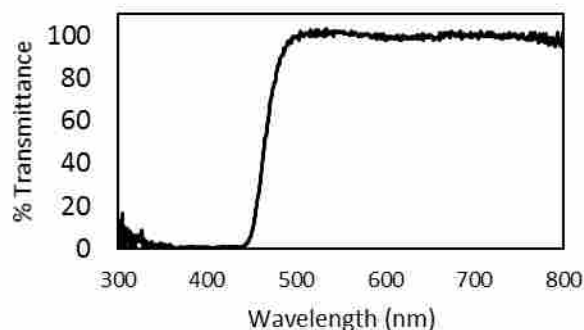
Figure 4.3 Transmittance spectrum of 500 μm thick 3D printed part containing 2% NPS.

I also characterized the autofluorescence of the 3D printed material as well as three other common microfluidic materials: PMMA, COC, and PDMS. The fluorescence from the focused laser in the bulk material collected at the PMT is given in Figure 4.4. My 3D printed devices have slightly higher fluorescence than either COC or PDMS (0.3 vs. 0.1-0.2) but lower fluorescence than PMMA (0.3 vs. 0.6). Hence, the 3D printed material has acceptable background for use in LIF detection compared to other commonly used polymer device materials.
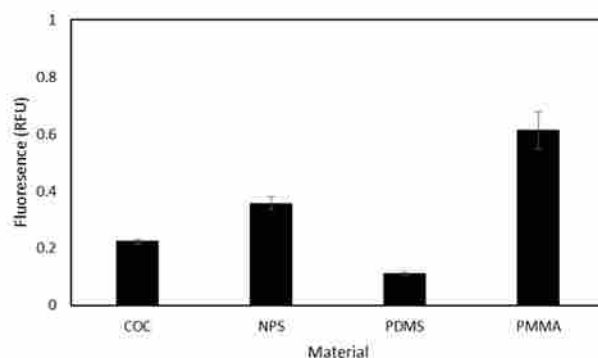
Figure 4.4 Autofluoresence of various microfluidic device materials. Signal was collected for 1 min and was averaged for 5 different spots of the device in the bulk material. The device material (NPS) shows more fluorescence than either COC or PDMS, but less than PMMA. Error bars represent the standard deviation of 5 measurements.

With the device design optimized, I next sought to determine the best separation

conditions regarding buffer identity, concentration, and the voltages applied. Several different

buffer compositions were examined, including sodium citrate (pH 5), MES (pH 6), sodium

phosphate (pH 7), HEPES (pH 8), sodium borate (pH 8), CHES (pH 9), and sodium bicarbonate

(pH 9.5). I found that ~10 mM concentrations of polyprotic buffers (citrate, phosphate, and

bicarbonate) produced erratic currents in devices and bubbles from electrolysis of the running

buffer in reservoirs and channels even at fields <100 V/cm. I do not believe this is an ionic

strength issue, because the ionic strength in the polyprotic buffers was similar to that in buffers

that did not show bubble problems (e.g., 0.011 for citric acid, pH 5, 0.013 for HEPES, pH 8). For

all concentrations of MES buffer (10, 25, 50, and 100 mM), samples had issues with consistent

injection times and amounts likely due to how close the buffer pH (6) was to the pIs of the amino

acids (6.1 for G and 5.5 for F). To determine the optimal buffer among the remaining candidates

(HEPES, borate, and CHES), the resolution between AF-labeled G and F was measured at a

variety of buffer concentrations between 10 and 100 mM. From this analysis, the optimal buffer

concentration was 50 mM; however, I occasionally had issues performing a reproducible injection with all buffers. I found that adding 1.0% HPC to the running buffer helped stabilize EOF, resulting in a 100% success rate for injections and better resolved peaks. In Figure 4.5A, the electropherogram for μCE of amino acids with HPC in the buffer shows better resolution (2.3 vs 1.3) between the G and F peaks than the separation without HPC (Figure 4.6). HPC may play multiple roles in improving resolution between G and F by improving the peak efficiency as a dynamic coating that prevents analyte adsorption and by stabilizing/suppressing EOF. Additionally, Table 4.2 reports EOF for these buffers with and without HPC. The buffers without HPC all had less reproducible migration times and EOFs than those with HPC; HEPES was selected as the running buffer, because it had the lowest EOF. This buffer is similar to that used in previous work from Woolley's group (100 mM CHES pH 9 with 0.05% HPC),[19] but in that study, higher molecular weight (~1000 kDa) HPC was used, which was less soluble than the (~100 kDa) used in this work. Also in that prior work,[19] buffer pHs between 7 and 10 were found to be acceptable, including pH 8 HEPES. Thus, the running buffer used for analysis was 50 mM HEPES, pH 8, with 1.0% HPC.
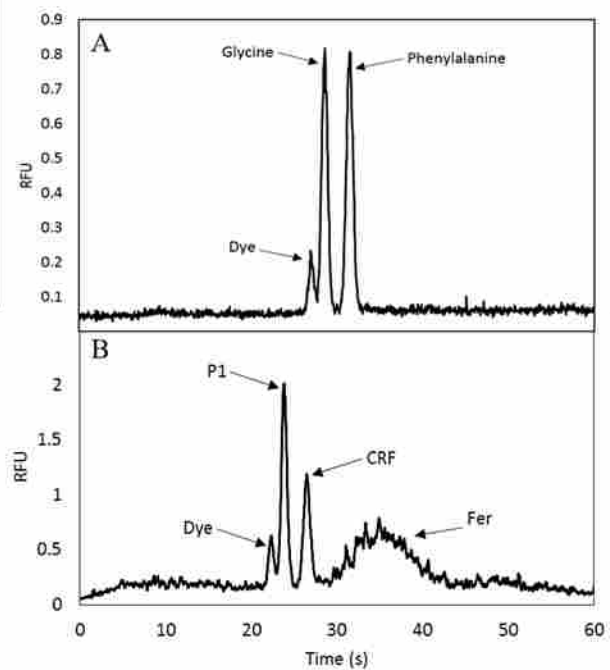
Figure 4.5 Microchip electropherograms in 3D printed microfluidic devices. (A) Amino acids: 50 nM G and F in 50 mM HEPES, pH 8. (B) PTB biomarkers: P1, CRF, and Fer; analyte concentrations are 20, 5, and 5 nM, respectively.
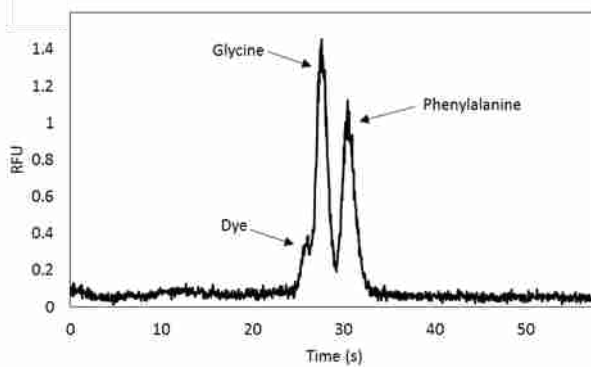
Figure 4.6 Separation of 50 nM G and F in 50 mM HEPES, pH 8, without HPC in the running buffer.

Table 4.2 Measured EOF of 50 mM buffers. Each buffer was measured in duplicate.

Buffer	EOF (cm^2/V·s)	SD
Borate-no HPC, pH 8	0.162	0.050
Borate-1% HPC, pH 8	0.196	0.007
HEPES-no HPC, pH 8	0.128	0.049
HEPES-1% HPC, pH 8	0.134	0.005
CHES-no HPC, pH 9	0.247	0.041
CHES-1% HPC, pH 8	0.172	0.009

I carried out an Ohm's Law analysis of our 3D printed devices. The current vs. voltage results from these experiments can be seen in Figure 4.7. Devices maintained a linear I-V relationship up to ~800 V. The average applied potential where a 5% deviation from linearity occurred (n=9) was 800 ± 100 V (620 ± 80 V/cm). This voltage is almost double what we applied during μCE, indicating that Joule heating was not an issue in μCE runs. Indeed, operational voltages below this limit allowed good resolution and ensured consistency in separation performance. I also did not observe any problems with arcing between the three closer reservoirs under these conditions.
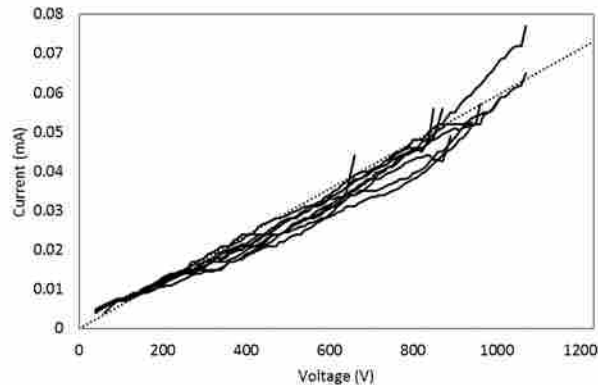
Figure 4.7 Measured current vs. voltage in 37 × 50 μm channels in 3D printed microfluidic devices. Data are shown for 9 trials, up to the voltage where current deviates from linearity. A dotted reference line is included to make the deviations from linearity more readily visible.

With Ohm's Law setting an upper limit for applied voltage, I optimized the voltage configuration for PTB biomarker separations. This involved balancing of a strong, consistent electric field in the channel, without causing too much electrolysis of the running buffer through the course of the run. For injection, up to +225 V (450 V/cm) was applied across the channel connecting Sam and SW, whereas the remaining reservoirs were grounded. For separation, the Gnd reservoir was grounded, up to +225 V was applied to the Sam and SW reservoirs, and up to +500 V (380 V/cm) was applied to the HV reservoir. Applying these voltages did not cause buffer electrolysis during the ~3 min analysis time. This electric field is comparable the 500 V/cm Woolley's group used previously with COC microdevices.[19] During each separation experiment, every injection was confirmed by fluorescence imaging in the microscope, ensuring high signal in the injection intersection before application of the separation voltage. After injection confirmation, the microscope stage was translated so the detection spot was 0.5 mm from the reservoir at the end of the channel. I used an amino acid test mixture for initial characterization of devices. The results of the optimized separation of G and F are shown in Figure 4.5A. The two peaks are well separated, and a small amount of residual dye from labeling

was detected before the G peak. Peak retention times were confirmed by spiking individual analytes into the mixture. The resolution between G and F is 2.3, and the number of theoretical plates is 1600 for G and 1700 for F. This separation clearly demonstrates the ability of this system to rapidly resolve fluorescently labeled biomolecules in <1 min with good separation performance. Additionally, this separation served as a test for all devices to verify functionality before use with other samples.

I further compared the µCE results in 3D printed microfluidic devices with the initially published µCE of amino acids with LIF detection in four widely used materials: glass,[39] PDMS,[40] PMMA,[41] and COC.[42] Table 4.3 reports the amino acid concentrations analyzed, the separation distances, the electric fields and times for separation, and the number of theoretical plates achieved in the first demonstration of µCE of amino acids in each of these materials. Notably, the 3D printed material had the lowest amino acid concentration separated (50 nM). The 3D print material also worked with comparable electric fields to the other polymer materials but lower fields than those applied in glass. These 3D printed devices had the shortest separation distances and had among the fastest separation times (tied with PMMA and twofold slower than glass but nearly tenfold faster than in PDMS or COC). The 3D prints had lower theoretical plate counts than obtained in the other materials, although the plates per separation distance are higher in the 3D printed device than in the initial PDMS report. These results demonstrate that 3D printed microfluidic devices offer comparable separation performance to that in other polymer materials.

Table 4.3 Comparison of performance in the first paper reporting μCE of amino acids with LIF detection in a given device material.

	Glass	PDMS	PMMA	COC	3D print
conc (μM)	10	10	3	0.1	0.05
d (cm)	11	21	2.0	2.5	1.2
E (V/cm)	1100	180	360	460	380
time (s)	15	280	30	300	30
N	40,000-75,000	23000*	4700-6700	12000	1600-1700
ref.	39	40	41	42	this work

*N not reported, estimated from the data in ref. 40.

Encouraged by these small molecule separations, I further developed conditions for μCE of three PTB biomarkers, P1, CRF, and Fer. These biomolecules were chosen as being representative of the larger panel of PTB biomarkers (smallest, intermediate, and largest compounds). An electropherogram of these three compounds can be seen in Figure 4.5B showing good separation; peak identities were confirmed by spiking. The resolution between the critical pair of peaks of interest (P1 and CRF) is 2.1, and the efficiency for P1 is 3600 plates. It is worth noting that the peak for Fer is broader than the others due to its large size and number of amine groups, which allow for a larger distribution in the number of AF labels attached. In recent work,[19] Woolley's group separated six PTB biomarkers with resolutions ranging from 0.5 to 1.9, indicating that these 3D printed devices offer comparable separations to conventionally fabricated devices. Importantly, this work represents the first successful demonstration of high performance μCE in a 3D printed microfluidic device.

I also characterized the detection limits for the three PTB biomarkers in these devices, as seen in Figure 4.8; all samples were analyzed in triplicate. Figure 4.8A shows the results for P1, which had a limit of detection of 7 nM and an R^2 value of 0.994. Figure 4.8B shows the calibration curve for CRF, which had a limit of detection of 200 pM and an R^2 value of 0.999.

Finally, Figure 4.8C contains the calibration curve for Fer, which has a limit of detection of 4 nM and an R^2 value of 0.996. The Fer sample calibration curve has a nonzero intercept, most likely because of either the greater peak width or small amounts of nonspecific adsorption of this large protein to the channel walls, which is more pronounced at very dilute concentrations. The limits of detection for this analysis are excellent, in the high pM to low nM range, and consistent with previous work involving conventional microfluidic devices, where detection limits for P1, CRF, and ferritin were 3, 90, and 1 nM, respectively.[19] Although these detection limits are still higher than the PTB risk levels for these analytes, Woolley's group has previously demonstrated that detection limits can be lowered through on-chip integration of immunoaffinity or solid-phase extraction with μCE.[17,18]
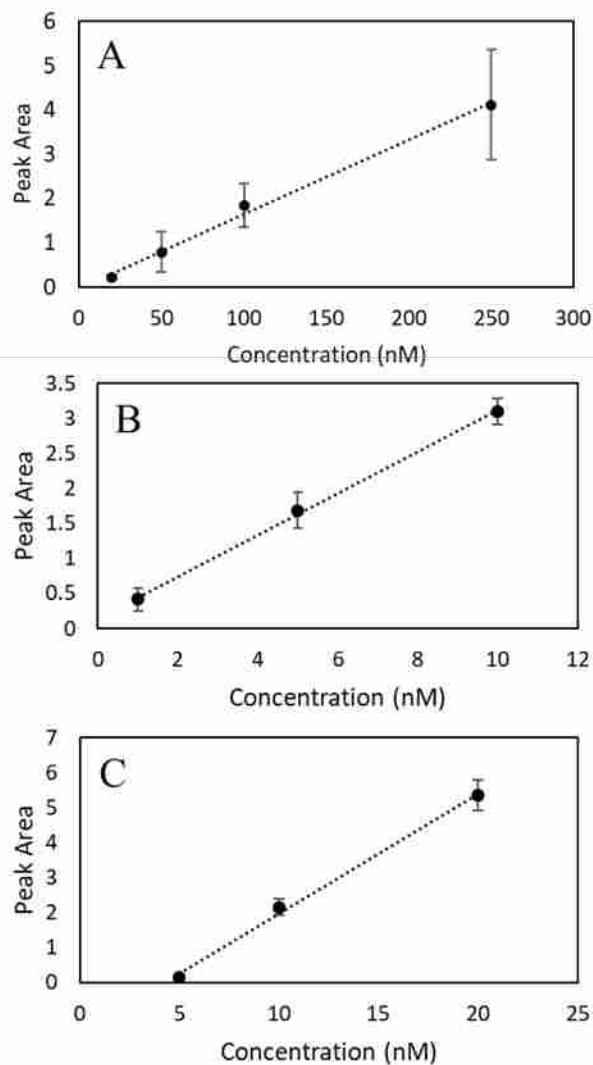
Figure 4.8 Calibration curves for determining detection limits for μCE of PTB biomarkers in 3D printed microfluidic devices. (A) P1; the limit of detection is 7 nM. (B) CRF; the limit of detection is 200 pM. (C) Fer; the limit of detection is 4 nM.

I note that further optimization should be helpful in facilitating device fabrication and use. Initially, approximately 75% of devices have all features correctly formed after 3D printing, and improvements in printer calibration and print design with more recent devices increased printing success to ~90%. The most common print failure mechanisms are device delamination from the glass slide caused by misalignment during printer calibration or bubbles trapped in the

resin during the printing process. Of the correctly printed devices, ~50% were successfully used for μCE experiments in the operation verification procedure separating amino acids. Recent experiments suggest that the device operation success rate could also be increased to ~80% through proper identification of defective devices and improved channel filling and cleaning. Common device operation failures entail poor sample injection or delamination when voltage is applied. To improve device yield and operational success, improvements are ongoing to the 3D printer calibration technique to provide better projector focus and reduce blur at channel edges. Initial results also show promise for decreasing device defects such as bubbles and particles by filtration and resin tray film treatment.

In this chapter, I have demonstrated SLA 3D printing of microfluidic devices with channels <50 μm for μCE analysis of amino acids and preterm birth risk biomarkers, the first such separation in a 3D printed device. Separation conditions including device layout, running buffer, and applied voltages were optimized using Ohm's Law and EOF analysis and validated using a test mixture. I applied these devices in analyzing medically significant samples, with a resolution of 2.1 and 3600 plates. Limits of detection for the analytes were in the high pM to low nM range, comparable to previous results in conventionally fabricated microfluidic devices. Device yields are good, with excellent prospects for improvement though better 3D printer calibration techniques, resin pretreatment, and printer preparation procedures.

This demonstrates the use of SLA 3D printing to make microfluidic devices for analysis of medically relevant biomarkers. Ongoing studies to evaluate these devices with additional biomarkers as well as improvements in device fabrication and use will further showcase the utility and benefits of this approach. For example, higher resolution printing should allow for serpentine channels with tapered turns to be made to increase channel length. In addition, a key

advantage of 3D printing is the ability to readily combine multiple components and processes in a single device, which can be leveraged in interfacing solid-phase extraction and on-chip sample preparation. The capabilities of this 3D printing system in creating complex 3D microfluidic structures in a scalable manner offers great opportunities for device optimization and fabrication. Finally, the ability to generate 3D printed microfluidic systems and use them to address important analytical problems holds great value for future developments in the field.

4.4   References

1.   World Health Organization; March of Dimes; The Partnership for Maternal, newborn & Child Health; Save the Children. Born too soon: the global action report on preterm birth, WHO, Geneva, **2012**.

2.   Centers for Disease Control and Prevention. Preterm birth in maternal and infant health. CDC. 2018. https://www.cdc.gov/reproductivehealth/maternalinfanthealth/pretermbirth.htm. Accessed July 3, 2018.

3.   Behrman RE, Butler AS. Preterm birth: causes, consequences, and prevention. National Academies Press; Washington DC; **2007**.

4.   Blencowe, H., Cousens, S., Oestergaard, M. Z., Chou, D., Moller, A. B., Narwal, R., Adler, A., Vera Garcia, C., Rohde, S., Say, L., Lawn, J. E. National, regional, and worldwide estimates of preterm birth rates in the year 2010 with time trends since 1990 for selected countries: a systematic analysis and implications. *Lancet*. **2012**, 379, 2162-2172.

5.   Esplin, M. S., Merrell, K., Goldenberg, R., Lai, Y., Iams, J. D., Mercer, B., Spong, C. Y., Miodovnik, M., Simhan, H. N., van Dorsten, R., Dombrowski, M. Proteomic identification of

serum peptides predicting subsequent spontaneous preterm birth. *Am. J. Obstet. Gynecol*. **2011**, 204, 391.e1–8.

6.   Al-Gubory, K. H., Fowler, P. A., Garrel, C. The roles of cellular reactive oxygen species, oxidative stress and antioxidants in pregnancy outcomes. *Int. J. Biochem. Cell Biol*. **2010**, 42, 1634–50.

7.   Buhimschi, I. A., Christner, R., Buhimschi, C. S. Proteomic biomarker analysis of amniotic fluid for identification of intra-amniotic inflammation. *BJOG*. **2005**, 112, 173–81.

8.   Fortunato, S. J., Menon, R. Distinct molecular events suggest different pathways for preterm labor and premature rupture of membranes. *Am. J. Obstet. Gynecol*. **2001**, 184, 1399–406.

9.   Petraglia, F., Imperatore, A., Challis, J. R. G. Neuroendocrine mechanisms in pregnancy and parturition. *Endocr. Rev*. **2010**, 31, 783–816.

10.   Kramer, M. S., Lydon, J., Séguin, L., Goulet, L., Kahn, D. R., McNamara, H., Genest, J., Dassa, C., Chen, M. F., Sharma, S., Meaney, M. J., Thomson, S., Van Uum, S., Koren, G., Dahhou, M., Lamoureux, J., Platt, R. W. Stress pathways to spontaneous preterm birth: the role of stressors, psychological distress, and stress hormones. *Am. J. Epidemiol*. **2009**, 169, 1319-26.

11.   Grebe, S. K. G., Singh, R. J. LC-MS/MS in the clinical laboratory–where to from here?. *Clin. Biochem. Rev*. **2011**, 32, 5–31.

12.   Cross, T. G., Hornshaw, M. P., Can LC and LC-MS ever replace immunoassays? *J. Appl. Bioanal*. **2016**, 2, 108–16.

13.   Nge, P. N., Rogers, C. I., Woolley, A. T. Advances in microfluidic materials, functions, integration, and applications. *Chem Rev*. **2013**, 113, 2550-83.

14.   Pandey, C., Augustine, S., Kumar, S., Nara, S., Srivastava, S., Malhotra, B. Microfluidics based point-of-care diagnostics. *Biotechnol. J.* **2018**, 13, 1700047.

15.   de Campos, R. P. S., Siegel, J. M., Fresta, C. G., Caruso, G., da Silva, J. A. F., Lunte, S. M. Indirect detection of superoxide in RAW 264.7 macrophage cells using microchip electrophoresis coupled to laser-induced fluorescence. *Anal. Bioanal. Chem.* **2015**, 407, 7003-12.

16.   Hu, J., Cui, X., Gong, Y., Xu, X., Gao, B., Wen, T., Lu, T. J., Xu, F. Portable microfluidic and smartphone-based devices for monitoring of cardiovascular diseases at the point of care. *Biotechnol. Adv.* **2016**, 34, 305-20.

17.   Sahore, V., Sonker, M., Nielsen, A. V., Knob, R., Kumar, S., Woolley, A. T. Automated microfluidic devices integrating solid-phase extraction, fluorescent labeling, and microchip electrophoresis for preterm birth biomarker analysis. *Anal. Bioanal. Chem.* **2018**, 410, 933-41.

18.   Sonker, M., Parker, E. K., Nielsen, A. V., Sahore, V., Woolley, A. T. Electrokinetically operated microfluidic devices for integrated immunoaffinity monolith extraction and electrophoretic separation of preterm birth biomarkers. *Analyst.* **2018**, 143, 224-31.

19.   Nielsen, A. V., Nielsen, J. B., Sonker, M., Knob, R., Sahore, V., Woolley, A. T. Microchip electrophoresis separation of a panel of preterm birth biomarkers. *Electrophoresis*, **2018**, 39, 2300-7.

20.   Dziomba, S., Araya-Farias, M., Smadja, C., Taverna, M., Carbonnier, B., Tran, N. T. Solid supports for extraction and preconcentration of proteins and peptides in microfluidic devices: A review. *Anal. Chim. Acta.* **2017**, 955, 1-26.

21.   Shallan, A. I., Smejkal, P., Corban, M., Guijt, R. M., Breadmore M. C. Cost-effective three-dimensional printing of visibly transparent microchips within minutes. *Anal. Chem.* **2014**, 86, 3124-30.

22.   Plevniak, K., Campbell, M., Myers, T., Hodges, A., He M. 3D printed auto-mixing chip enables rapid smartphone diagnosis of anemia. *Biomicrofluidics*. **2016**, 10, 054113-1-11.

23.   Brooks, J. C., Ford, K. I., Holder, D. H., Holtan, M. D., Easley, C. J. Macro-to-micro interfacing to microfluidic channels using 3D-printed templates: application to time-resolved secretion sampling of endocrine tissue. *Analyst*. **2016**, 141, 5714-21.

24.   Anderson, K. B., Lockwood, S. Y., Martin, R. S., Spence, D. M. A 3D printed fluidic device that enables integrated features. *Anal. Chem*. **2013**, 85, 5622-6.

25.   Munshi, A. S., Martin, R. S. Microchip-based electrochemical detection using a 3-D printed wall-jet electrode device. *Analyst*. **2016**, 141, 862-9.

26.   Lee, W., Kwon, D., Choi, W., Jung, G. Y., Au, A. K., Folch, A., Jeon, S. 3D-printed microfluidic device for the detection of pathogenic bacteria using size-based separation in helical channel with trapezoid cross-section. *Sci. Rep*. **2015**, 5, 7717-1-6.

27.   Beauchamp, M. J., Nordin, G. P., Woolley, A. T. Moving from millifluidic to truly microfluidic sub-100-μm cross-section 3D printed devices. *Anal. Bioanal. Chem*. **2017**, 409, 4311-8.

28.   Waheed, S., Cabot, J. M., Macdonald, N. P., Lewis, T., Guijt, R. M., Paull, B., Breadmore, M. C. 3D printed microfluidic devices: enablers and barriers. *Lab Chip*. **2016**, 16, 1993-2013.

29.   Nanoscribe, Photonic Professional Data Sheet, http://www.nanoscribe.de/files/4414/7393/1095/DataSheet_PP_V05_2016_Web.pdf, accessed December 12, 2018.

30.   Li, F., Macdonald, N. P., Guijt, R. M., Breadmore M. C. A 3D printed fluidic device for measuring pharmaceuticals in biological fluids. *Anal. Chem*. **2019**, 91, 1758-63.

31.   Walczak, R., Adamski, K., Kubicki, W., Inkjet 3D printed chip for capillary gel electrophoresis. *Sens. Actuators, B*. **2018**, 261, 474-80.

32.   Gong, H., Bickham, B. P., Woolley, A. T., Nordin, G. P. Custom 3D printer and resin for 18 μm× 20 μm microfluidic flow channels. *Lab Chip*. **2017**, 17, 2899-909.

33.   Gong, H., Beauchamp, M. J., Perry, S., Woolley, A. T., Nordin, G. P. Optical approach to resin formulation for 3D printed microfluidics. *RSC Adv*. **2015**, 5, 106621-32.

34.   Gong, H., Woolley, A. T., Nordin, G. P. 3D printed high density, reversible, chip-to-chip microfluidic interconnects. *Lab Chip*. **2018**, 18, 639-47.

35.   Parker, E. K., Nielsen, A. V., Beauchamp, M. J., Almughamsi, H. M., Nielsen, J. B., Sonker, M., Gong, H., Nordin, G. P., Woolley, A. T. 3D printed microfluidic devices with immunoaffinity monoliths for extraction of preterm birth biomarkers. *Anal. Bioanal. Chem*. **2018**, DOI: https://doi.org/10.1007/s00216-018-1440-9.

36.   Beauchamp, M. J., Gong, H., Woolley, A. T., Nordin, G. P. 3D printed microfluidic features using dose control in X, Y, and Z dimensions. *Micromachines*. **2018**, 9, 326-1-12.

37.   Jacobson, S. C., Hergenröder, R., Koutny, L. B., Warmack, R. J., Ramsey, J. M., Effects of injection schemes and column geometry on the performance of microchip electrophoresis devices. *Anal. Chem*. **1994**, 66, 1107–13.

38.   Paegel, B. M., Hutt, L. D., Simpson, P. C., Mathies, R. A., Turn geometry for minimizing band broadening in microfabricated capillary electrophoresis channels. *Anal. Chem*. **2000**, 72, 3030–7.

39.   Harrison, D. J., Fluri, K., Seiler, K., Fan, Z., Effenhauser, C. S., Manz, A. Micromachining a miniaturized capillary electrophoresis-based chemical analysis system on a chip. *Science*. **1993**, 261, 895-7.

40.   Duffy, D. C., McDonald, J. C., Schueller, O. J. A., Whitesides, G. M. Rapid prototyping of microfluidic systems in poly(dimethylsiloxane) *Anal. Chem*. **1998**, 70, 4974-84.

41.   Kelly, R. T., Woolley, A. T. Thermal bonding of polymeric capillary electrophoresis microdevices in water. *Anal. Chem*. **2003**, 75, 1941-5.

42.   Wang, Q., Zhang, Y., Ding, H., Wu, J., Wang, L., Zhou, L., Pu Q. The use of ethylene glycol solution as the running buffer for highly efficient microchip-based electrophoresis in unmodified cyclic olefin copolymer microchips. *J. Chromatogr. A*. **2018**, 52, 9422-7.

5. UNIQUE CAPABILITES ENABLED BY 3D PRINTED MICROFLUIDIC DEVICES[*]

5.1 Introduction

3D printing holds considerable promise as a potential fabrication technique for microfluidic devices.[1-5] Indeed there has been much interest in recent years to use these devices in a variety of chemical and biological applications including cell scaffolds,[6] droplet generators,[7-8] hydrogel spheroids,[9] UV-Vis cells,[10] and µCE (chapter 4).[11] Many researchers have taken advantage of some of the unique properties of 3D printing by pausing printing to incorporate membranes and clear windows,[12] creating modular designs that can be connected together,[13] and creating fully 3D dimensional architectures.[14] This chapter demonstrates several novel microfluidic devices that leverage advantageous properties of 3D printing and custom resin formulations. These devices were used for a variety of collaborative projects, both within the Woolley group as well as one internationally.

In an effort to develop a microfluidic platform for the immunoaffinity extraction, on-chip concentration and labeling, and separation and quantification of PTB biomarkers Woolley's research group has worked with porous polymer monoliths.[15-19] A monolith is a porous structure that can be used for solid phase extraction (SPE) in sample purification and preconcentration steps in microfluidics. Reverse-phase monoliths are used to retain compounds based on

---

hydrophobic interactions between the stationary phase and the analyte. Immunoaffinity

monoliths have been used for extraction of compounds from buffer and serum based on antigen

recognition of antibodies covalently attached to the surface of the monolith. Both types of

monoliths are typically fabricated on-chip by flowing a prepolymer mix through the channel and

exposing a selectively masked portion to UV light. However, the repeatability, size, and

positioning of monoliths can be problematic, and masking is often done manually, which can be

a cause of error.

From the initial microfluidic devices demonstrated[20-21] until the present day, the vast

majority are planar in nature with only a few layers bonded together to seal the device. This

largely stems from the difficulties that arise from properly aligning and bonding the layers

together. Typical techniques for creating devices involve patterning one substrate with the

desired features and sealing that against another flat substrate to form fluidic structures.[22] The

patterning can be done through hot embossing, casting over a mold, or micromilling.[22] The

patterned and flat substrate may or may not be the same material but, regardless, often just two

pieces are used. In some devices (especially PDMS) three pieces are used comprised of a channel

layer, flat piece, and orthogonal control layer. Due to the elastomeric nature of PDMS and the

orthogonality of the features the flat layer acts as a deflecting membrane for pumps and valves.

In most cases, researchers seek to avoid manually aligning layers together as this process can be

time consuming, expensive, and requires finesse because the features are ~50 μm or smaller.

When it comes to 3D printing, however, this formerly tedious alignment of features is automated

because the device is never moved from the surface on which it is being printed. In fact, 3D

printed devices formed by SLA can be seen as an alignment of hundreds of layers all attached to

each other by a photopolymerization process. In addition, moving to large (several mm)

architectures in the Z dimension, orthogonal to the plane of the channels, is easily accomplished with 3D printing. All of these advantages point to 3D printing as a potentially useful technique to overcome the limitations of making truly 3D microfluidics.

Over the years many different detection techniques have been interfaced to various microfluidic platforms such as mass spectrometry,[23] fluorescence,[24] and electrochemistry.[25] All of these techniques have advantages and disadvantages such as being a destructive technique, requiring a fluorophore, or an oxidizable molecule. A detector developed for use with microfluidic systems first reported in 2001 is known as capacitatively coupled contactless conductivity detection, or C4D.[26] The operating principle behind C4D is that as an analyte passes an electrode with an applied alternating current (AC), the change in the conductivity of the solution induces a change in the applied electric field. When coupled to a reference electrode a phase shift between the applied ACs results in a measurable signal.[27] This technique has several advantages compared to conventional conductimetric techniques. Due to the lack of direct contact between the sample and the electrode the common problems of electrode fouling, bubbles caused by electrolysis, and electrical interference from an applied electric field from electrophoresis are avoided entirely.[28] The main drawback of C4D is the lower sensitivity compared to other electrochemical techniques. Researchers have recently pioneered removable, reusable electrodes for electrochemical detection of NO gas standards and ATP.[29] The advantage of having removable electrodes is that they can be removed and polished for use with several devices and analyses without fouling and cross contamination between chips.

In this chapter I present several unique microfluidic devices enabled through 3D printing. First, the use of a monolith polymerization window (MPW) allows the polymerization of a porous polymer monolith for the immunoaffinity extraction of a PTB biomarker, Fer, from 20%

blood serum. These devices take advantage of the UV absorber in the resin to precisely define the monolith area and size without the need for an external photomask. Second, I describe the printing and testing of microfluidic devices with spiral electrodes for C4D in a T-shaped µCE device (as in chapter 4). This device takes advantage of the 3D nature of the printing process to produce a structure that would be impossible to manually align and bond using conventional layered fabrication techniques. Last, the fabrication of a removable insert interfaced to a T-shaped µCE system is developed. This device builds on recent work from the Nordin group to produce a tight microfluidic seal between two 3D printed parts using direct contact in a clamping apparatus.[30] Both the spiral electrode devices and the electrochemical insert devices were tested using a µCE separation of an amino acid mixture of glycine and phenylalanine and shown to have comparable results to the design without these features.

5.2　Experimental Section

5.2.1　Material Sources

Polyethylene glycol diacrylate (PEGDA, 258 Da MW), Tris hydrochloride, antiferritin, glycidyl methacrylate (GMA), ethylene glycol dimethacrylate (EDMA), 1-dodecanol, 2,2-dimethoxy-2-phenylacetophenone (DMPA), triethoxysilyl propyl methacrylate, hydroxypropyl cellulose (HPC, average MW 300 kDa), 4-(2-hydroxyethyl)-1-piperazineethanesulfonic acid (HEPES), phenylbis (2,4,6-trimethylbenzoyl)phosphine oxide (Irgacure 819), and dimethyl sulfoxide (DMSO) were purchased from Sigma-Aldrich (Milwaukee, WI). AlexaFluor 532 NHS ester (AF), acetone, Tris base, and 2-propanol (IPA) were purchased from Fisher Scientific (Salt Lake City, UT). Glycine (G), sodium phosphate, sodium bicarbonate, sodium carbonate, ferritin (Fer), hydrochloric acid, potassium chloride, and Amicon ultra 0.5 mL centrifuge filters were

purchased from Millipore Sigma (Billerica, MA). Toluene and glass microscope slides (3 × 1 in, 1 mm thick) were purchased from Avantor (Center Valley, PA). Phenylalanine (F) and cyclohexanol were purchased from Spectrum Chemical (New Brunswick, NJ). Sodium hydroxide was purchased from Mallinckrodt Specialty Chemicals (St. Louis, MO). Sodium bicarbonate monobasic was purchased from Merck (Burlington, MA). 2-Nitrodiphenylsulfide (NPS) was purchased from TCI America (Portland, OR). Female human blood serum (off-the-clot, sterile filtered) was purchased from Zen-Bio (Research Triangle Park, NC). All solutions were prepared in deionized water (18.3 MΩ•cm) filtered by a Barnstead EASYpure UV/UF system (Dubuque, IA).

5.2.2 Sample Labeling

Fer was fluorescently labeled by dissolving it in 10 mM sodium bicarbonate pH 10 and mixing this in a 30:1 molar ratio with AF dissolved in DMSO. The solutions were incubated overnight in the dark at room temperature. Afterward, the solutions were filtered four times for 15 min at 14000 RPM using a 30 kDa filter, respectively, to remove excess dye. Dilutions of this sample were prepared using 20 mM phosphate, pH 7. The spiked serum sample was made by adding labeled ferritin to make a 50 nM concentration in human blood serum which had been previously diluted to 20% using 20 mM phosphate, pH 7. F and G were labeled in the same manner as chapter 4, section 4.2.3.

5.2.3 Monolith Preparation and Experimental Conditions

Glass slides were scored into 1" squares on one face with a laser cutter (Universal Laser Systems, Scottsdale, AZ). The laser cutter settings were 50% power, 10% speed, and 165 pulses

per inch. The scored slides were washed with acetone and then IPA and dried in air. They were

then submerged in a freshly prepared 10% (v/v) solution of triethoxysilyl propyl methacrylate in

toluene for 2 h. After treatment, the glass slides were washed again with IPA, dried, and broken

along the scored marks. They were stored under toluene until use. The 3D printing resin was

made from a solution of 2% NPS and 1% Irgacure 819 (w/w) in PEGDA. The resin was

sonicated until all components were dissolved and stored in an amber bottle wrapped in foil to

protect it from light.

3D printing designs were created in open source CAD software called OpenSCAD

(openscad.org). The design for the monolith device is shown in Figure 5.1A and a photograph of

the printed device is shown in Figure 5.1B. The printed part is 1.6 mm tall, 12 mm long, and 19

mm wide. The design contains four discrete devices separated by 500 μm spacers (shown in

blue). Each module has a straight channel (shown in red) that is 5 layers (50 μm) tall, 6 pixels

(45 μm) wide, and 4.9 mm long with a 2.7 mm diameter fluid reservoir at either end (shown in

yellow). A 600 μm wide monolith polymerization window (MPW) shown in green that is six

layers above the channel spans the width of each module.
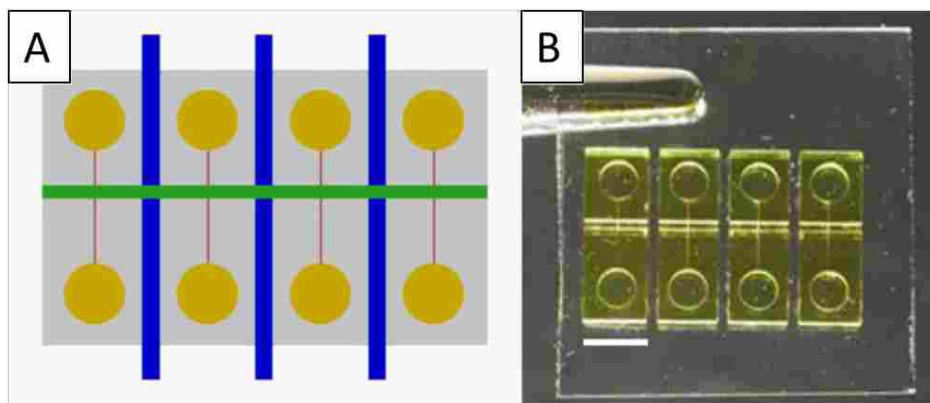
Figure 5.1 3D printing design and photograph of device used for immunoaffinity monoliths. A) OpenSCAD design showing the channels in red, reservoirs in yellow, the MPW in green and the dividers between devices in blue. B) Photograph of device design in A. The scale bar is 4 mm.

The SLA 3D printer used in this work is described in ref 30 and chapters 2-4. This 3D printer has a polymerization source that operates at 385 nm, a 7.6 μm pixel size in the image plane and an irradiance of 21 mW•cm^{-2}. The layer thickness for devices is 10 μm, and the normal exposure time for each layer is 600 ms. To ensure attachment of a print to the glass slide, the first four layers are overexposed for 20, 10, 5, and 1 s. After the printing process is complete, the unpolymerized material is flushed out of the print in 30 s using IPA and vacuum. Postprint the device is cured with a 430 nm LED (ThorLabs, Newton NJ) at 11 mW/cm^2 for at least 20 min after liquid resin removal.

The monolith prepolymer solution was comprised of 24% GMA, 11% EDMA, 10% cyclohexanol, and 55% 1-dodecanol, which was sonicated for 10 min. 1% DMPA was added and the mixture was sonicated for an additional 10 min. This solution was loaded into the channel and the device was placed under a SunRay 600 UV lamp (Uvitron, West Springfield, MA) for 10 min. The unpolymerized material was flushed from the channel by rinsing with IPA for 30 min and the device was stored dry until use. To attach the antibody to the monolith, 5 μL of the antibody solution (2 mg/mL in 20 mM borate buffer pH 8.5) was added to one of the reservoirs and allowed to flow through the channel by capillary action. After the entire channel was filled, both reservoirs were emptied and then refilled with 20 mM borate buffer, pH 8.5, and the antibody solution was left to immobilize overnight at room temperature. Next, the channel was filled with 0.1 M Tris buffer, pH 8.5, which blocks any remaining active sites on the monolith, for 1 hour. Finally, the monoliths were washed with 20 mM phosphate buffer pH 7. For the control experiments, the same procedure was used except for the overnight antibody attachment step.

For the immunoaffinity capture instrumental setup, a laser-induced fluorescence (LIF) detection system used a 532-nm laser (Laserglow Technologies, Toronto, ON) directed into a Zeiss Axio Oberserver.A1 inverted microscope (Jena, Germany) with a Chroma ET-532-nm laser bandpass filter set (Rockingham, VT). Images were taken using a Photometrics coolSNAP HQ2 CCD camera (Tucson, AZ) and a 4× microscope objective. CCD images were taken with exposure times between 100 and 400 ms and analyzed using ImageJ.

For experiments, the channels were first filled with 20 mM phosphate buffer, pH 7, and vacuum was applied to the reservoir further from the monolith for 1 min to equilibrate the channel. Next, the reservoirs were emptied; labeled sample was added to the reservoir nearer to the monolith, and the other reservoir was refilled with fresh phosphate buffer. Vacuum was applied for 1 min to load the sample through the channel. After vacuum was removed, the PTB analyte was allowed to incubate for 10 min with the antibody on the monolith. Then, both reservoirs were washed three times and filled with phosphate buffer, and vacuum was reapplied for 5 min for rinsing. This process was repeated twice until the entire channel was rinsed out (except for any analyte bound to the antibody on the monolith). Rinse efficiency was confirmed by CCD imaging of the monolith. Finally, the rinsing buffer was removed from both reservoirs, elution buffer (50 mM BCB pH 10) was added, and vacuum was reapplied for 2 min. The difference in fluorescent signal at each step of the process is used to determine immunoaffinity capture.

5.2.4 Capacitatively Coupled Contactless Conductivity Detection Devices

The design for the device used for C4D is shown in Figure 5.2. This device is the same as the T-shaped µCE device used in chapter 4 except it has two spiral C4D electrode channels

wrapped around the separation channel about 500 μm from the high voltage reservoir. The

channel dimensions are approximately 38 μm × 50 μm and the channel size of the circular spiral

electrodes is 200 μm in diameter. The distance from the channel to the coil is approximately 150

μm and the radius of spiral is 300 μm. Two reservoirs (1 mm radius) are attached to each coil

(with a small section of channel connecting them). Figure 5.2B shows an end view of the C4D

coils wrapped around the separation channel. The HV reservoir has been removed to make it

easier to see the coils.
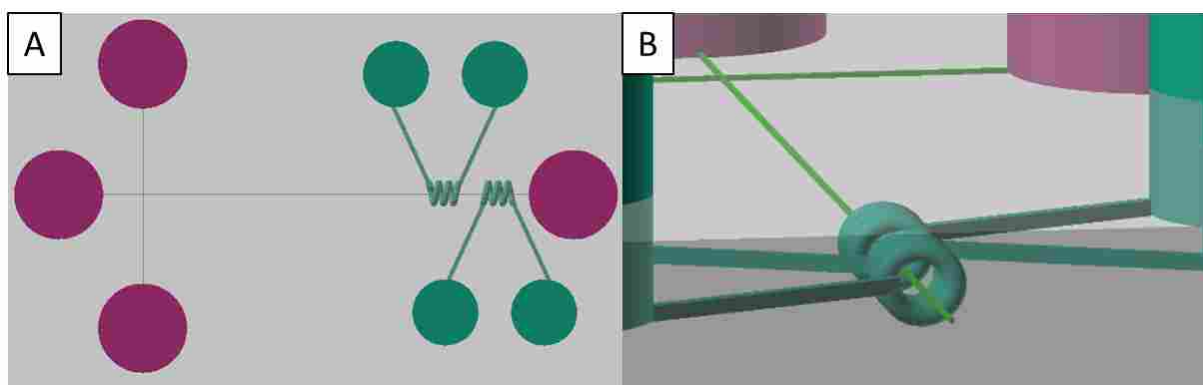
Figure 5.2 OpenSCAD design for C4D spiral electrode device. A) Top-down device view with electrophoresis reservoirs shown in purple, channels in green, and the C4D electrodes with spirals in turquoise. B) Orthogonal device view to show the C4D electrode spirals wrapped around the separation channel. The high voltage reservoir has been removed to make it easier to visualize the electrodes.

Separations of the amino acids G and F were conducted under the same conditions

described in section 4.2.3. For detection, the same laser and microscope setup in the CCD

experiments was used, except a 20× objective was used to focus the excitation source within the

channel and collect fluorescent photons. The emitted fluorescence was directed to a PMT

(Hamamatsu, Bridgewater, NJ) connected to a Stanford Research Systems SR-560 preamplifier

(Sunnyvale, CA). The analog PMT voltage signal was digitized using a NI USB-6212 analog-to-

digital converter (National Instruments; Austin, TX) and recorded at 20 Hz using LabVIEW

software (National Instruments). Fluorescence was recorded between the two spiral C4D electrodes giving an effective separation distance of approximately 11 mm.

To simulate C4D conditions, a 3 M KCl solution was used to fill the spiral electrodes. A function generator (HP 33120a, Agilent Technologies, Santa Clara, CA) was used to supply a 3 V (peak to peak) AC at 350 kHz. The device was inspected for cracks or delamination in the device caused by running under C4D conditions.

5.2.5   Electrochemical Detection Devices with a Removable Insert

Devices for electrochemical detection with a removable insert were made using the two pieces shown in Figure 5.3, which are combined together to form the complete sealed device by placing the post of the device in B into the yellow section of the T-shaped device in A. The T-device is the similar to that used in chapter 4 except there is a hole to insert the electrode insert piece. The two device pieces were held together using an aluminum bracket with 4 screws to secure it in place and adjust the pressure between the pieces. Separations in this device were conducted using the same conditions as in section 5.2.4, except the voltages were reduced to +200 V for injection and +400 V for separation. To test the device, the two pieces were sandwiched together using two aluminum plates with screws in the corners to adjust the tension and O-rings to help prevent breakage
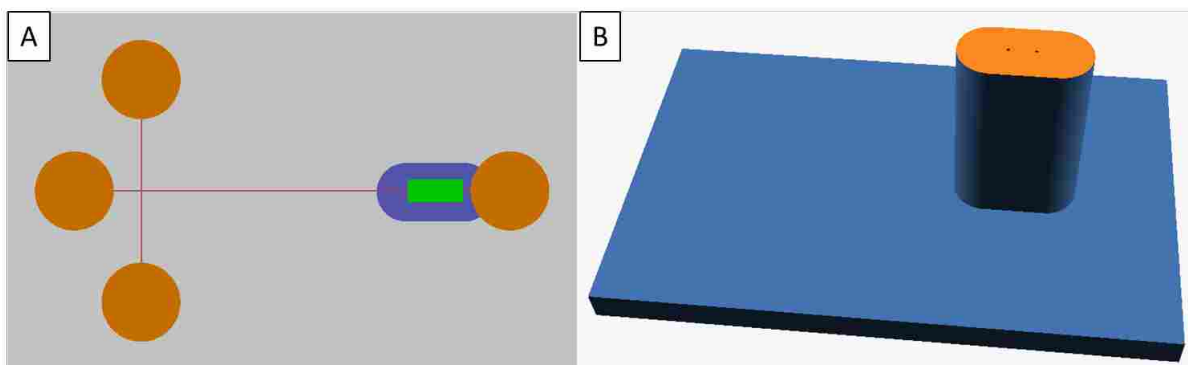
Figure 5.3 Designs of removable electrode insert devices. A) μCE portion of the device with the reservoirs shown in orange, channel shown in red, insert contact area in blue, and approximate electrode detection point in green. B) Electrode insert device. The two holes in the top of the insert are where the electrodes will run through this device.

5.3   Results and Discussion

5.3.1   Immunoaffinity Capture of Ferritin from Serum

The monolith formulation, buffer identity, concentration, rinsing times and antibody selectivity experiments were conducted by a fellow graduate student, Ellen Parker. Detailed below are my specific contributions to this effort.

Initial experiments for developing devices for immunoaffinity extraction of preterm birth biomarkers focused on the use of previous developed channels and resin formulations. One feature of the print was the spacing between the channels. In early designs with higher channel density, I often had issues with cracking through the device causing channels to become damaged by use of the neighboring channels. In order to help prevent this cross-talk between the channels, spacing was placed between individual channels. A second feature of the printed part was the use of large reservoirs (2.7 mm diameter) which lowered the influence of gravity induced flow. A second benefit of using larger diameter reservoirs was that they could be shorter while still holding an adequate volume of samples which reduced the overall print time and stress through the device (thus further reducing cracking).

The final important feature of the immunoaffinity device is called the monolith polymerization window (MPW). The MPW is necessary because the 3D printing resin contains a UV absorber, which does not allow for sufficient penetration of UV light necessary to polymerize monoliths. By creating a trench whose bottom is six layers (60 μm) above the channel top, the material above the channel was thin enough to allow UV light through to polymerize the monolith in this region. In this way, the MPW utilized the inherent UV absorption properties of the resin to give precise and reproducible spatial selectivity over monolith formation. For these experiments, the MPW width (and thus the monolith length) was designed to be 600 μm, but it would be straightforward to design other lengths.

To show the precision and spatial selectivity afforded by the MPW in monolith formation, monoliths were polymerized in 3D printed devices using either a MPW or a chrome-glass mask. In both cases, the monolith was designed to be 600 μm long and was placed 1.2 mm from a reservoir. With the mask, monoliths were formed with a length of 607 ± 25 μm and a spatial precision of ± 65 μm (n = 8). Using the MPW, monoliths were 567 ± 14 μm long with a spatial precision of ± 17 μm (n = 8). Spatial precision for the MPW is limited by the monolith length, rather than variations in the MPW location in the 3D print. These results indicate that the MPW yields better monolith length precision, and considerably improved spatial positioning precision over monolith formation by an external mask. Additionally, the MPW is easier to place than an external mask since the alignment is integrated into the design. The MPW is most effective if the 3D printed material enclosing the channel is sufficiently thick (~ 500 μm) to mask the rest of the channel from unwanted polymerization (see Figure 5.4).
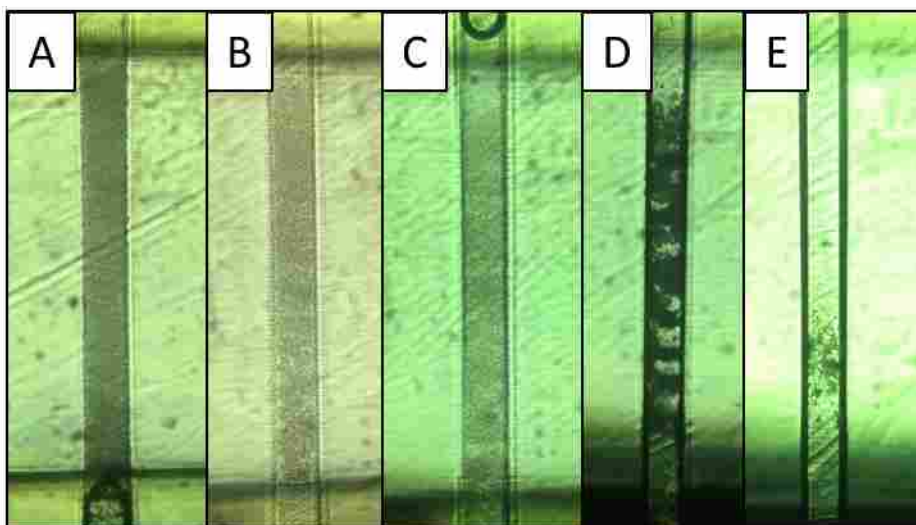
Figure 5.4 Polymerization of monoliths through different material thicknesses to measure good formation and MPW shielding thicknesses. A) 5 layers (50 µm). Monolith is well formed. B) 15 layers (150 µm). Monolith is mostly formed. C) 25 layers (250 µm). Monolith is partly formed. D) 35 layers (350 µm). Channel was dried to show formation better; polymerization is patchy. E) 45 layers (450 µm). Minor polymerization on channel surfaces, indicating a minimum of 50 layers (500 µm) is needed to shield the channels.

For the analysis of immunoaffinity extraction of Fer from spiked blood serum background subtracted fluorescent CCD images were taken of the monolith after loading sample, each rinse, and elution. The fluorescence on the monolith was calculated by comparing these images. For these experiments a high signal is expected during the loading step as fluorescent material is loaded onto the monolith. During the rinse steps for both the control and test monolith the signal should drop as nonspecifically bound material is rinsed off, but the drop should be much more pronounced in the control. In the elution step the control should remain low but the sample monolith fluorescence should drop to a similarly low level.

Figure 5.5A shows that for the control monolith (lacking antiferritin), the signal dropped the most between the loading and rinse steps, and was more similar between the rinses and elution. This was the expected result, because the majority of the labeled ferritin should rinse out from the control monolith since there is no antibody to retain the ferritin. The residual signal

after rinsing and elution is likely from nonspecifically adsorbed ferritin bound to the monolith. In contrast, when antiferritin is attached to the monolith, there is a smaller decrease in fluorescent signal between loading and rinsing than in the control, because ferritin retained by the antibody on the monolith does not wash off during the rinsing step. In these experiments, a much larger, ~2-fold, drop in fluorescence occurs between the rinse and the elution, indicating that much of the extracted ferritin was eluted. The signal in these experiments does not return to background levels after elution for control or test monoliths, indicating incomplete recovery (~50%) of extracted sample. Recovery could be increased by lowering nonspecific adsorption through monolith formulation optimization. I note that there is little nonspecific adsorption on the 3D printed device material, but that it primarily occurs on monoliths.

In order to create a PTB risk analysis device, it must be possible to extract PTB biomarkers from a blood serum matrix. To evaluate the viability of this system for such a test, a human blood serum sample was spiked with ferritin and flowed through monoliths with or without antiferritin attached as shown in Fig. 5.5B. The data show that the largest signal drop for the control is between the load and rinse steps, a statistically significant 57% decrease ($t = 11.5$, $p = 0.99$). In contrast, when antiferritin is attached to the monolith, the drop in signal between the load and rinse steps is not statistically significant at only 4.4%, ($t = 0.10$, $p = 0.99$). The largest drop in signal when antiferritin is attached to the monolith occurs between the rinse and elution steps, a statistically significant 33% decrease ($t = 1.92$, $p = 0.85$), while the difference between the rinse and the elution steps for the control at only 6% was not statistically significant ($t = 0.82$, $p = 0.85$). There is residual signal in both experiments, likely from nonspecific adsorption to the monolith as indicated earlier. The clear differences in column fluorescence between the

experiments with or without attached antiferritin give strong support to the assertion that this

PTB biomarker can be extracted from a serum sample using a 3D printed microfluidic device.
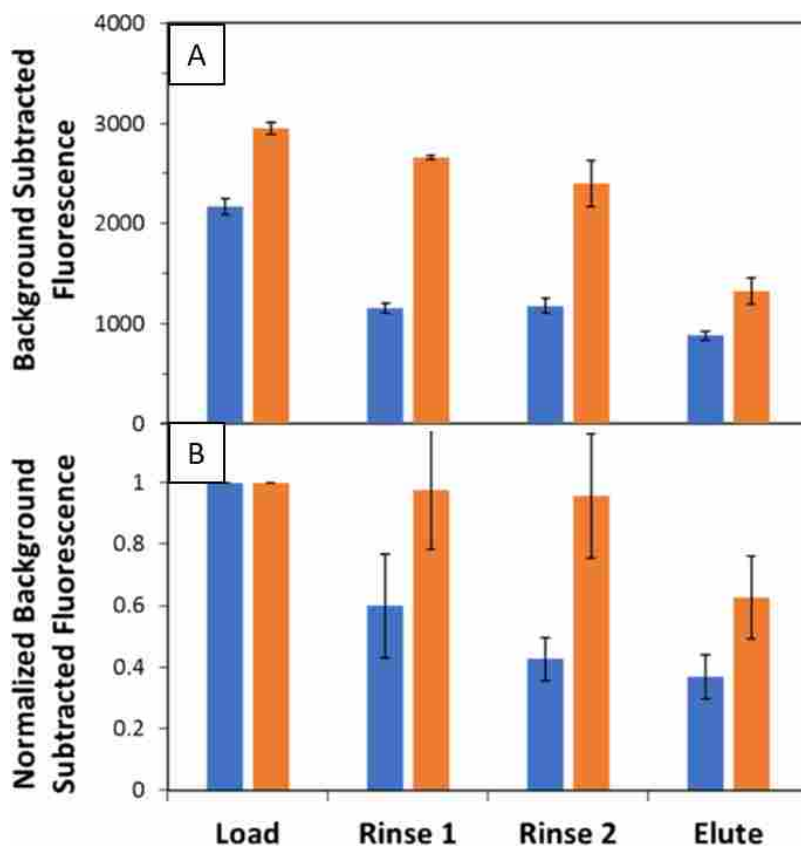
Figure 5.5 Immunoaffinity monolith extraction of ferritin. Control monoliths (no antiferritin) are in blue and monoliths with antiferritin are shown in orange. A) 50 nM ferritin. B) Human blood serum (diluted 5-fold) and spiked to 50 nM ferritin.

5.3.2 C4D Devices

A second type of device I developed was a T-shaped µCE device which could be interfaced with C4D detection. This device was built for a collaborative project with José Alberto Fracassi da Silva's group at the University of Campinas in Sao Paulo, Brazil. This group has successfully used C4D as a detection technique in microfluidics.[32-34] In an effort to increase the sensitivity I created a pair of spiral electrodes around the channel instead of the planar

electrodes typically used for this technique. I created microfluidic devices with spiral electrodes and tested them under normal and C4D like conditions. These devices were then sent to da Silva's group for testing in their apparatus using proper C4D conditions.

The device design for the spiral electrode microchips is shown in Figure 5.2. The unique feature of this device is the spiral electrode channel which wraps around the μCE separation channel. This type of structure would be essentially impossible to fabricate using conventional techniques of aligning and bonding many layers together, especially to achieve a properly aligned and continuous spiral. A photograph of a pair of the produced spirals is shown in Figure 5.6. This image shows the spiral channels with the separation channel running through them. Both channels were leak tested to ensure no cracks existed between them.
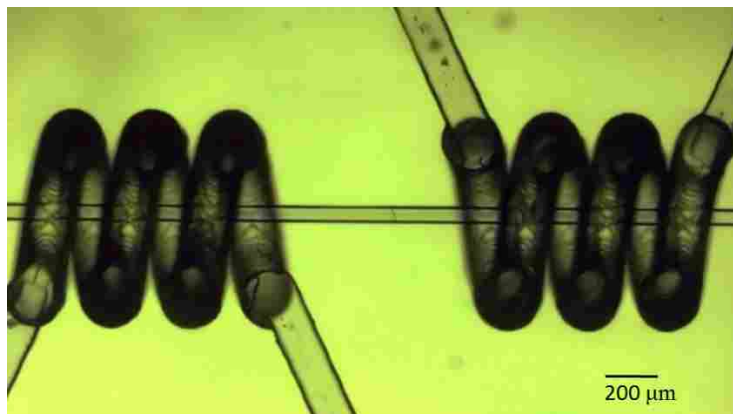
Figure 5.6 Photograph of spiral channel device. The contrast has been adjusted to help visualize the channels more clearly.

The devices were tested using a 5 nM mixture of AF labeled G and F. The separation results were compared when the spirals were empty to when the spirals were filled and run under C4D-like conditions. I used conditions to simulate a C4D environment because I lacked the

appropriate electronics for measuring the phase shift produced by the passing analytes, as well as proper shielding.

A comparison of the G and F separations without and with the channels filled and the C4D voltage applied can be seen in Figure 5.7. For these separations, the resolution without C4D applied is 2.4 and the resolution under C4D conditions is 2.1. The efficiency of the G peak is 1600 plates without C4D and with the voltage applied it is 1100. There are several factors which may account for the slightly poorer performance under C4D conditions. First the applied C4D field may influence the separation electric field lines in the detection area causing peak broadening and thus lower resolution and efficiency. Additionally, the two spiral electrodes were connected to each other in series, which is not the exact configuration used in a C4D system where the spirals would be independently connected to circuitry. Attachment of the C4D electrodes may have also affected the focus of the system and alignment of the device to the PMT pinholes which was not reverified before the analysis which could account for the lower overall signal. Importantly, this analysis demonstrates that the devices are not harmed and separations work using C4D-like conditions, and that further testing is merited. These devices were sent to da Silva's group who was able to achieve promising C4D results in μCE of potassium, sodium, and lithium ions, with gallium metal in the spiral electrode channels.
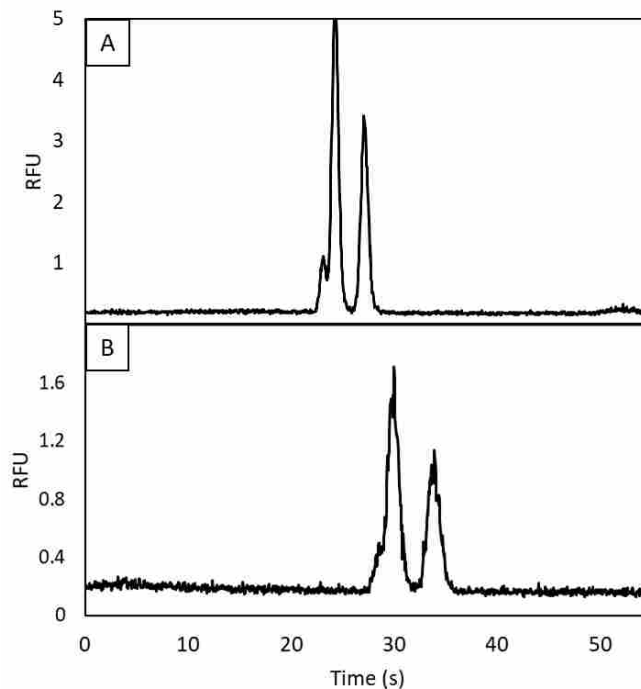
Figure 5.7 Separation of G and F in spiral electrode devices. A) Separation with spirals empty showing typical separation results for a T-shaped µCE device. B) Separation of G and F when spirals are filled with 3 M KCl and a 3 V C4D-like AC is applied at 350 kHz.

5.3.3   Microchip Electrophoresis with Removable Insert Interfacing

A final 3D printed microfluidic device I designed for unique applications was a T-shaped µCE device interfaced to a removable electrode insert for electrochemical detection. The design for this device is shown in Figure 5.3 and it consists of two 3D printed pieces that are sealed together. This ability to seal devices is based on previous work from Nordin's group which showed two devices could be sealed together to make fluidically tight seals.[30] These devices were checked for leaks in the assembled form and verified to adequately separate a G and F mixture when the insert was placed in the separation chip.

From several iterations of device designs for both the µCE and electrode insert chip I found several key design features that allowed for a fluid tight seal to form. First, the electrode insert piece made a tighter seal when the hole was set to 99% the size of the insert piece. When

97

the sizes were exactly matched, slight variations and imperfections led to frequent leaks and a poor seal between the pieces. A second key feature was to place several layers of support material around the insert piece post. Designs with no support, support on the µCE chip, and support on the electrode insert piece were tested and I found that when there was no support material or support on the µCE chip the electrode insert tended to break off the glass side easily. Thus, the optimized design of the electrode insert piece had support to help it stay attached to the glass slide. Figure 5.8 shows the three designs with the optimized design shown in Figure 5C.
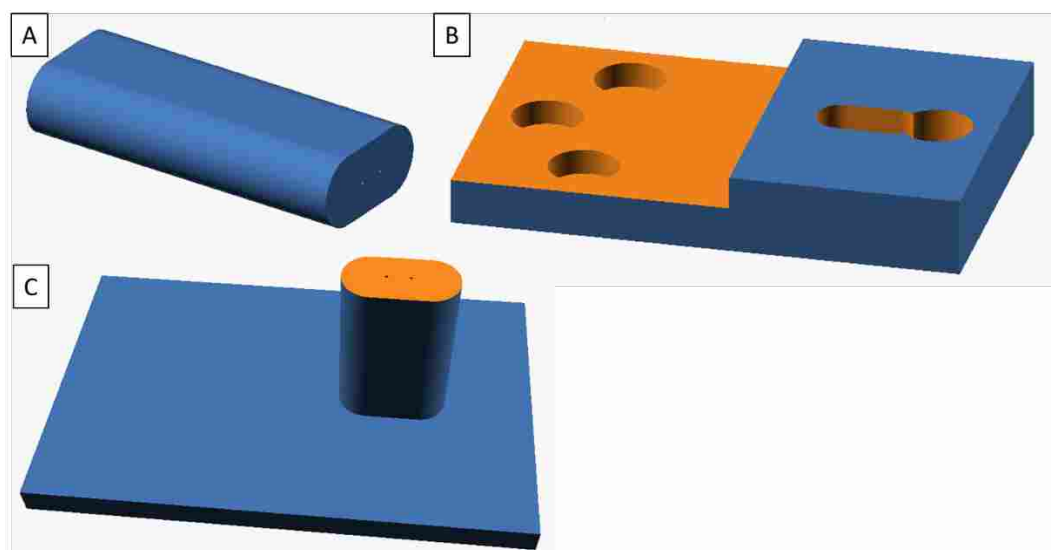
Figure 5.8 Designs for various electrode insert pieces. A) Electrode insert without any support features. This design broke off the glass slide easily. B) Extra support was placed on the µCE piece, but this caused the insert to get stuck and break. C) Optimal design with support to attach the insert to the glass slide.

For separation experiments, the assembled µCE and insert pieces were clamped together as described in section 5.2.5. A photograph of the assembled setup with the electrodes in place to run the µCE chip is shown in Figure 5.9A, and the resulting electropherogram can be seen in Figure 5.9B. There is a little more baseline noise in this run compared to similar runs of these same analytes (Figs. 4.5A and 5.7A). For this analysis I noticed the current in the channel (one

measure of device performance) was a more erratic than is typical for µCE devices without any modifications. As a result, I used lower voltages, +200 V for injection and +400 V for separation, in order to achieve a satisfactory electropherogram. These two factors could be attributed to a small amount of capillary flow into the electrode insert holes. The two holes that are in the insert piece will hold the detection electrodes in the final version but currently are open. Even though the insert piece is printed on a glass slide so the other end of the electrode holes is blocked, some liquid can be drawn into these holes. This could affect both the electric field lines as new conductive paths are opened, as well as draw sample into the holes, potentially resulting in a noisier baseline with several small, broad, unidentified peaks. I expect that with further optimization and a device with electrodes in place these peaks should be reduced or eliminated.
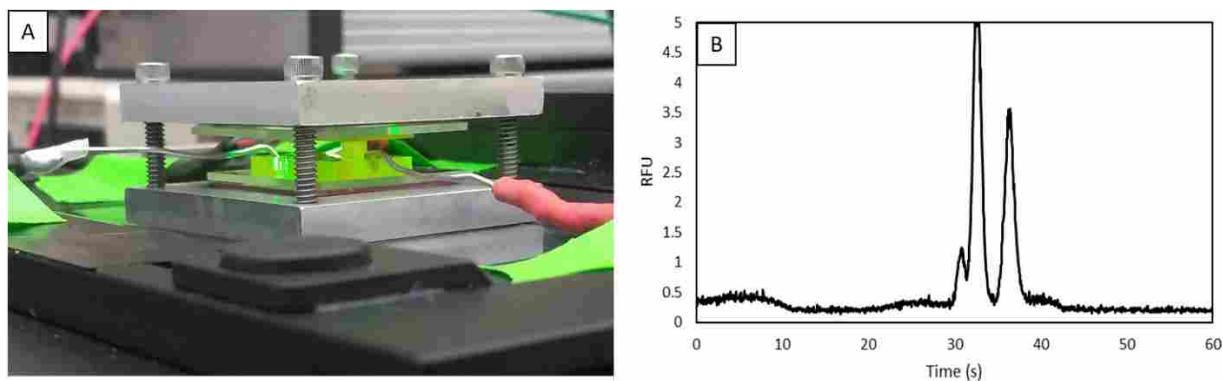
Figure 5.9 Photograph and electropherogram from devices for electrochemical detection. A) Photograph of assembled device ready for analysis. The µCE chip is on bottom and the electrode insert is on top. The device is sandwiched between two aluminum plates and the running electrodes are in place. B) Electropherogram of 5 nM G and F sample using assembled electrochemical detection device.

All three of the devices used in this chapter have unique designs enabled by 3D printing of microfluidic structures. Immunoaffinity capture monoliths were polymerized in a well defined and spatially controlled way, taking advantage of the UV absorber in the resin from the 3D

printing process. They were then used to selectively extract ferritin from 20% blood serum. In a demonstration of more fully utilizing the Z dimension of microfluidic devices, spiral electrode channels for C4D were printed, tested, and sent to a collaborator for further characterization. The initial promising results show that the devices function as expected and there is potential to use 3D printed devices for μCE with C4D. Finally, initial designs were developed for a device that could be interfaced to electrochemical detection using a removable electrode insert. Several device iterations were tested to develop a liquid tight seal, and a preliminary amino acid separation was demonstrated to show the assembled chip functions as expected. More work needs to be done to allow electrodes to be interfaced to the insert chip and then the devices can be sent to a collaborator for electrochemical detection. These devices show great promise for 3D printed microfluidics to be developed for a wide variety of analyses. Indeed 3D printing will likely lead to many new analyses based on the advantages it offers over traditional fabrication techniques, such as those demonstrated here.

5.4   References

1.   Dixit, C. K., Kadimisetty, K., Rusling, J. 3D-printed miniaturized fluidic tools in chemistry and biology. *Anal Chem*. **2018**, 106, 37-52.

2.   Beauchamp, M. J., Nordin, G. P., Woolley, A. T. Moving from millifluidic to truly microfluidic sub-100-μm cross-section 3D printed devices. *Anal Bioanal Chem*. **2017**, 409, 4311-9.

3.   Au, A. K., Huynh, W., Horowitz, L. F., Folch, A. 3D-printed microfluidics. *Angew Chem Int Ed*. **2016**, 55, 3862-81.

4.   Waheed, S., Cabot, J. M., Macdonald, N. P., Lewis, T., Guijt, R. M., Paull, B., Breadmore, M. C. 3D printed microfluidic device: enablers and barrier. *Lab Chip*. **2016**, 16, 1993-2013.

5.   Chen, C., Mehl, B. T., Munshi, A. S., Townsend, A. D., Spence, D. M., Martin, R. S. 3D-prnited microfluidic devices: fabrication, advantages and limitations-a mini review. *Anal. Methods*. **2016**, 8, 6005-12.

6.   Jonusauskas, L., Gailevicius, D., Rekstyte, S., Juodkazis, S., Malinauskas, M. Synchronization of linear stages and galvo-scanners for efficient direct laser fabrication of polymeric 3D meso-scale structures. *Proceedings of the SPIE*. **2018**, 10523, 105230X-8.

7.   Mannel, M. J., Selzer, L., Bernhardt, R., Thiele J. Optimizing Process Parameters in Commercial Micro-Stereolithography for Forming Emulsions and Polymer Microparticles in Nonplanar Microfluidic Devices. *Adv. Mat. Tech*. **2018**, 4. 1800408.

8.   Zhang, J. M., Li, E. Q., Aguirre-Pablo, A. A., Thoroddsen, S. T. A simple and low-cost fully 3D-printed non-planar emulsion generator. *RSC Adv*. **2016**, 6, 2793-9.

9.   Mandon, C. A., Blum, L. J., Marquette, C. A. Adding Biomolecular Recognition Capability to 3D Printed Objects. *Anal. Chem*. **2016**, 88, 10767–72.

10.   Monaghan, T., Harding, M. J., Harris, R. A., Friel, R. J., Christie, S. D. R. Customizable 3D printed microfluidics for integrated analysis and optimization. *Lab Chip*. **2016**, 16, 3362-73.

11.   Beauchamp, M. J., Nielsen, A. V., Gong, H., Nordin, G. P., Woolley, A. T. 3D printed microfluidic devices for microchip electrophoresis of preterm birth biomarkers. *Anal. Chem*. **2019**, 91, 7418-25.

12.   Yuen, P. K. Embedding objects during 3D printing to add new functionalities. *Biomicrofluidics*. **2016**, 10, 044104.

13.   Lee, K. G., Park, K. J., Seok, S., Shin, S., Kim, D. H., Park, J. Y., Heo, Y. S., Lee, S. J., Lee, T. J. 3D printed modules for integrated microfluidic devices. *RSC Adv*. **2014**, 4, 32876-80.

14.   Lee, W., Kwon, D., Chung, B., Yung, G. Y., Au, A., Folch, A., Jeon, S. Ultrarapid detection of pathogenic bacteria using a 3D immunomagnetic flow assay. *Anal Chem*. **2014**, 86, 6683-8.

15.   Sonker, M., Yang, R., Sahore, V., Kumar, S., Woolley, A. T. On-chip fluorescent labeling using reversed-phase monoliths and microchip electrophoretic separation of selected preterm birth biomarkers. *Anal. Methods*. **2016**, 8, 7739-46.

16.   Sonker, M., Knob, R., Sahore, V., Woolley, A. T. Integrated electrokinetically driven microfluidic devices with pH-mediated solid-phase extraction coupled to microchip electrophoresis for preterm birth biomarkers, *Electrophoresis*. **2017**, 38, 1743-54.

17.   Kumar, S., Sahore, V., Rogers, C. I., Woolley, A. T. Development of an integrated microfluidic solid-phase extraction and electrophoresis device. *Analyst*. **2016**, 141, 1660-8.

18.   Yang, R., Pagaduan, J. V., Yu, M., Woolley, A. T. On chip preconcentration and fluorescence labeling of model proteins by use of monolithic columns: device fabrication, optimization, and automation. *Anal. Bioanal. Chem*. **2015**, 407, 737-47.

19.   Parker, E. K., Nielsen, A. V., Beauchamp, M. J., Almughamsi, H. M., Nielsen, J. B., Sonker, M., Gong, H., Nordin, G. P., Woolley, A. T. 3D printed microfluidic devices with immunoaffinity monoliths for extraction of preterm birth biomarkers. *Anal. Bioanal. Chem*. **2018**. DOI: https://doi.org/10.1007/s00216-018-1440-9.

20.   Terry, S. C., Jerman, J. H., Angell, J. B. A gas chromatographic air analyzer fabricated on a silicon wafer. *IEEE Trans. Electron Devices*. **1979**, 26, 1880-1886.

21.   Harrison, D. J., Manz, A., Fan, Z., Luedi, H., Widmer, H. M. Capillary electrophoresis and sample injection systems integrated on a planar glass chip. *Anal. Chem*. **1992**, 64, 1926-32.

22.   Das, S., Srivastava, V. C. Microfluidic-based photocatalytic microreactor for environmental application: a review of fabrication substrates and techniques, and operating parameters. *Photochem. Photobiol. Sci*. **2016**, 16, 714-30.

23.   Lazar, I. M., Grym, J., Foret, F. Microfabricated devices: A new sample introduction approach to mass spectrometry. *Mass Spec. Rev*. **2006**, 25, 573-94.

24.   Johnson, M. E., Landers, J. P. Fundamentals and practice for ultrasensitive laser-induced fluorescence detection in microanalytical systems. *Electrophoresis*. **2004**, 25, 3513-27.

25.   Fischer, D. J., Hulvey, M. K., Regel, A. R., Lunte, S. M. Amperometric detection in microchip electrophoresis devices: Effect of electrode material and alignment on analytical performance. *Electrophoresis*. **2009**, 30, 3324-33.

26.   Guijt, R. M., Baltussen, E., van der Steen, G., Frank, H., Billiet, H., Schalkhammer, T., Laugere, F., Vellekoop, M., Berthold, A., Sarro, L., van Dedem, G. W. K. Capillary electrophoresis with on-chip four-electrode capacitively coupled conductivity detection for application in bioanalysis. *Electrophoresis*. **2001**, 22, 2537-41.

27.   Brito-Neto, J. G. A., da Silva, J. A. F., Blanes, L., do Lago, C. L. Understanding Capacitively Coupled Contactless Conductivity Detection in Capillary and Microchip Electrophoresis. Part 1. Fundamentals. *Electroanalysis*. **2005**, 17, 1198-206.

28.   Coltro, W. K. T., Lima, R. S., Segato, T. P., Carrilho, E., de Jesus, D. P., do Lago, C. L., da Silva, J. A. F. Capacitively coupled contactless conductivity detection on microfluidic systems—ten years of development. *Anal. Methods*. **2012**, 4, 25-33.

29.   Erkal, J. L., Selimovic, A., Gross, B. C., Lockwood, S. Y., Walton, E. L., McNamara, S., Martin, R. S., Spence, D. M. 3D printed microfluidic devices with integrated versatile and reusable electrodes. *Lab Chip*. **2014**, 12, 2023-32.

30.   Gong, H., Woolley, A. T., Nordin, G. P. 3D printed high density, reversible, chip-to-chip microfluidic interconnects. *Lab Chip*. **2018**, 18, 639-47.

31.   Gong, H., Bickham, B. P., Woolley, A. T., Nordin, G. P. Custom 3D printer and resin for 18 μm× 20 μm microfluidic flow channels. *Lab Chip*. **2017**, 17, 2899-909.

32.   Campos, C. D. M., Reyes, F. G., Manz, A., da Silva, J. A. F. On-line electroextraction in capillary electrophoresis: Application on the determination of glutamic acid in soy sauces. *Electrophoresis*. **2018**, 40, 322-9.

33.   Coelho, A. G., de Jesus, F. F. S., de Assis Pallos, L., da Silva, J. A. F., de Jesus, D. P. Capillary electrophoresis with capacitively coupled contactless conductivity detection for the determination of propionate and sorbate in bread. *J. Sep. Sci*. **2018**, 41, 3932-7.

34.   Guimaraes, I. C., da Silva, J. A. F., de Jesus, D. P. Comparison of Potassium and Sodium Content in Diet and Non-Diet Soft Drinks by Using Capillary Electrophoresis with Capacitively Coupled Contactless Conductivity Detection. *Eclética Química*. **2009**, 34, 51-6.

6. CONCLUSIONS AND FUTURE WORK

6.1 Conclusions

6.1.1 Printer and Resin Development

In chapter 2, the importance of matching the resin absorption properties to the 3D printer light source, as well as careful control over light penetration deeper into the resin, were characterized both theoretically and experimentally.[1] To help determine appropriate resin formulations, spectral measurements were made of various UV absorbers so their potential use could be evaluated with various acceptance criteria such as solubility, spectral overlap, print mechanical strength, and others. A mathematical model based on the absorptivity of the resin was evaluated by producing millifluidic channels using 3 commercial and open source resins.

6.1.2 3D Printed Resolution Features

Given ability the to 3D print microfluidic sized channels with a custom built 3D printer in the Nordin lab, I sought to further characterize this printer by producing a variety of resolution evaluation features, such as exterior and interior trenches, ridges and interior micropillars.[2] The importance of exposure time for a feature was examined between 500 and 1500 ms, as well as a unique light compensation pattern enabled by this custom printer. The minimum trench and ridge size that was printed was ~ 20 μm in either interior or exterior features, and the minimum pillar size was 16 μm. This information about the printer capabilities allowed me to create microfluidic particle traps for the capture of 25 μm polystyrene beads.

6.1.3 Microchip Electrophoresis of Pre-Term Birth Biomarkers

In chapter 4, as a demonstration of the use of 3D printed microfluidic devices, I conducted the first microchip electrophoresis (µCE) separation in a 3D printed device with channels ~50 µm.[3] Various separation parameters such as device layout, running buffer (50 mM HEPES pH 8 with 1% HPC), and applied voltage (+225 and 500 V) were optimized for these devices. The devices were also characterized based on channel size using the reduced edge compensation pattern described in chapter 3, as well as optical properties such as transmission and autofluorescence. A model mixture of two fluorescently labeled amino acids (G and F) was used to demonstrate the system function and characterize the separations with resolution between the peaks of 2.3. The separation efficiency of G was 1600 and of F was 1700. I then expanded this analysis to a mixture of three fluorescently labeled medically relevant PTB biomarkers, P1, CRF, and Fer. The resolution between P1 and CRF was 2.1 and the separation efficiency of P1 was 3600. The limits of detection for these analytes were 7 nM for P1, 0.2 nM for CRF, and 4 nM for Fer. Importantly, these devices show comparable resolution, efficiency, and detection limits to conventional microfluidic devices previously used in Woolley's group. In summary, this demonstrates for the first time microchip electrophoresis in a 3D printed device.

6.1.4 Unique Devices Enabled by 3D Printing

In chapter 4 one application of 3D printed microfluidic devices was demonstrated through microchip electrophoresis of PTB biomarkers. Chapter 5 describes several collaborative projects that demonstrate the broader applicability of these device types that can be 3D printed. The first type of novel application was the creation of a monolith polymerization window (MPW) in the devices to take advantage of the UV absorber in the resin to reproducibly and

carefully control the position and size of porous polymer monoliths produced in devices for immunoaffinity extraction of PTB biomarkers from blood.[4] The results showed better control over monolith size and position than traditional photomasking techniques. These monoliths then were successfully used to extract Fer from spiked 20% serum samples. A second technique that used the unique capabilities of 3D printing was the development of spiral channels for electrodes in combination with our μCE devices for use in capacitatively coupled contactless conductivity (C4D) applications. This device geometry is nearly impossible to achieve with conventional fabrication techniques but easily accessible with 3D printing. These devices were then sent to our collaborator Fracassi da Silva in Brazil for further testing. The final application demonstrated was a removable insert interfaced with μCE that could potentially be used for on-chip electrochemical detection. These devices entailed developing a microfluidic seal between the two chips as well as confirming that separations still function once the pieces are attached together. All of these projects illustrate the broad applicability of 3D printed microfluidic devices.

6.2   Future Work

6.2.1   Printer and Resin Development

To help further improve the ability to 3D print devices for microfluidics, new printers will need to be built and new resin options for use in the printers will need to be formulated. To further improve the printer, work could be done to improve the X-Y resolution, as this is one area in which 3D printing lags behind conventional techniques. The current printer has about 7.6 μm resolution enabling creation of channels as small as 20 μm. However, with the move to smaller features, there is a trade-off between resolution and available print space. Higher resolution features are typically obtained through smaller pixel sizes by reduced micromirror size

or through the imaging system. Because the pixel count is limited due to cost this typically results in a smaller print area. For my devices in chapters 3-4 I was limited to a print area of about 12 mm × 20 mm; however, microfluidic devices could be made larger (up to even ~10 cm or more). In order to create high resolution features while still maintaining an adequate print size, there are a few options. First, the high resolution projector could be translated around a print area and multiple images could be stitched together to create a large print. To aid in this, a second projector could be used to more quickly expose large areas that do not require high resolution features. Secondly, two photon polymerization techniques can be used to create extremely high resolution prints (nm scale), and while this technique theoretically can be used to produce large prints, practically it only results in prints about 1 mm^3 in about 20 hours.[5] However, coupling this technique to a projector for the larger areas (without fine feature prints) could result in extraordinarily fine features.

In addition to improving the X-Y resolution, more work could be done to improve the Z resolution and utilization in prints. Vertical features are an area where 3D printing has advantages over traditional microfluidic fabrication techniques because of the ease of printing these features instead of bonding many layers together. For chapters 2 and 4, most of the features are of a planar nature; however, in chapters 3 and 5 several devices are shown with greater use of the third dimension. Features where there is not a need to have them running in an X-Y direction can be stacked on top of each other in a vertical fashion which can save area in the device footprint. This would allow for complex fluidic networks where channels can run over, under, or around features with greater ease. Ultimately, this could lead to small and complex devices with little wasted space and a path toward parallelism where many devices can be printed at once even in small build areas. Key to obtaining such tight networks will be careful control of the Z size of

features. Efforts to improve the Z resolution of print would largely involve the further optimization of resin formulations as demonstrated in chapter 2.

In addition to improving the printers used for making microfluidic features, more work should be done to enhance the properties of the resins used in these printers. To help improve polyjet and fused deposition modeling printing the first advancement that is needed is more easily cleared support materials. Whether these could be some sort of ionic compounds that could dissolve in water, or different hydrophobic material (as opposed to wax-like substances currently used) that could dissolve more easily in organic solvents remains to be seen, but either could improve the channel sizes achievable with these printer types. Regarding stereolithography (SLA) resins, opportunities exist for expanding on the monomers used, as nearly all are acrylates and most of these formulations are proprietary. Alternatives such as styrenes ought to be further explored. In addition, the variety of potential additives will also be crucial to fine tune the characteristics of the resin such as biocompatibility, optical transmission properties, and material strength among others. All of these aspects of resin development will require careful and systematic examination as potential combinations and compounds abound.

6.2.2   PTB Device Improvements

While the separations demonstrated in chapter 4 demonstrate an important step in the development of microfluidic devices for PTB biomarkers, there is still much work to be done to improve the results. The separation demonstrated here only accounts for 3 of the PTB biomarkers, and 6 more need to be added to this analysis for it to be fully useful. Additional experiments need to be conducted to determine if these biomarkers will run well in a 3D printed device and whether or not they can be separated from P1, CRF, and Fer as well as each other. If

the current devices are insufficient to separate the biomarkers, modifications can be made to the device to help this effort. For example, a serpentine channel geometry can be used to increase the length of the separation channel allowing for more distance to separate the biomarkers.[8] Figure 6.1A shows an OpenSCAD design where serpentine designs were used. To help prevent excessive band broadening, a tapered turn was designed as shown in Figure 6.1B. Because 3D printing allows better use of a three dimensions for device layouts, the channels can be extended to be above or below others resulting in a very long separation channel (650 mm) if 6 layers of channels with 11 channels per layer are used which is similar to the spacing shown in Fig 6.1A. The serpentine channel bend can easily be extended into all three dimensions.
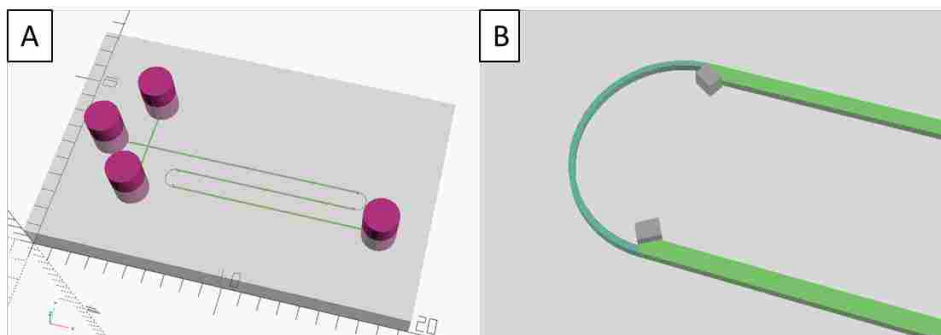
Figure 6.1 OpenSCAD designs of serpentine channels. (A) Overall device design with reservoirs shown in purple and channels in green. The tapered turns are blue. (B) Zoomed view of one turn. The channels are green and turn is blue. The darker gray blocks show where the taper occurs and will be part of the bulk in the final print.

In addition to a more complete and optimized separation module, this component needs to be integrated with two other major processes for sample treatment, immunoaffinity extraction and on-chip labeling. Part of the immunoaffinity extraction module was presented in chapter 5 for the extraction of ferritin from serum.[5] However, this was only for one biomarker in isolation from the other steps of the analysis. In the final integrated device all 9 biomarkers will need to go through the processes of isolation, labeling, separation and quantification. Work is presently

being done to both develop the individual modules as well as integrate the modules together. Indeed a fellow graduate student has promising results for the extraction of several other PTB biomarkers (CRF, lactoferrin, and P2) from buffer using antibodies. Work on the on-chip labeling step has not yet progressed to the point where it can be interfaced to the other aspects of the devices but promising preliminary steps have been taken.

6.2.3   Work with Collaborators

Because of the unique capabilities allowed by this 3D printing system producing microfluidic features, I have had the fortunate opportunity to work on several interesting collaborations with other research groups. To this end I have demonstrated initial viability of these devices and the potential they might hold. The spiral electrode microchips were shown to have similar separation results when the spirals were empty compared to filled with a concentrated salt solution with the C4D applied signal applied. These results demonstrated that devices can withstand the desired conditions and that the spirals do not interfere with detection of fluorescently labeled analytes. Additional work for this project will include optimization of the system for C4D. For example, in a recent iteration of the design I adjusted the distance from the spirals to the high voltage reservoir due to an issue related to delamination causing the devices to crack. Further optimization could include spiral spacing, spiral diameter, separation between the coil and running channels, integration with the serpentine geometry after this has been improved, and further optimization of the channel size with a higher resolution printer previously discussed.

The second major external collaboration which I worked on was the creation of microchip electrophoresis devices for interfacing with electrochemical detection. These devices

are in a more preliminary stage of work but still show potential as a promising project to be carried out in the future. The initial work shows that the two pieces can be connected without leaking and degradation of the separation results. These devices still need to have the top insert piece printed on PMMA substrates with appropriate holes for the electrodes to be inserted into the chip. Additionally, the substrate piece will need to have a hole through which the detection electrodes can be interfaced to the end of the channel. Initial testing will consist of blocking the detection electrode hole and testing if the separation results are affected by the insert chip in this configuration. Also this will serve as a test of the repeatability of the seal between the chips and if further optimization of the sealing mechanism is necessary. With the current test setup I was able to get a seal between the chips but it was rather difficult because the chips are not centered in the clamping apparatus, and to the contact area is much smaller than is typically used. I expect that an alternative clamping setup for providing steady sealing pressure between the chips could be specifically designed. Finally, for this project devices need to be shipped to our collaborator so they can actually insert the detection electrodes and attempt to use the chips in their setup. This will also undoubtedly entail further optimization of the design for electrode placement, hole size, and support around the inset post. Indeed, alternative insert shapes could be created as well if the current design proves difficult to optimize. Given the ease of modifying designs however, this should be feasible.

This dissertation demonstrates some of the possibilities for 3D printing of microfluidic devices and their applications in analyses. The ability to 3D print microfluidic devices is still an emerging and developing technology with high upside that will continue to be explored. The potential upside offered by 3D printing to make compact devices with unique geometries will lead to new analyses. The potentially wide variety of materials that can be explored will also

prove to be useful to expand possible applications. There is a large gap between current commercially available 3D printing capabilities and what is required for 3D printing microfluidics. The field of 3D printing microfluidics is still being developed and holds great promise for the future as researchers, tools, and applications come together in unique ways.

6.3   References

1.   Gong, H., Beauchamp, M., Perry, S., Woolley, A. T., Nordin, G. P. Optical approach to resin formulation for 3D printed microfluidics. *RSC Adv.* **2015**, 5, 106621-32.

2.   Beauchamp, M. J., Gong, H., Woolley, A. T., Nordin, G. P. 3D printed microfluidic features using dose control in X, Y, and Z dimensions. *Micromachines*. **2018**, 9, 326-1-12.

3.   Beauchamp, M. J., Nielsen, A. V., Gong, H., Nordin, G. P., Woolley, A. T. 3D printed microfluidic devices for microchip electrophoresis of preterm birth biomarkers. *Anal. Chem*. **2019**, 91, 7418-25.

4.   Parker, E. K., Nielsen, A. V., Beauchamp, M. J., Almughamsi, H. M., Nielsen, J. B., Sonker, M., Gong, H., Nordin, G. P., Woolley, A. T. 3D printed microfluidic devices with immunoaffinity monoliths for extraction of preterm birth biomarkers. *Anal. Bioanal. Chem*. **2018**, DOI: https://doi.org/10.1007/s00216-018-1440-9.

5.   Nanoscribe. Photonic Professional Data Sheet. http://www.nanoscribe.de/files/4414/7393/1095/DataSheet_PP_V05_2016_Web.pdf (Accessed December 12, 2018).

6.   Nordin, G. P., Gong, H., Viglione, M., Hooper, K., Woolley, A. T. 3D printing for lab-on-a-chip devices with 20 μm channels. *Proceedings Volume 10932, Emerging Digital Micromirror Device Based Systems and Applications XI. SPIE*. **2019**, 1093207.

7.   Paegel, B. M., Hutt, L. D., Simpson, P. C., Mathies, R. A., Turn geometry for minimizing band broadening in microfabricated capillary electrophoresis channels. *Anal. Chem.* **2000**, 72, 3030–7.

APPENDIX A. DATA FOR RESOLUTION FEATURE MEASUREMENTS

This appendix contains all the images used for measurements of interior and exterior features in chapter 3. The standard deviation is given for each measurement at n=3. The tables are organized as follows:

Exterior Features A1-9
    Ridges A1-3
        500 ms exposure A1
        1000 ms exposure A2
        1500 ms exposure A3
    Trenches with edge compensation A4-6
        500 ms exposure A4
        1000 ms exposure A5
        1500 ms exposure A6
    Trenches without edge compensation A7-9
        500 ms exposure A7
        1000 ms exposure A8
        1500 ms exposure A9
Interior Features A10-21
    Ridges A10-12
        500 ms exposure A10
        1000 ms exposure A11
        1500 ms exposure A12
    Trenches with edge compensation A13-15
        500 ms exposure A13
        1000 ms exposure A14
        1500 ms exposure A15
    Trenches without edge compensation A16-18
        500 ms exposure A16
        1000 ms exposure A17
        1500 ms exposure A18
    Pillars A19-21
        500 ms exposure A19
        1000 ms exposure A20
        1500 ms exposure A21
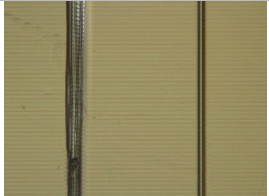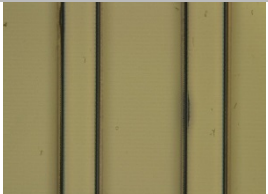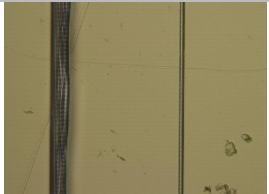
Exterior Features

Ridges
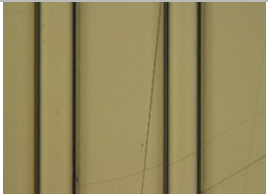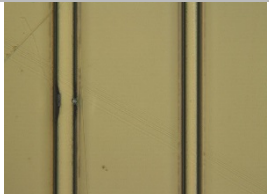
A1-Exterior ridges exposed for 500 ms. Widths range from 10 to 1 pixels from left to right. The designed and measured widths are given as well as images of the ridges.

Designed Trench Width (µm)	76.0 and 68.4	60.8 and 53.2	45.6 and 38.0	30.4 and 22.8	15.2 and 7.6
Measured Trench Width (µm)	62.0 ±0.9 and 55.3 ±1.0	48.5 ± 2.2and 40.6 ± 0.9	30.7 ± 0.8 and 23.4 ±0.2	16.1 ±1.3 and 7.5 ±0.5	3.2 ±0.3 and -
Image					

A2-Exterior ridges exposed for 1000 ms. Widths range from 1 to 10 pixels from left to right. The designed and measured widths are given as well as images of the ridges.
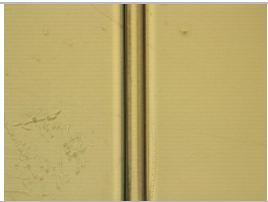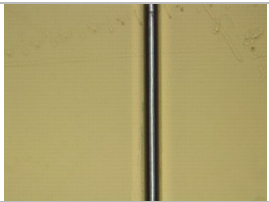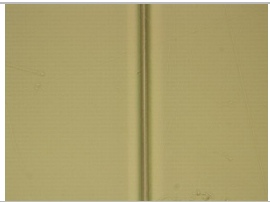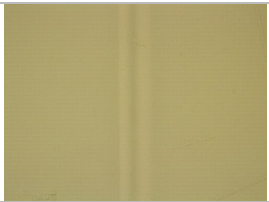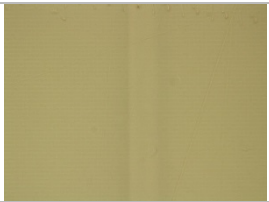
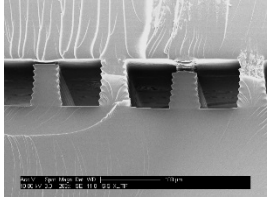| Designed Trench Width (μm)	76.0 and 68.4	60.8 and 53.2	45.6 and 38.0	30.4 and 22.8	15.2 and 7.6
Measured Trench Width (μm)	72.0 ± 0.3 and 64.4± 0.5	56.8 ± 0.3 and 48.4 ± 0.6	40.6 ±0.2 and 32.8 ± 0.9	24.9 ± 0.7 and 16.3 ± 1.5	7.2 ± 0.7 and 2.9 ± 0.4
Image					

A3-Exterior ridges exposed for 1500 ms. Widths range from 1 to 10 pixels from left to right. The designed and measured widths are given as well as images of the ridges.
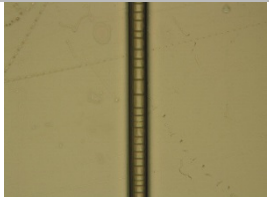
Designed Trench Width (μm)	76.0 and 68.4	60.8 and 53.2	45.6 and 38.0	30.4 and 22.8	15.2 and 7.6
Measured Trench Width (μm)	77.1 ± 0.3 and 69.2 ± 0.4	61.7 ± 0.2 and 54.0 ± 0.3	45.9 ± 0.3 and 37.9 ± 0.3	29.8 ± 1.1 and 25.3 ± 1.3	15.1 ± 0.6 and 7.1 ± 0.8
Image					

Trenches with edge compensation
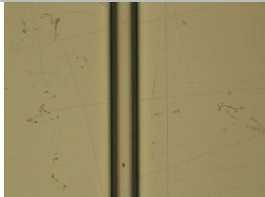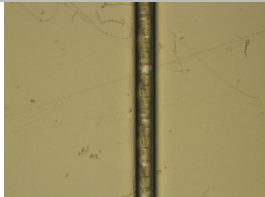
A4-Exterior trenches with edge compensation exposed for 500 ms. Widths range from 10 to 1 pixels from left to right across two rows. The designed and measured widths are given as well as images of the trenches.

Designed Trench Width (μm)	76.0	68.4	60.8	53.2	45.6
Measured Trench Width (μm)	77.3 ± 0.6	68.7 ± 0.3	61.7 ± 0.4	50.5 ± 0.6	38.9 ± 0.4
Image					
Designed Trench Width (μm)	38.0	30.4	22.8	15.2	7.6
Measured Trench Width (μm)	28.6 ± 0.7	5.5 ± 0.6	-	-	-
Image					

A5-Exterior trenches with edge compensation exposed for 1000 ms. Widths range from 10 to 1 pixels from left to right across two rows. The designed and measured widths are given as well as images of the trenches.
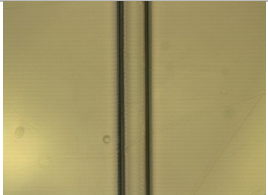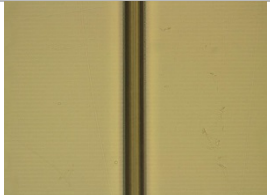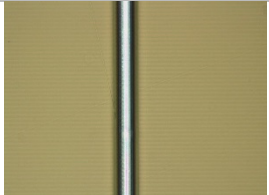
Designed Trench Width (μm)	76.0	68.4	60.8	53.2	45.6
Measured Trench Width (μm)	62.8 ± 0.2	53.5 ± 0.5	43.6 ± 0.6	33.5 ± 0.3	20.7 ± 0.4
Image					
Designed Trench Width (μm)	38.0	30.4	22.8	15.2	7.6
Measured Trench Width (μm)	13.1 ± 1.9	-	-	-	-
Image					

A6-Exterior trenches with edge compensation exposed for 1500 ms. Widths range from 10 to 1 pixels from left to right across two rows. The designed and measured widths are given as well as images of the trenches.
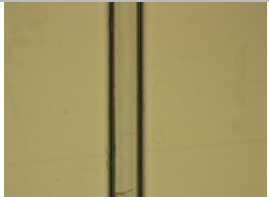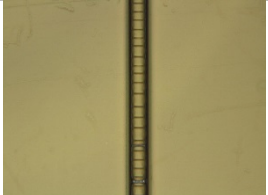
Designed Trench Width (μm)	76.0	68.4	60.8	53.2	45.6
Measured Trench Width (μm)	52.0 ± 0.3	42.9 ± 0.5	31.8 ± 0.2	22.2 ± 0.5	11.4 ± 0.4
Image					
Designed Trench Width (μm)	38.0	30.4	22.8	15.2	7.6
Measured Trench Width (μm)	9.3 ± 0.7	-	-	-	-
Image					

Trenches without edge compensation

A7-Exterior trenches without edge compensation exposed for 500 ms. Widths range from 10 to 1 pixels from left to right. The designed and measured widths are given as well as images of the trenches.

Designed Trench Width (μm)	76.0	68.4	60.8	53.2	45.6
Measured Trench Width (μm)	81.9 ± 0.5	74.3 ± 0.6	66.7 ± 0.9	58.1 ± 0.5	49.0 ± 1.2
Image					
Designed Trench Width (μm)	38.0	30.4	22.8	15.2	7.6
Measured Trench Width (μm)	41.7 ± 0.4	21.1 ± 0.6	14.2 ± 0.6	10.1 ± 0.4	-
Image					

A8-Exterior trenches without edge compensation exposed for 1000 ms. Widths range from 10 to 1 pixels from left to right across two rows. The designed and measured widths are given as well as images of the trenches.

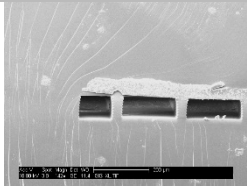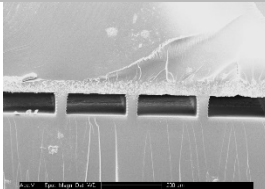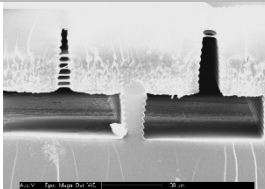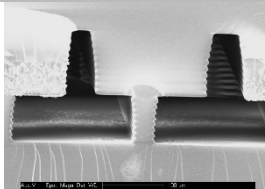|					
Designed Trench Width (μm)	76.0	68.4	60.8	53.2	45.6
Measured Trench Width (μm)	72.4 ± 0.3	64.3 ± 0.4	55.6 ± 0.2	44.9 ± 0.5	33.6 ± 0.4
Image					
Designed Trench Width (μm)	38.0	30.4	22.8	15.2	7.6
Measured Trench Width (μm)	21.1 ± 0.3	12.9 ± 1.5	11.5 ± 0.9	-	-
Image					
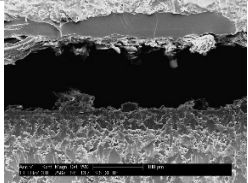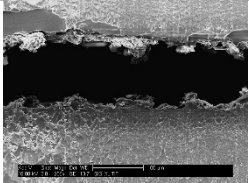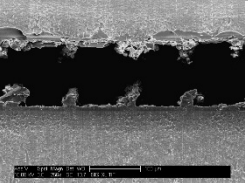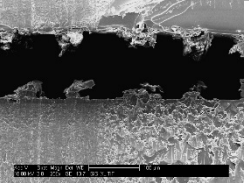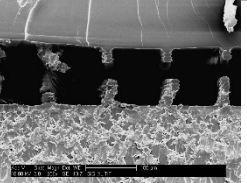
A9-Exterior trenches without edge compensation exposed for 1500 ms. Widths range from 10 to 1 pixels from left to right across two rows. The designed and measured widths are given as well as images of the trenches.

Designed Trench Width (μm)	76.0	68.4	60.8	53.2	45.6
Measured Trench Width (μm)	62.4 ± 0.2	53.6 ± 0.1	44.2 ± 0.4	33.8 ± 0.2	24.7 ± 0.6
Image					
Designed Trench Width (μm)	38.0	30.4	22.8	15.2	7.6
Measured Trench Width (μm)	16.5 ± 0.3	8.6 ± 0.7	-	-	-
Image					
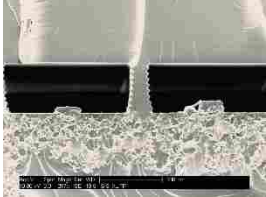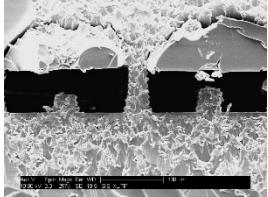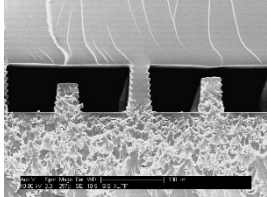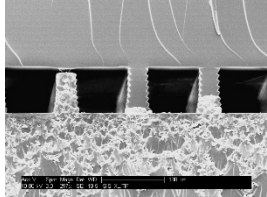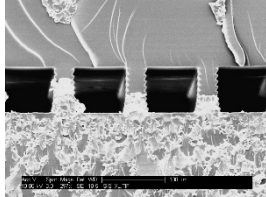
Interior Features

Ridges
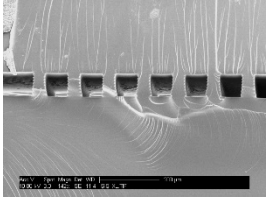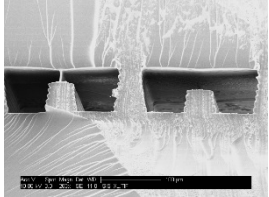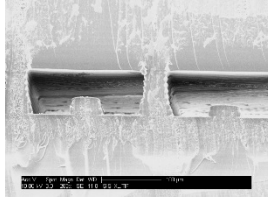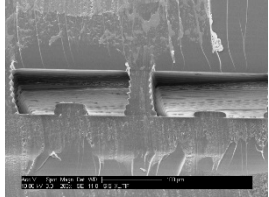
A10-Interior ridges exposed for 500 ms. Heights range from 1 to 10 layers from left to right. The designed height, measured height, and height from top of the ridge to the top of the void feature (gap height), are given, as well as images of the ridges.

Designed Ridge Height (layers)	1 and 2	3 and 4	5 and 6	7 and 8	9 and 10
Measured Ridge Height (μm)	9.8 and 18.1	18.8 and 27.8	33.8 and 38.0	55.7 and 40.1	78.5 and 79.9
Measured Gap to Ceiling (μm)	129.3 ± 0.4 and 126.3 ± 0.8	127.8 ± 2.0 and 102.3 ± 0.9	87.2 ± 5.0 and 94.7 ± 3.1	78.2 ± 4.6 and 90.8 ± 2.8	44.8 ± 2.3 and 32.1 ± 0.4
Image					

A11-Interior ridges exposed for 1000 ms. Heights range from 1 to 10 layers from left to right. The designed height, measured height, and height from top of the ridge to the top of the void feature (gap height), are given, as well as images of the ridges.
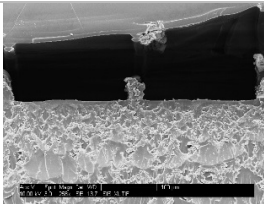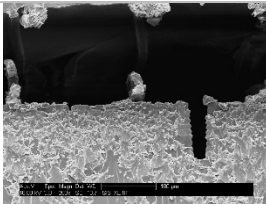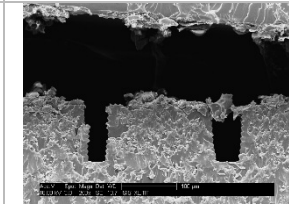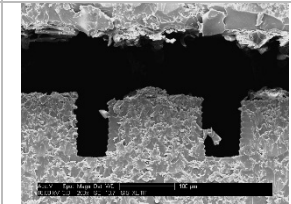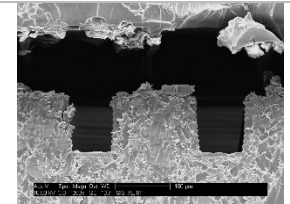
Designed Ridge Height (layers)	1 and 2	3 and 4	5 and 6	7 and 8	9 and 10
Measured Ridge Height (μm)	9.7 and 18.2	27.9 and 37.7	46.1 and 55.2	63.6 and 72.1	70.1 and 72.1
Measured Gap to Ceiling (μm)	69.5 ± 1.0 and 58.4 ± 0.8	39.6 ± 0.7 and 27.3 ± 0.7	27.9 ± 1.0 and 18.2 ± 1.0	7.1 ± 0.4 and -	- and -
Image					

A12-Interior ridges exposed for 1500 ms. Heights range from 10 to 1 layers from left to right. The designed height, measured height, and height from top of the ridge to the top of the void feature (gap height), are given, as well as images of the ridges.
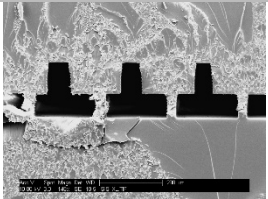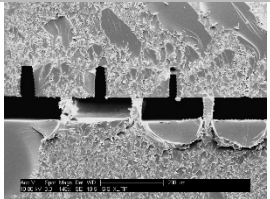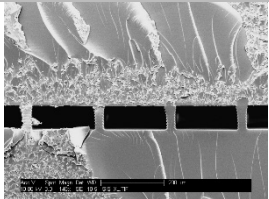
Designed Ridge Height (layers)	10, 9, and 8	7 and 6	5 and 4	3 and 2	2 and 1
Measured Ridge Height (μm)	77.6, 74.8, and 73.5	69.4 and 62.6	48.3 and 38.8	29.3 and 19.1	19.1 and 9.5
Measured Gap to Ceiling (μm)	-, -, and -	6.8 ± 0.7 and 17.7 ± 0.4	19.7 ± 1.2 and 33.3 ± 0.7	42.9 ± 0.4 and 55.1 ± 0.7	55.1 ± 0.7 and 63.3 ± 0.7
Image					

Trenches with edge compensation

A13-Interior trenches with edge compensation exposed for 500 ms. Widths range from 1 to 10 pixels from left to right.
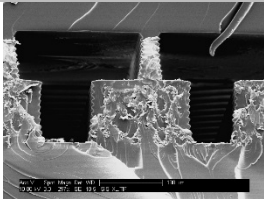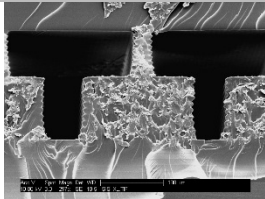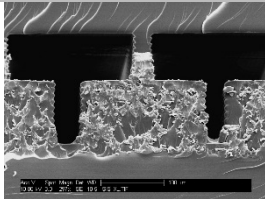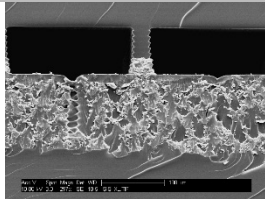The designed and measured widths are given as well as images of the trenches.

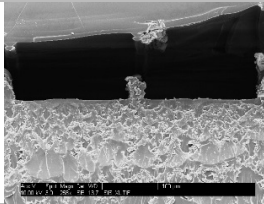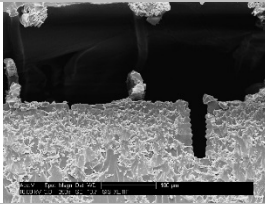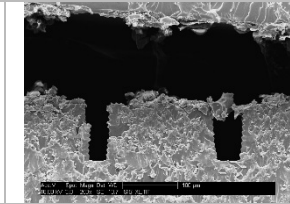| Designed Trench Width (µm)	7.6 and 15.2	22.8 and 30.4	38.0 and 45.6	53.2 and 60.8	68.4 and 76.0
Measured Trench Width (µm)	- and -	- and 25.1 ± 0.9	37.3 ± 1.2 and 50.4 ± 0.8	58.1 ± 1.2 and 69.2 ± 0.8	77.4 ± 0.8 and 84.7 ± 0.9
Image					

A14-Interior trenches with edge compensation exposed for 1000 ms. Widths range from 10 to 1 pixels from left to right. The designed and measured widths are given as well as images of the trenches.
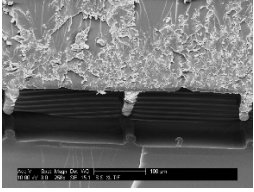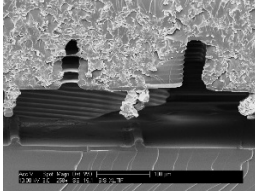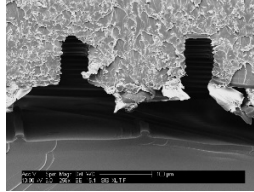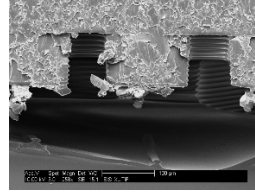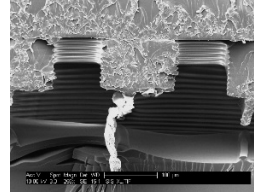
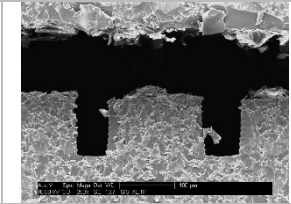| Designed Trench Width (μm)	76.0, 68.4 and 60.8	53.2, 45.6, 38.0 and 30.4	22.8, 15.2, and 7.6
Measured Trench Width (μm)	71.4 ± 1.3, 62.8 ± 1.5, and 52.8 ± 0.8	42.4 ± 0.8, 34.2 ± 0.8, 21.6 ± 0.8, and -	-, -, and -
Image			

A15-Interior trenches with edge compensation exposed for 1500 ms. Widths range from 1 to 10 pixels from left to right. The designed and measured widths are given as well as images of the trenches.
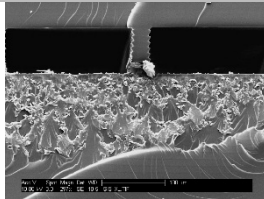
Designed Trench Width (µm)	7.6 and 15.2	22.8, 30.4, 38.0, and 45.6	53.2 and 60.8	68.4 and 76.0
Measured Trench Width (µm)	- and -	-, -, -, and -	17.7 ± 0.7 and 30.8 ± 1.0	43.1 ± 0.8 and 55.8 ± 0.7
Image				

Trenches without edge compensation

A16-Interior trenches without edge compensation exposed for 500 ms. Widths range from 1 to 10 pixels from left to right. The designed and measured widths are given as well as images of the trenches.
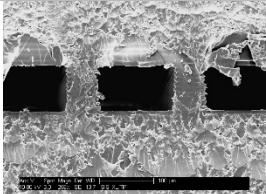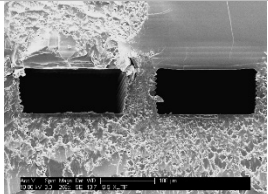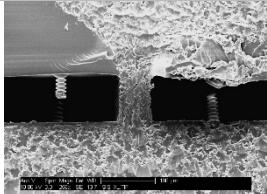
Designed Trench Width (µm)	7.6 and 15.2	22.8 and 30.4	38.0 and 45.6	53.2 and 60.8	68.4 and 76.0
Measured Trench Width (µm)	- and -	30.8 ± 0.8 and 39.1 ± 0.8	50.9 ± 0.4 and 54.4 ± 0.9	57.9 ± 0.8 and 66.9 ± 0.8	83.2 ± 0.9 and 94.7 ± 1.3
Image					

A17-Interior trenches without edge compensation exposed for 1000 ms. Widths range from 10 to 1 pixels from left to right. The designed and measured widths are given as well as images of the trenches.
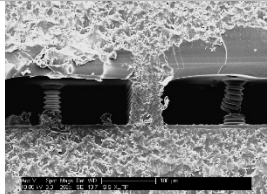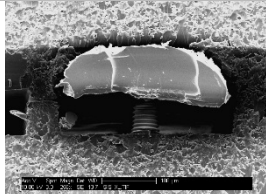
Designed Trench Width (μm)	76.0 and 68.4	60.8 and 53.2	45.6 and 38.0	30.4 and 22.8	15.2 and 7.6
Measured Trench Width (μm)	80.1 ± 0.4 and 71.0 ± 0.7	61.0 ± 0.7 and 46.3 ± 0.8	40.7 ± 1.5 and 27.9 ± 0.7	- and -	- and -
Image					

A18-Interior trenches without edge compensation exposed for 1500 ms. Widths range from 1 to 10 pixels from left to right. The designed and measured widths are given as well as images of the trenches.
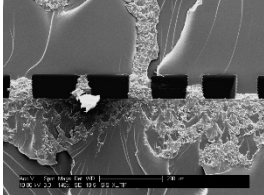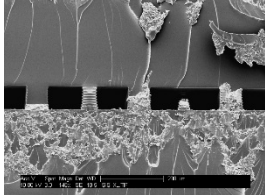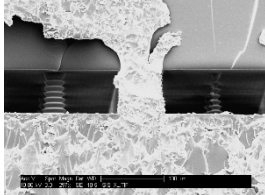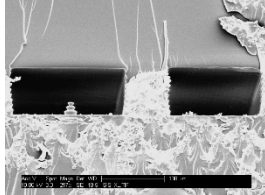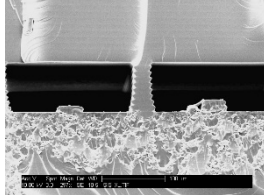
Designed Trench Width (μm)	7.6, 15.2, 22.8, and 30.4	38.0 and 45.6	53.2 and 60.8	68.4 and 76.0
Measured Trench Width (μm)	-, -, -, and -	- and 21.8 ± 0.7	34.0 ± 0.4 and 42.8 ± 0.7	57.6 ± 0.4 and 67.4 ± 0.7
Image				

Pillars

A19-Interior pillars exposed for 500 ms. Widths range from 1 to 10 pixels from left to right. The designed and measured diameters are given as well as images of the pillars.

	7.6, 15.2, and 22.8	30.4 and 38.0	45.6 and 53.2	60.8 and 68.4	76.0
Designed Pillar Diameter (µm)	7.6, 15.2, and 22.8	30.4 and 38.0	45.6 and 53.2	60.8 and 68.4	76.0
Measured Pillar Diameter (µm)	-, -, and -	- and -	19.3 ± 0.4 and 21.1 ± 0.8	31.1 ± 0.4 and 40.4 ± 0.4	49.4 ± 0.4
Image					

A20-Interior pillars exposed for 1000 ms. Widths range from 10 to 1 pixels from left to right. The designed and measured diameters are given as well as images of the pillars.

Designed Pillar Diameter (μm)	76.0 and 68.4	60.8 and 53.2	45.6 and 38.0	30.4 and 22.8	15.2 and 7.6
Measured Pillar Diameter (μm)	48.5 ± 0.8 and 50.2 ± 0.8	47.2 ± 0.8 and 35.1 ± 0.1	33.6 ± 0.8 and 16.7 ± 0.4	13.6 ± 1.1 and -	- and -
Image					

A21-Interior pillars exposed for 1500 ms. Widths range from 1 to 10 pixels from left to right. The designed and measured diameters are given as well as images of the pillars.

Designed Pillar Diameter (µm)	7.6, 15.2, 22.8 and 30.4	38.0, 45.6, and 53.2	60.8, 68.4 and 76.0
Measured Pillar Diameter (µm)	-, 12.2 ± 2.4, -, and 18.6 ± 0.8	24.9 ± 0.8, 36.3 ± 0.8, and 41.7 ± 0.8	52.6 ± 0.8, 58.0 ± 1.6, and 68.5 ± 0.8
Image			